AFWAL-TR-82-3036

PERFORMANCE METHODS FOR LIFTING ENTRY VEHICLE RANGE ANALYSIS

David T. Johnson
Charles H. Bursey
Richard C. Nash

High Speed Aero-Performance Branch
Aeromechanics Division

November 1982

Final Report for Period March 1979 to September 1981

Approved for public release, distribution unlimited.

DTIC
ELECTE
MAR 8 1983
B

83 03 08 009

REPORT DOCUMENTATION PAGE		READ INSTRUCTIONS BEFORE COMPLETING FORM
1. REPORT NUMBER AFWAL-TR-82-3036	2. GOVT ACCESSION NO. AD-A125406	3. RECIPIENT'S CATALOG NUMBER
4. TITLE *(and Subtitle)* PERFORMANCE METHODS FOR LIFTING ENTRY VEHICLE RANGE ANALYSIS		5. TYPE OF REPORT & PERIOD COVERED Final Report Mar 79 to Sep 81
		6. PERFORMING ORG. REPORT NUMBER
7 AUTHOR(s) David T. Johnson Charles H. Bursey Richard C. Nash		8. CONTRACT OR GRANT NUMBER(s)
9. PERFORMING ORGANIZATION NAME AND ADDRESS Flight Dynamics Laboratory (AFWAL/FIMG) AF Wright Aeronautical Laboratories Wright-Patterson AFB, OH 45433		10. PROGRAM ELEMENT, PROJECT, TASK AREA & WORK UNIT NUMBERS PE 6201F Project 2404, Task 240407 Work Unit 24040732
11. CONTROLLING OFFICE NAME AND ADDRESS Flight Dynamics Laboratory (AFWAL/FIM) AF Wright Aeronautical Laboratories Wright-Patterson AFB, OH 45433		12. REPORT DATE November 1982
		13. NUMBER OF PAGES 144
14. MONITORING AGENCY NAME & ADDRESS *(if different from Controlling Office)*		15. SECURITY CLASS. *(of this report)* Unclassified
		15a. DECLASSIFICATION/DOWNGRADING SCHEDULE

16. DISTRIBUTION STATEMENT *(of this Report)*

Approved for public release; distribution unlimited.

17. DISTRIBUTION STATEMENT *(of the abstract entered in Block 20, if different from Report)*

18. SUPPLEMENTARY NOTES

19. KEY WORDS *(Continue on reverse side if necessary and identify by block number)*
Lifting Entry Footprints
Temperature Constraints
Range Optimization
Simplified Control
Mapping and display

20. ABSTRACT *(Continue on reverse side if necessary and identify by block number)*
⸺ Parameter optimization methods were applied to maximize lateral range with
and without down-range constraints to produce performance footprints. Three
lifting entry vehicles with maximum lift-to-drag ratios of 1.89, 2.2, and 2.6,
respectively, were used.

A simplified bank control procedure was developed which closely approxi-
mated the optimal footprint results in the case where no heating constraints

DD $_{1\ JAN\ 73}^{FORM}$ **1473**   EDITION OF 1 NOV 65 IS OBSOLETE

20. Abstract (Continued)

were imposed. This method is easy to use and is efficient in terms of computer resources required to generate a near optimal footprint. No simple method was found to handle heating constraints, however the parameter optimization procedure was able to produce solutions for the single heating point considered. Footprint shrinkage when applying the temperature constraint was most noticeable at the front and back portions with less shrinkage in maximum cross-range. For the most stringent temperature constraint considered the results were a 19% loss in maximum down-range, a doubling of the minimum down-range and a 9.4% loss in maximum cross-range. An automated procedure was developed to display and move the footprint on world maps. This technique shows promise in relating results to functional performance and can be used separately or in conjunction with the footprint data.

FOREWORD

This technical report summarizes research performed in-house at the High Speed Aero-Performance Branch, Aeromechanics Division, Flight Dynamics Laboratory, Air Force Wright Aeronautical Laboratories, Wright-Patterson Air Force Base, Ohio. The work was performed under Project No. 2404 "Aeromechanics," Task No. 240407 "Aeroperformance and Aeroheating Technology," Work Unit 24040732 "Reentry Vehicle Performance Analysis Methods." The study period was March 1979 to September 1981.
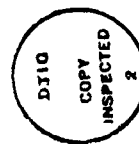
Accession For

NTIS GRA&I		✓
DTIC TAB		☐
Unannounced		☐
Justification		

By

Distribution/

Availability Codes

Dist	Avail and/or Special
A	

DTIC COPY INSPECTED 2

AFWAL-TR-82-3036

TABLE OF CONTENTS

LIST OF ILLUSTRATIONS

LIST OF ILLUSTRATIONS (Continued)

LIST OF ILLUSTRATIONS (Continued)

LIST OF ILLUSTRATIONS (Concluded)

LIST OF TABLES

LIST OF SYMBOLS

Alt	Altitude
A(1), -A(4)	Polynomial Coefficient
C	Change in Longitude
C_D	Drag Coefficient
C_L	Lift Coefficient
F	Force
g	Acceleration of Gravity
h	Altitude and Heat Transfer Coefficient
H	Enthalpy, also Gravity Coefficient in Appendix A
J	Gravity Coefficient in Appendix A
K	Slope of Bank Angle versus Heading also Units of 1000, also Gravity Coefficient in Appendix A
L/D	Lift/Drag Ratio
m	Vehicle Mass
M	Mach number
n.mi.	Nautical Miles
psf	Lb/ft^2
q	Dynamic Pressure
$\dot{q}$	Heat Rate
R	Earth Radius
°R	Degrees Rankine
R'	Average Radius of Earth
S	Aerodynamic Reference Area
T	Temperature
t	Flight Time
V	Velocity

LIST OF SYMBOLS (Continued)

X_D	Down-range
Y_D	Cross-range
i,j,k	Direction Cosines
$r,s,t,$	Direction Cosines
X,Y,Z	Position Coordinates
$\dot{X},\dot{Y},\dot{Z}$	Velocity Components in X,Y,Z Directions
W/S	Wing Loading
$\ddot{X},\ddot{Y},\ddot{Z}$	Accelerations in X,Y,Z Directions
α	Angle of attack
σ	Heading
θ	Longitude
ω_p	Earth Rotation Angular Rate
W_i	Weighting Matrix
γ	Flight Path Angle
ϕ	Payoff Function
ϕ^*	Augmented Performance Function
ϕ_B	Bank Angle
ϕ_L	Latitude
ϵ	Emissivity
u	Universal Gravity Constant
ψ	Constraint Function
ζ	Remaining Heading Change also Heading of Great Circle from Initial Point to Present Position (Figure 30)
ξ	Heading Angle Between Initial Great Circle and Present Position of Vehicle; Downrange and Crossrange Calculations (Figure 30)

LIST OF SYMBOLS (Concluded)

SUBSCRIPTS

A	Aerodynamic Reference
AW	Adiabatic Wall
c	Control on Flight Path
e or E	Entry Conditions and Earth Reference Axes System
f	Final Condition
F&R	Fay and Riddell
ROT	Rotating
g	Local Geocentric, Horizon Reference
I	Inertial
i,o	Initial Conditions
L	Latitude
M	Modified
NROT	Nonrotating
P	Polar
W	Wall
X_e, Y_e, Z_e	Indicates Direction of Force Components in Earth-Referenced Coordinate System
1,2,3	Matrix Row Numbers
X_A, Y_A, Z_A	Indicates Direction of Aerodynamic Force Components in Wind Axes Coordinate System
X_g, Y_g, Z_g	Indicates Direction of Force Components in Local Geocentric Horizon Coordinate System

SECTION I

INTRODUCTION

The ability of high speed maneuvering vehicles to perform military missions has been a subject of interest over the last two decades. Studies have been made of concepts ranging from space transportation and on-demand rescue to boost glide maneuvering missiles. A great deal of effort has gone into the development of aerodynamic shapes for these purposes. To determine which concepts were most suited some sort of performance measure was needed. With the advent of the digital computer as a practical engineering tool a performance "footprint" as a measure of maneuvering capability was selected. This cross range-down range footprint of a vehicle concept shows the landing or impact versatility which can be gained by maneuvering in the earth's atmosphere. The footprint is directly dependent on lift-to-drag (L/D) capability of the vehicle and shrinks to the ballistic impact point in the limit where L/D = 0. Generally the first of these footprints to be studied used a constant L/D and bank angle with the footprint generated by varying the bank angle in successive cases. This was followed by a staged bank angle, i.e. bank set at a constant value until the heading changed 90° and then set to zero during the remaining glide range, again with the footprint generated by varying the constant bank portion parametrically. This staged bank approach yielded slightly larger cross-ranges than the constant bank. Variable L/D aerodynamics were also generally factored into the analysis at this time (C_L and C_D varying as a function of altitude and Mach number).

The next step in footprint development evolved with the construction of flight path optimization methods. Computer programs were generated and applied to the problem of maximizing cross-range (unconstrained). The optimization program used within the Flight Dynamics Laboratory was based on the steepest descent technique and is still available although not much used today, Reference 1. The optimum cross-range solutions obtained from this program were higher than any developed by the previous methods. However, to obtain a solution for just the maximum cross-range point on the footprint through steepest descent optimization was time consuming in terms of computer resources, and to optimize the complete

1

footprint for each vehicle and entry condition was out of the question.
Footprints were hence estimated by fairing a curve through the maximum
cross-range point and the parametric points generated by the staged bank
procedure described previously. Reference 2 contains a partial list of
references in the performance area.

The objective of this effort was to develop a reliable method for
rapidly analyzing entry vehicle performance (see also Reference 3).
Development of the control laws stressed the use of realistic vehicles
in the medium to high L/D range, that is those which are supported by
analysis and wind tunnel data, rather than hypothetical vehicles which
were much used in the past. The impact of heating considerations was
also addressed.

The approach used was to develop optimal cross-range solutions for a
footprint both without constraints and with down-range constraints.
Parameter optimization on bank angle was used to develop these solutions
using the optimization procedures described in References 4 and 5 and
the trajectory program described in Reference 6. Observation of the
variation of the optimal bank angle control schedule with respect to
turn angle then led to the development of a simplified control for rapid
footprint generation. Comparisons between the simplified control results
and the optimization results were then made for three conceptual vehicles.
Section II contains these results.

In Section III optimal solutions with heating constraints were sought
and the effect on the footprint was noted. The heating method employed
was a reference heat transfer procedure similar to that used in
Reference 7 in conjunction with the optimization and trajectory programs.
In Section IV a display concept is presented to aid in translating
footprint data to functional performance. This procedure allows plotting
and manipulating of data on world maps and can be used separately or in
conjunction with the performance calculation procedure. Study conclusions
are shown in Section V. Mathematical details are shown in Appendix A,
vehicle aerodynamics in Appendix B, and a footprint data base in
Appendix C.

SECTION II

FOOTPRINT GENERATOR DEVELOPMENT

1. REENTRY VEHICLES

Three lifting entry vehicles with maximum lift/drag (L/D) ratios of
1.89, 2.2, and 2.6, respectively, were selected for analysis. These L/D
values were measured at Mach = 20 and 200,000 feet altitude. All three
vehicles are realistic in terms of system type analysis supported by a
broad base of aerodynamic experimental data. Sketches of these config-
urations are shown in Figures 1a through 1c. Aerodynamic characteristics
used in this analysis are shown in Appendix B. These data were obtained
from References 8 through 10. The Reference 9 data were supplemented by
theoretical calculations at Mach = 10 and 20. A wing loading of 70 psf
was used for the low L/D vehicle and 40 psf was used for the other two.

2. ASSUMPTIONS

Atmospheric entry was initiated at 60 nautical miles (364,566 feet)
altitude heading east on the equator (heading σ = 90 degrees). An earth
relative velocity of 24,480 feet/second was used. This corresponds to an
inertial velocity of 26,032 feet/second, which is slightly above circular
velocity. Although aerodynamic heating considerations limits the entry
path angle corridor that is practical for lifting entry vehicles, entry
paths angles from -2.0 to -5.0 degrees were investigated for the purpose
of methodology development. An entry path angle of -2.0 degrees was
used for the purpose of footprint generator development and for trajectories
with heating constraints imposed. A rotating oblate earth with the 1959
standard atmosphere was used in the trajectory computations. Coordinated
turns (zero side-slip angle) were assumed. Unconstrained trajectories
were flown at zero bank angle to the initial pull-out altitude (γ = 0);
bank angle was then allowed to vary for the remainder of the trajectory.
Unconstrained optimal solutions and maximum cross-range under down-range
constraints used the angle-of-attack for maximum L/D. This varied with
Mach and altitude for the particular vehicle. The optimal solution with
heating constraints in Section III varied the bank angle after the initial
pull-out and the angle-of-attack over the entire trajectory.

Moment
reference
center

839

101

25

FRL

Side View
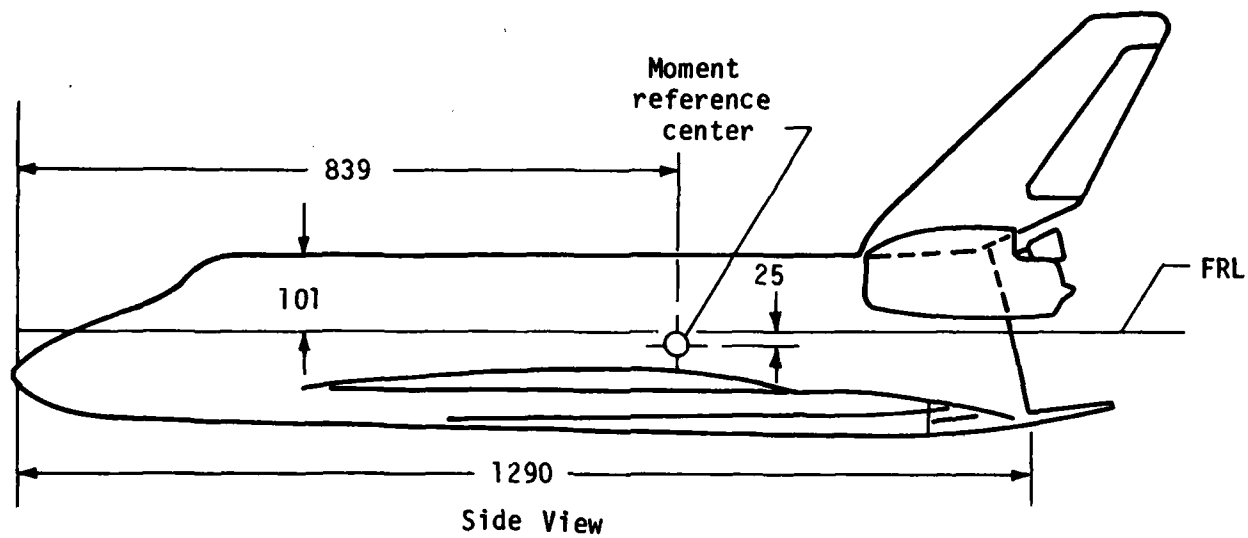
$S = 2690 \text{ ft}^2$

$W = 187,900 \text{ lb}$

$W/S = 70 \text{ lb/ft}^2$

1290

Dimensions in inches.

937

Rear view.

Figure 1a. L/D = 1.89 Configuration

4

Aileron

Body Flap

80.0

42.7

274.5

197

Strake

X=0.0

Y=0.0

Top View

All linear dimensions in inches

$S = 125.84 \text{ ft}^2$

$W = 5035 \text{ lb}$

$W/S = 40. \text{ lb/ft}^2$

54.5

Center Fin

Moment Reference Center

Y 0.0

Z -9.1

Z=0.0

Side View
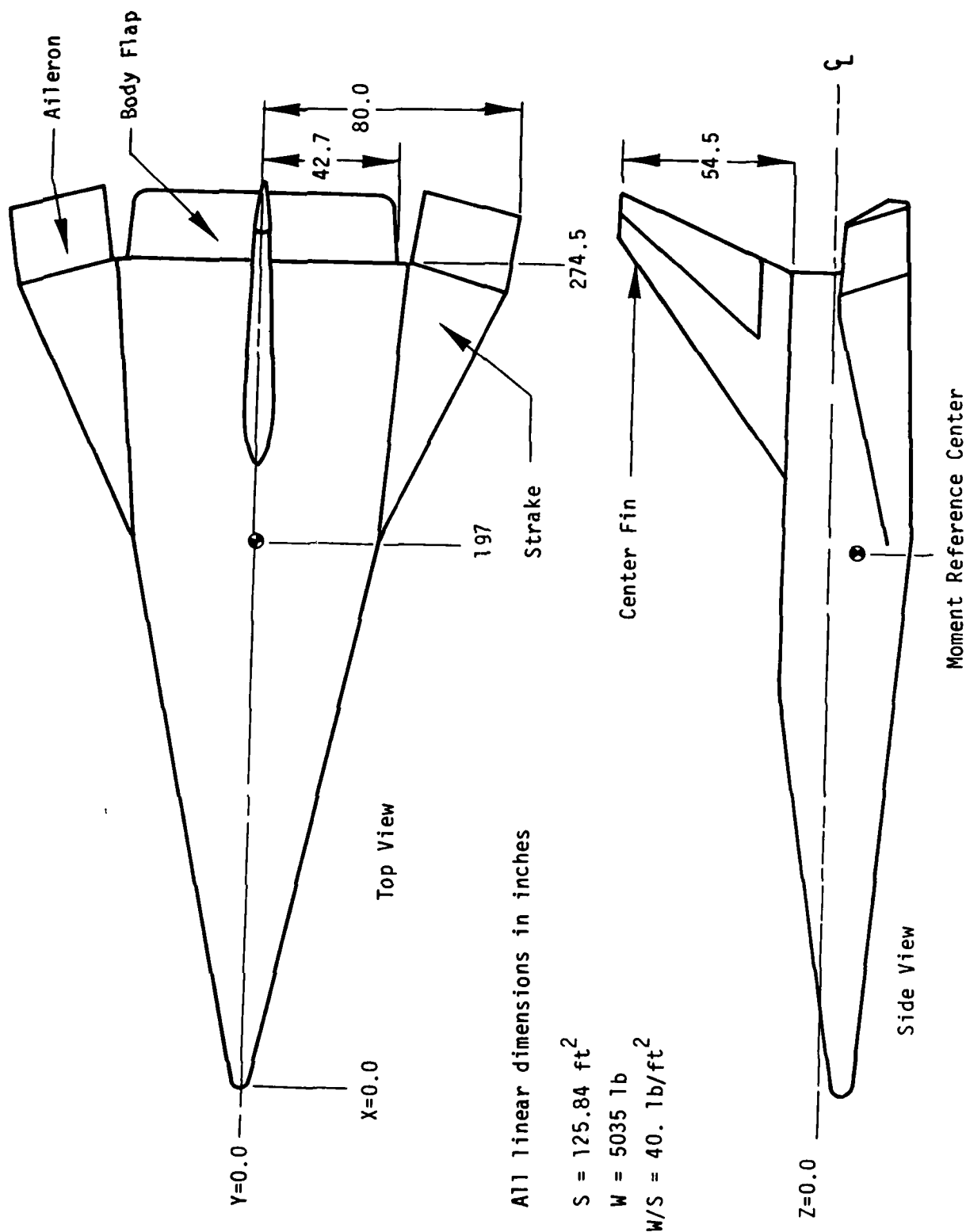
Figure 1b. L/D = 2.2 Configuration

32.1

$S = 35.38 \text{ ft}^2$
$W = 1415 \text{ lb}$
$W/S = 40 \text{ lb/ft}^2$

Dimensions in inches.

60.65

168
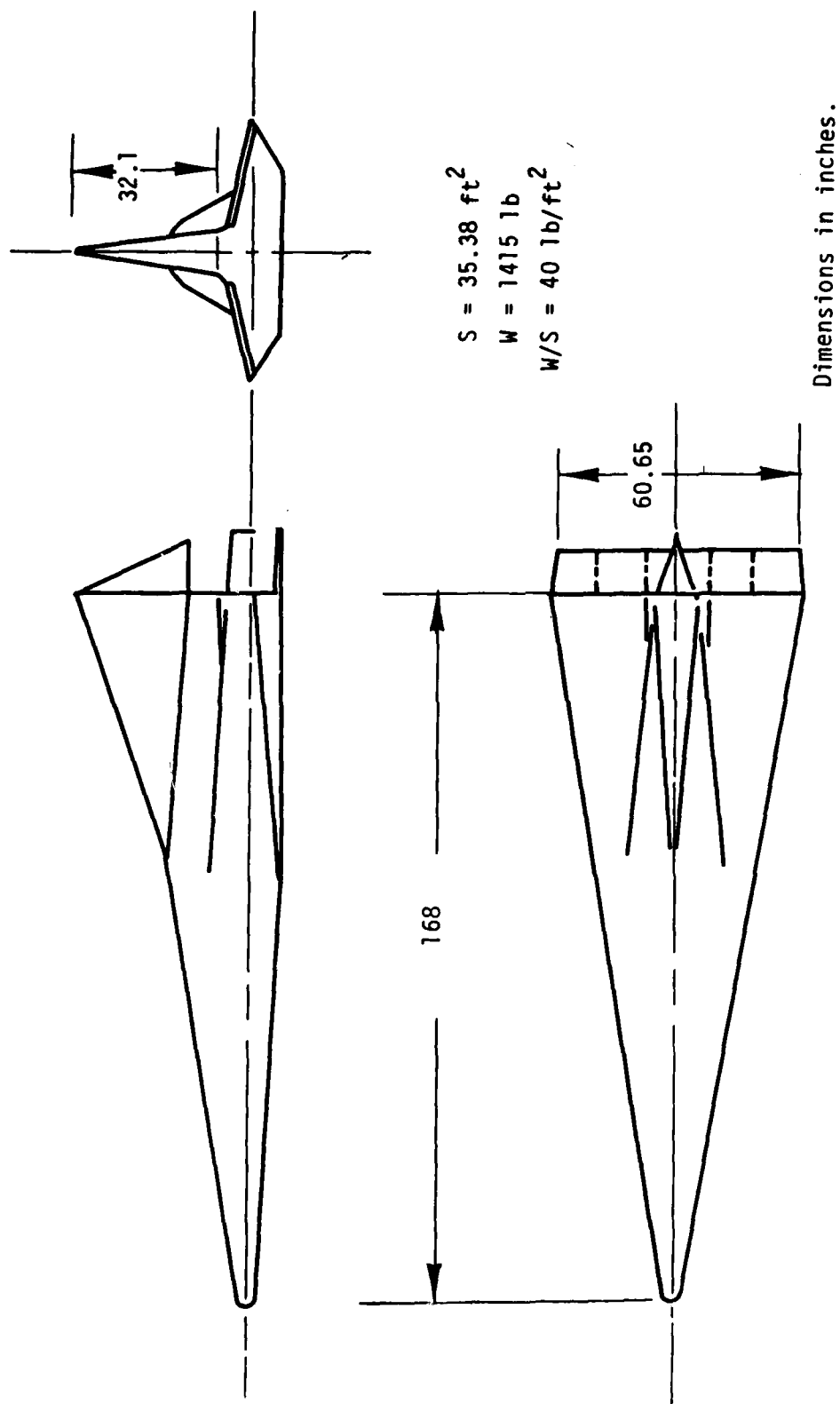
Figure 1c. L/D = 2.6 Configuration

6

3. EQUATIONS OF MOTION

The equations of motion are solved in an earth-referenced cartesian coordinate system. The relation between local-geocentric-horizon, inertial and earth-referenced coordinate systems is illustrated in the following sketch.
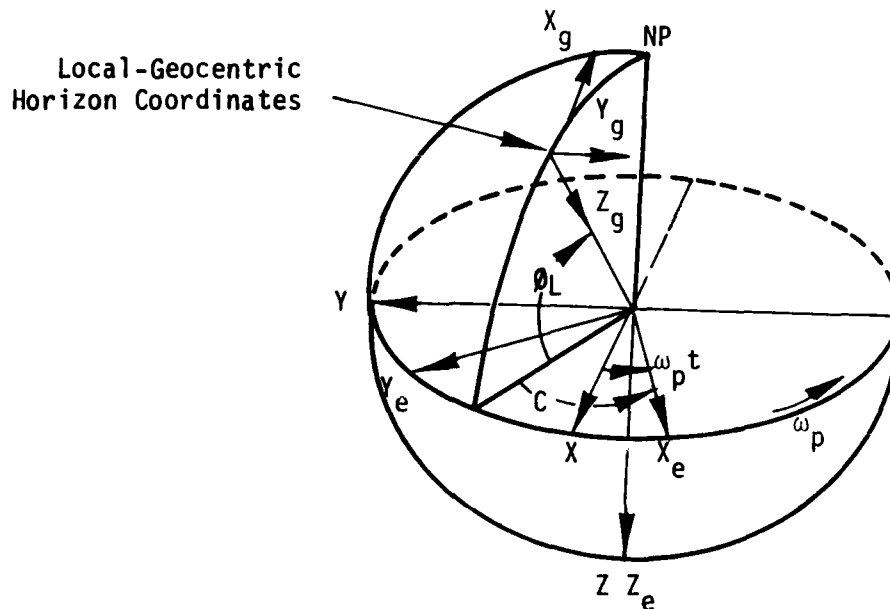
X, Y, Z,	Inertial Coordinates
X_e, Y_e, Z_e	Earth-referenced coordinates
X_g, Y_g, Z_g	Local-geocentric-horizon coordinates

The origin of these systems lies on the polar axis in the equatorial plane. The Z and Z_e axes are collinear with the polar axes and positive toward the south pole. The X_e axis is in the equatorial plane and is fixed at the longitude of the vehicle at time equal zero. The Y_e axis is positive to form a right-handed system. The inertial coordinates X,Y,Z and the earth-referenced coordinates X_e, Y_e, Z_e coincide at time zero. The earth-referenced axes rotate with the planet whereas the inertial axes remain fixed.

The equations of motion solved in an earth-referenced cartesian coordinate system are as follows:

$$\ddot{X}_e = F_{x_e}/m - 2\,\dot{y}_e\omega_p + x_e\omega_p^2 \tag{1}$$

$$\ddot{Y}_e = F_{y_e}/m + 2\,\dot{x}_e\omega_p + y_e\omega_p^2 \tag{2}$$

$$\ddot{Z}_e = F_{z_e}/m \tag{3}$$

These equations were integrated to obtain the velocity $\dot{X}_e$, $\dot{Y}_e$, $\dot{Z}_e$ and position X_e, Y_e, Z_e.

The transformations necessary to relate the axes systems employed are developed in Appendix A.

4. OPTIMIZATION PROCEDURE

The control variables used for optimization were bank angle (ϕ_B) and angle-of-attack (α). These variables were input to the computer program in tabular form as "control parameters". The parameter optimization procedures then vary these control parameters to maximize or minimize a given function. The control used by the program is formed by a linear interpolation between the discrete control parameter points varied by the optimizer. In this section, eight parameters were used on bank angle with angle-of-attack set to L/D max. Additional parameters were used on angle-of-attack when temperature constraints were considered, as will be shown in Section III.

The methods considered for parameter optimization are those described in Reference 4. After some early experimentations with these parameter optimization methods, a sequential combination of two searches was found to produce satisfactory results. This combination was an adaptive "creeping" search followed by a "pattern" search. The adaptive creeping search operates by introducing perturbations in the control parameters varying one parameter at a time seeking improvement in the function to be optimized. If improvement is not found when a parameter is perturbed

8

in one direction the other direction is searched. The size and direction
of the perturbations are determined adaptively by the search algorithm
as the search progresses. After one complete cycle of the creeping
search, with perturbations in all parameters having been explored, the
pattern search was used. The pattern search attempts to accelerate
convergence by exploring the direction revealed by the creeping search
and moves all the parameters simultaneously. The creeping search is then
repeated and followed by another pattern search, etc. Constraints are
handled by a penalty on the payoff, forming an augmented performance
function of the form:

$$\phi^* = \phi + \Sigma_i \, \omega_i (||\psi_i| - \bar{\psi}_i| - TTOL_i/2)^2 \tag{4}$$

where

ϕ is the value of the pay-off function   (cross-range used in this study)

ω_i is the weighting matrix   (unit matrix used)

ψ_i is the value of constraint i   (down-range and/or temperature used)

$\bar{\psi}_i$ is the desired value of constraint i   (down-range 2,000 - 14,000 nmi) (temperature 2550 - 2600°R)

$TTOL_i$ is the tolerance   (5° on temperature, 50 nmi on down-range)

5. CROSS-RANGE OPTIMIZATION

The controls used to maximize cross-range were angle-of-attack for
L/D max and bank angle as a function of turn angle. Figure 2 shows the
nominal control used for the bank angle. The circles show the nominal
value of the parameters used for an eight parameter optimization. The
heading angle points were selected from -15° to 90° in 15° increments.
The bank angle at these points was then varied by the optimizer. Linear
interpolation between points was used. The first problem considered was
finding maximum unconstrained cross-range. The down-range constraints
were then introduced and the problem re-run seeking maximum cross-range
under a series of down-range constraints to develop the footprint. This
process was repeated for each of the three vehicles studied.

9
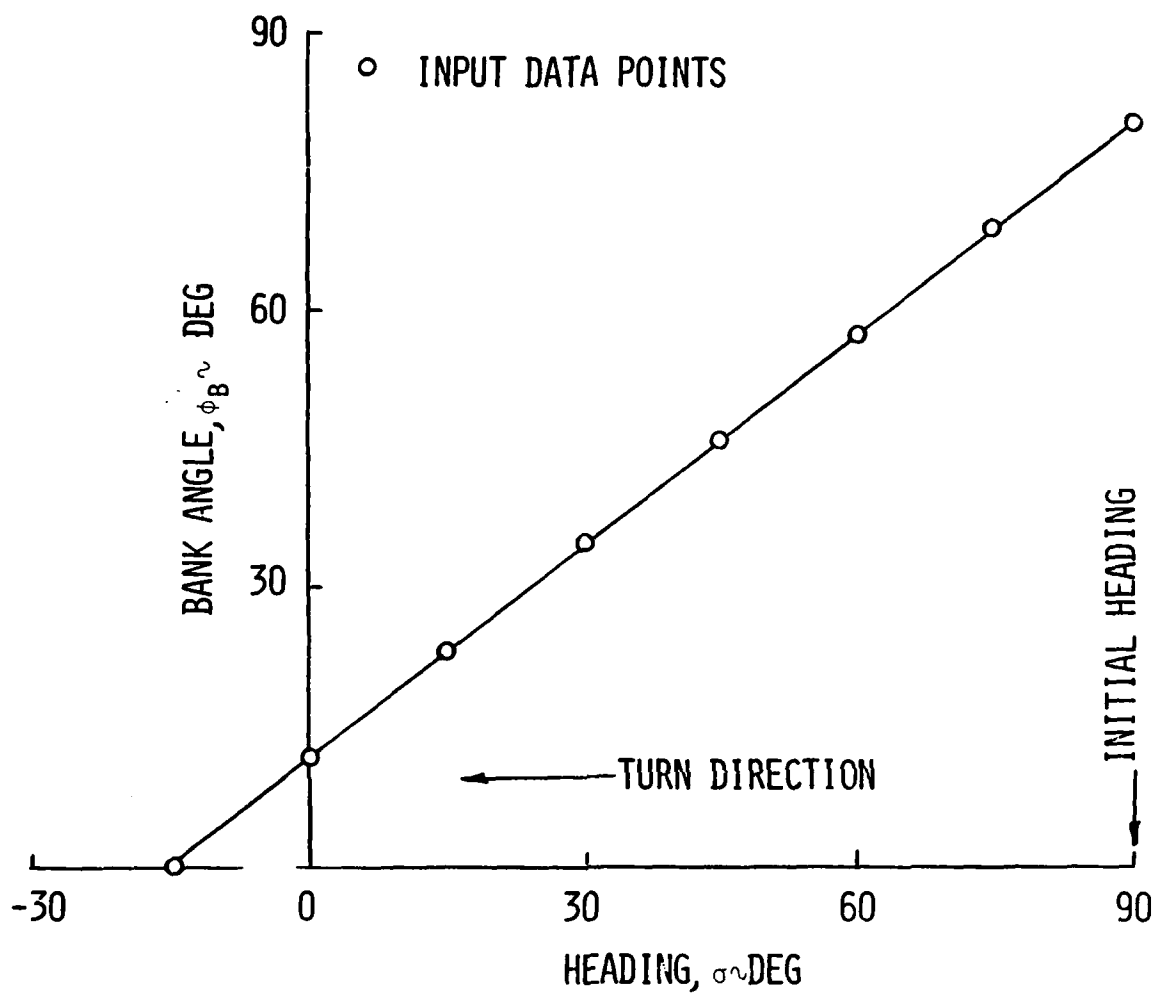
Figure 2. Bank Angle Control Schedule

Typical convergence for maximizing unconstrained cross-range is shown in Figure 3 for the L/D = 2.2 vehicle. This figure shows "steps" in cross-range at several places. These steps occur where the convergence process switches from creep to pattern. Approximately 110 iterations were used in this example. Note that over 95% of the maximum cross-range was obtained in 30 iterations. The inset to Figure 3 shows the nominal control schedule used to start the optimization and the final control determined by the optimization process.

This optimized control and the resulting controls for maximizing cross-range under down-range constraints are shown by the circles connected by the solid lines in Figure 4. The form of the control resulting from the optimization suggests that a linearization might yield satisfactory results. The control was then linearized as shown by the dashed lines in the figure and the problem re-run. The difference in cross-range between using the linearized and the optimal control was less than five percent in all cases. A two-parameter linear control was then investigated. The control used was $\phi_B = K(\sigma - \sigma_f)$ where K is the slope of bank angle versus heading, σ is the instantaneous value of heading, and σ_f is the final heading where the bank angle reduces to zero. This control is illustrated by Figure 5. In keeping the slope, K, constant and varying σ_f, a parametric control set was generated as shown in Figure 6. As shown in the figure, the maximum bank angle was arbitrarily limited to 75 degrees since this seemed to be a reasonable upper limit. Three different parametric sets were run using K values of .5, .67, and 1.0. This was done for all three vehicles and the results are shown in Figure 7. The optimum results are shown by the squares. The solid lines are fairings through the outer boundary of the parametric data. This figure shows fairly good agreement between the parametric and optimum results at the forward part of the footprint, but poor agreement at the back part. In an attempt to improve the agreement on the back part of the footprint, the two-parameter control was changed by: (1) increasing the bank angle limit from 75 to 85° and (2) by setting $\sigma_f = 0°$, which results in $\phi_B = K\sigma$. By varying the parameter K, a parametric control set was generated as shown in Figure 8. The parameter K was varied from 0. to 1.5.
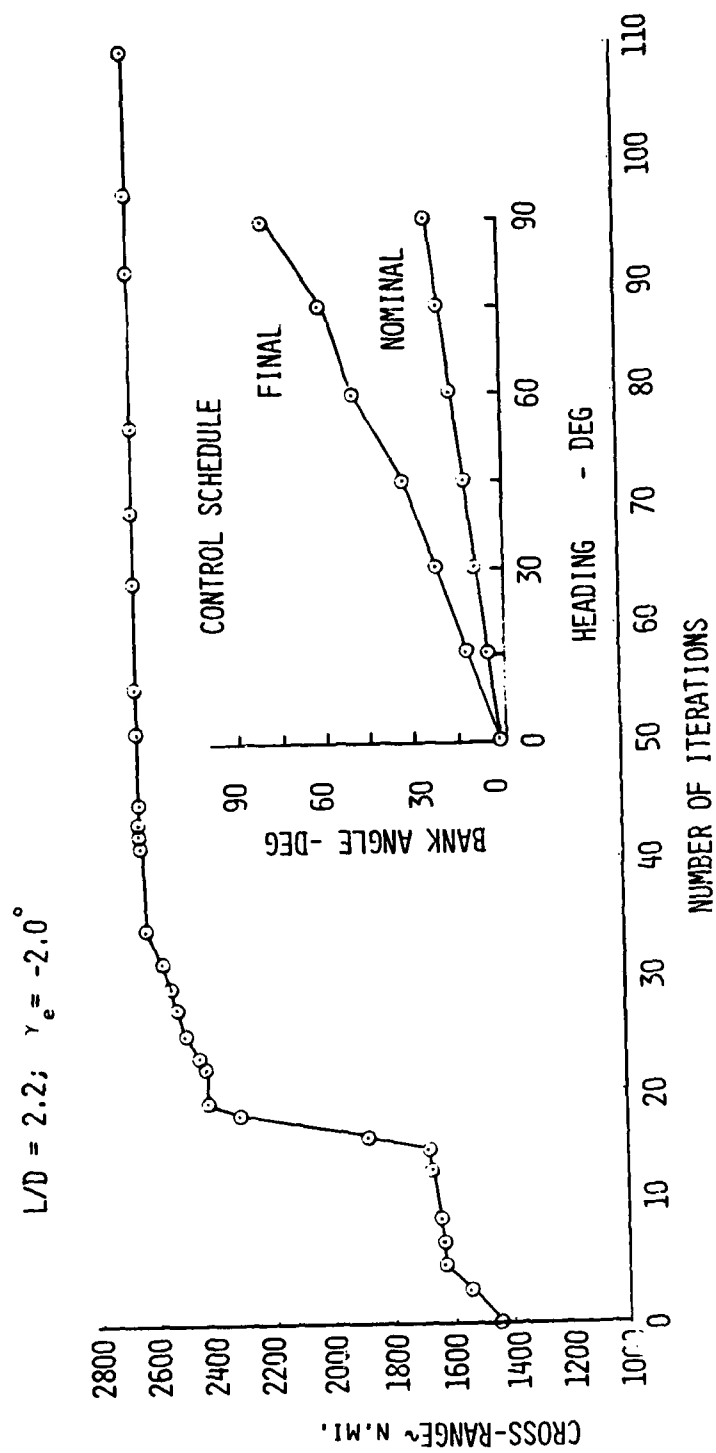
Figure 3. Convergence for Maximizing Cross-range
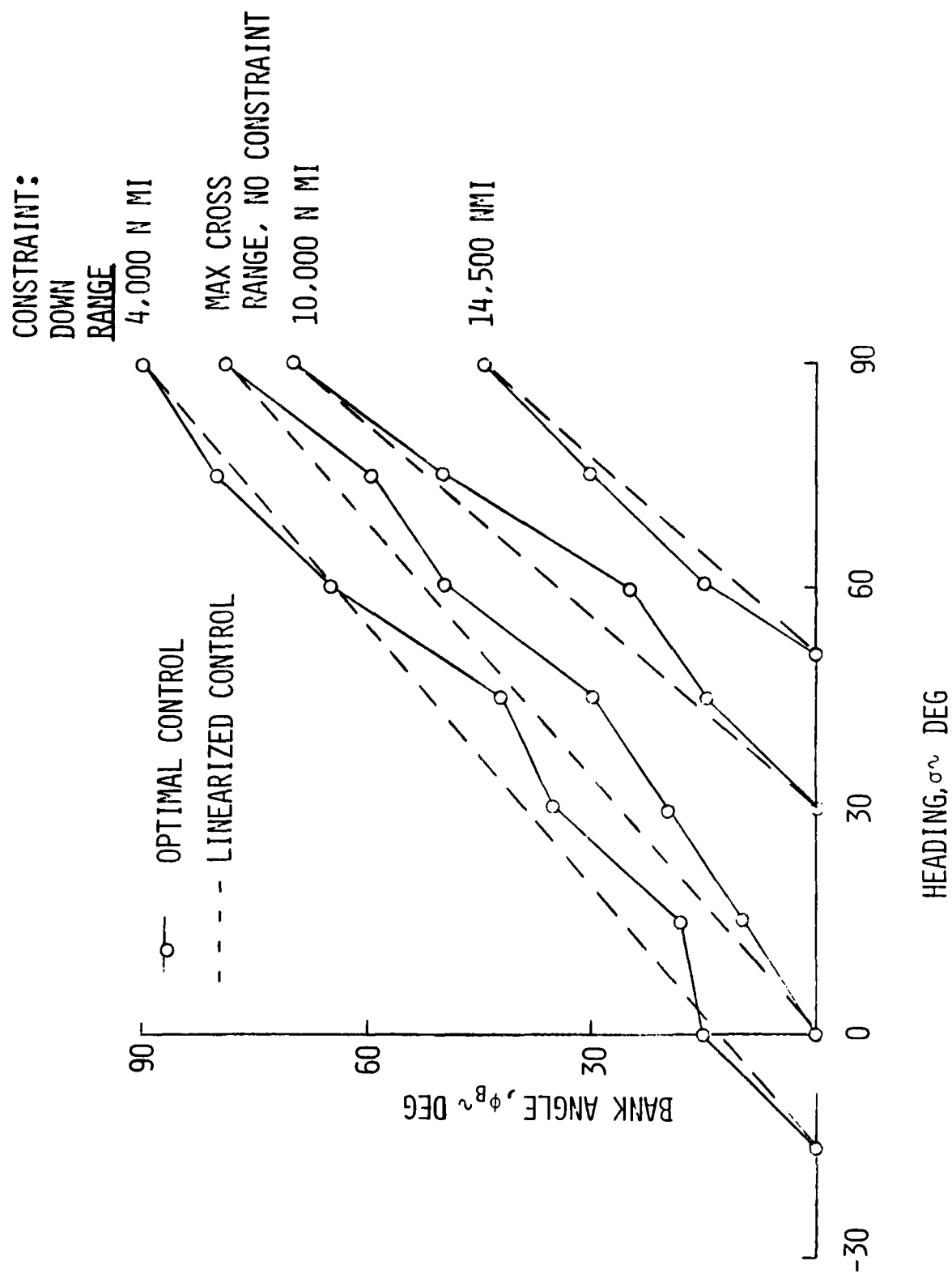
Figure 4. Optimal and Linearized Bank Angle Control

$$\phi_B = K(\sigma - \sigma_f)$$
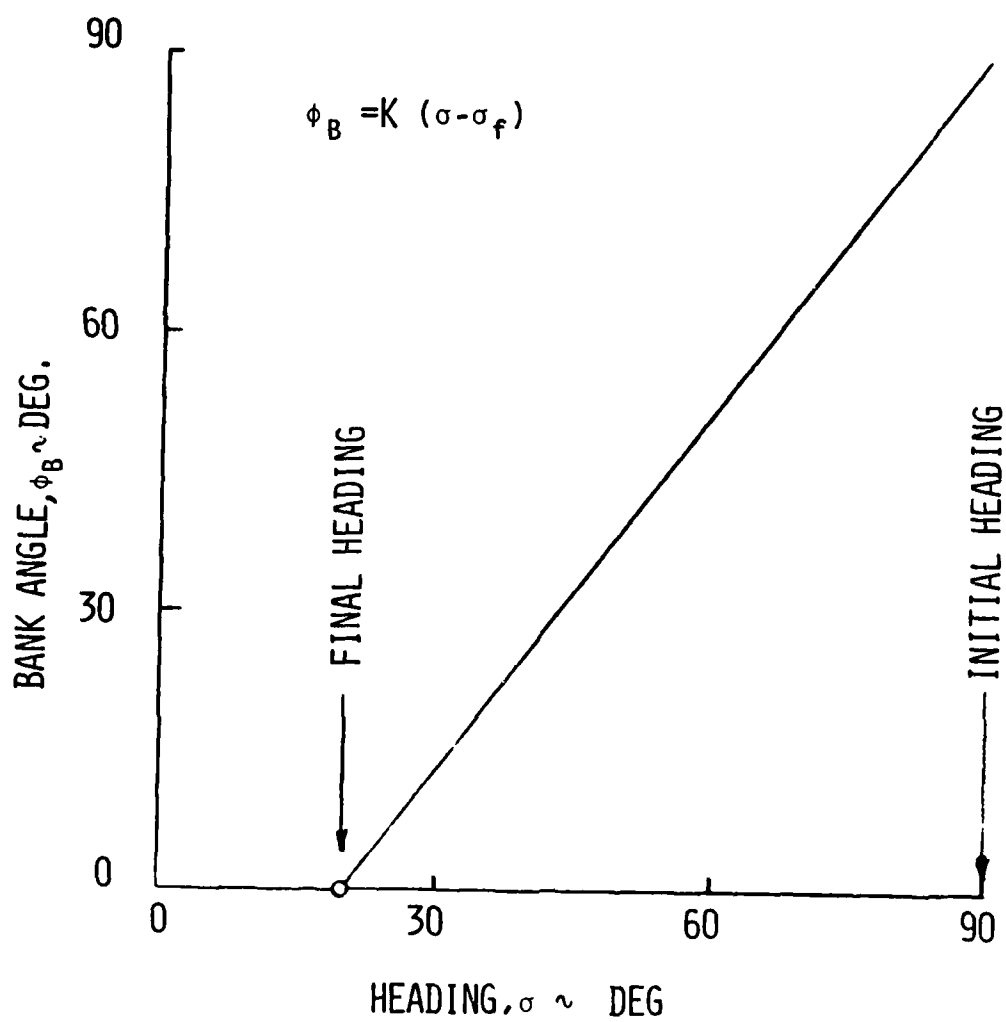
Figure 5. Two Parameter Control

14

$$\phi_B = K (\sigma - \sigma_f)$$
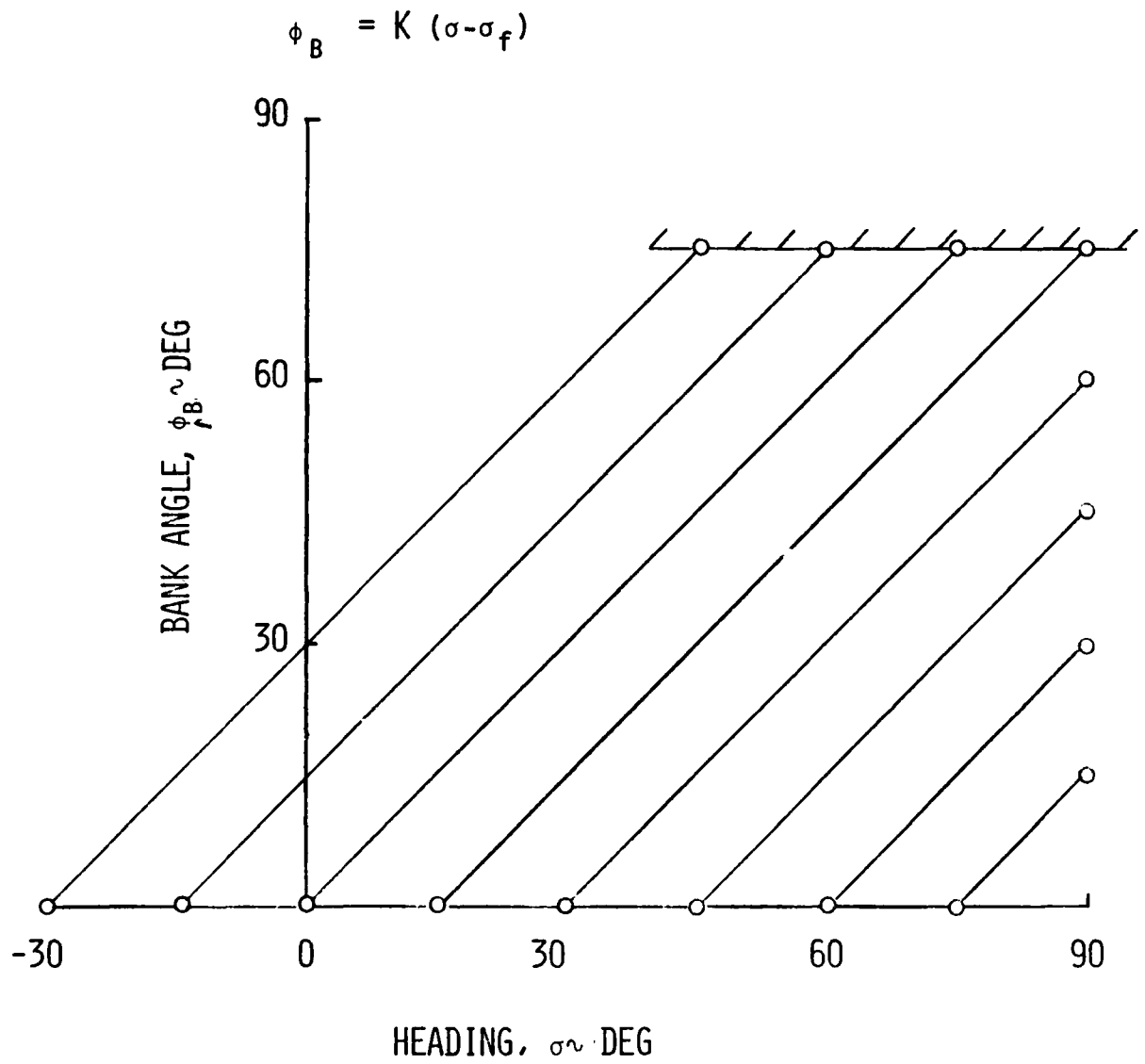
Figure 6. Two Parameter Bank Angle Control

15
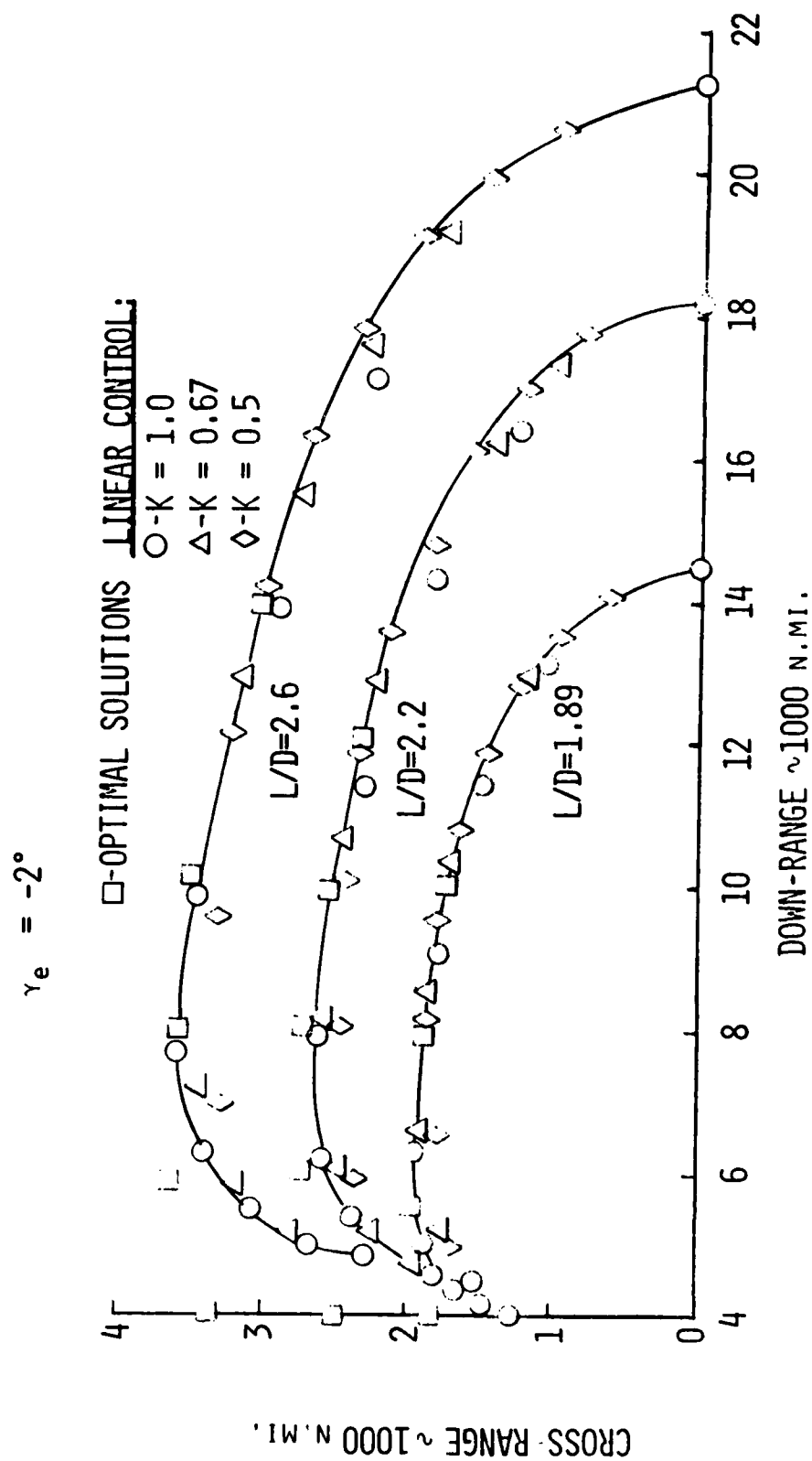
Figure 7. Optimal and Parametric Comparisons

$$\phi_B = K\sigma$$
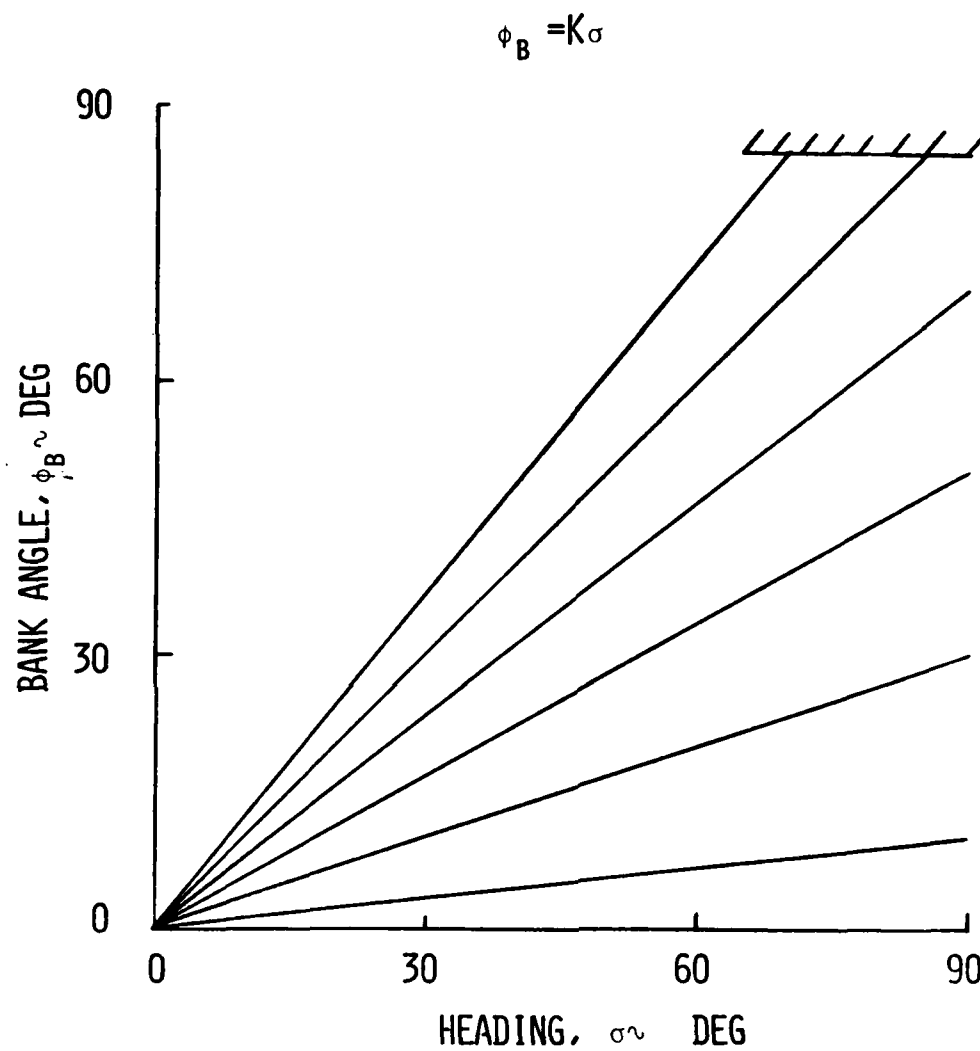
Figure 8. Single Parameter Control

17

The higher values of K (K>1.0) provide a bank angle control which initially follows the 85° boundary (Figure 8) and then is reduced linearly to zero as the turning angle approaches 90° (σ = 0). This type of control results in fast initial turning and short down-range. The results are shown by the circles in Figure 9. The squares are again the optimized results and the solid lines are the results from the previous parametrics. The figure shows that the results from the ϕ_B = Kσ control compare closely over the entire region with both the optimized results at the short to mid ranges and with the best cross-range achieved by the previous parametrics at the longer ranges for all three vehicles being studied. Use of the bank control equation ϕ_B = Kσ is called a "single parameter" control as K is the only parameter being varied.

6. FOOTPRINT GENERATION

The footprint generator development thus far has dealt with maximizing cross-range for the portion of the footprint that has down-ranges of 4000 nmi and greater. Attention is now given to ranges of less than 4000 nmi. Using the L/D = 1.89 configuration, the cross-range was maximized using the optimization process where down-range was constrained to 3000 and then 2000 nmi. The resulting optimal bank angle controls are shown in Figure 10 for these ranges plus the 4000 nmi range developed previously. It was found that these results could be closely approximated using the linear control ϕ_B = Kσ if the maximum bank angle limit were removed, i.e., allowing the vehicle to bank greater than 85 degrees. The results are shown in Figure 11. Note that all trajectory data points were run at (L/D) max except for the zero lift data point. Complete footprints for the three configurations are shown in Figure 12. This figure shows good agreement between the optimal results shown by the hexagonal points and the single parameter control solutions.

From Figure 12 each footprint was generated with 13 points, each point requiring a trajectory. In contrast, each of the optimization points shown in the figure represents about 110 trajectory iterations before converging to a solution. Forming part of a footprint using three optimized points would require about 110 X 3 = 330 trajectories.
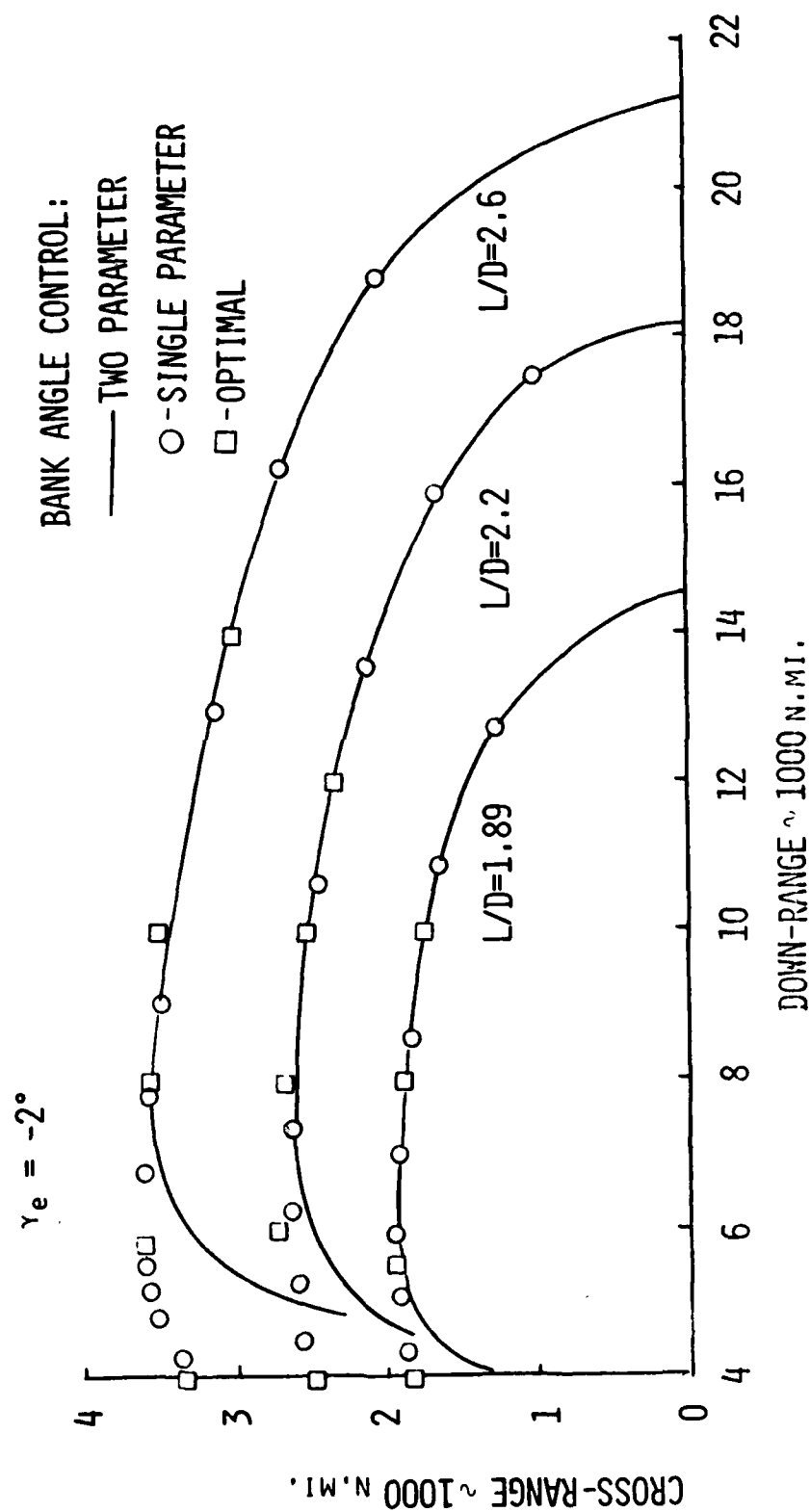
Figure 9. Optimal and Parametric Comparisons
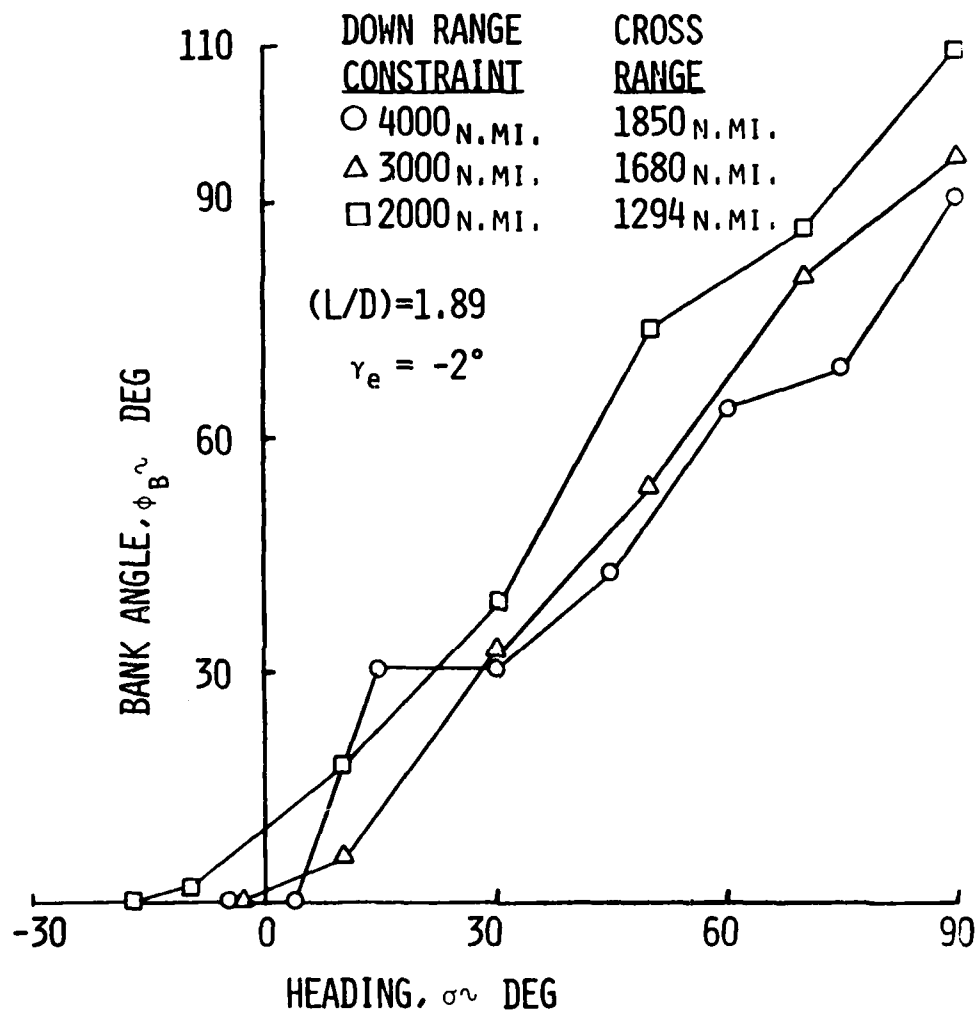
Figure 10. Optimal Bank Angle Schedules
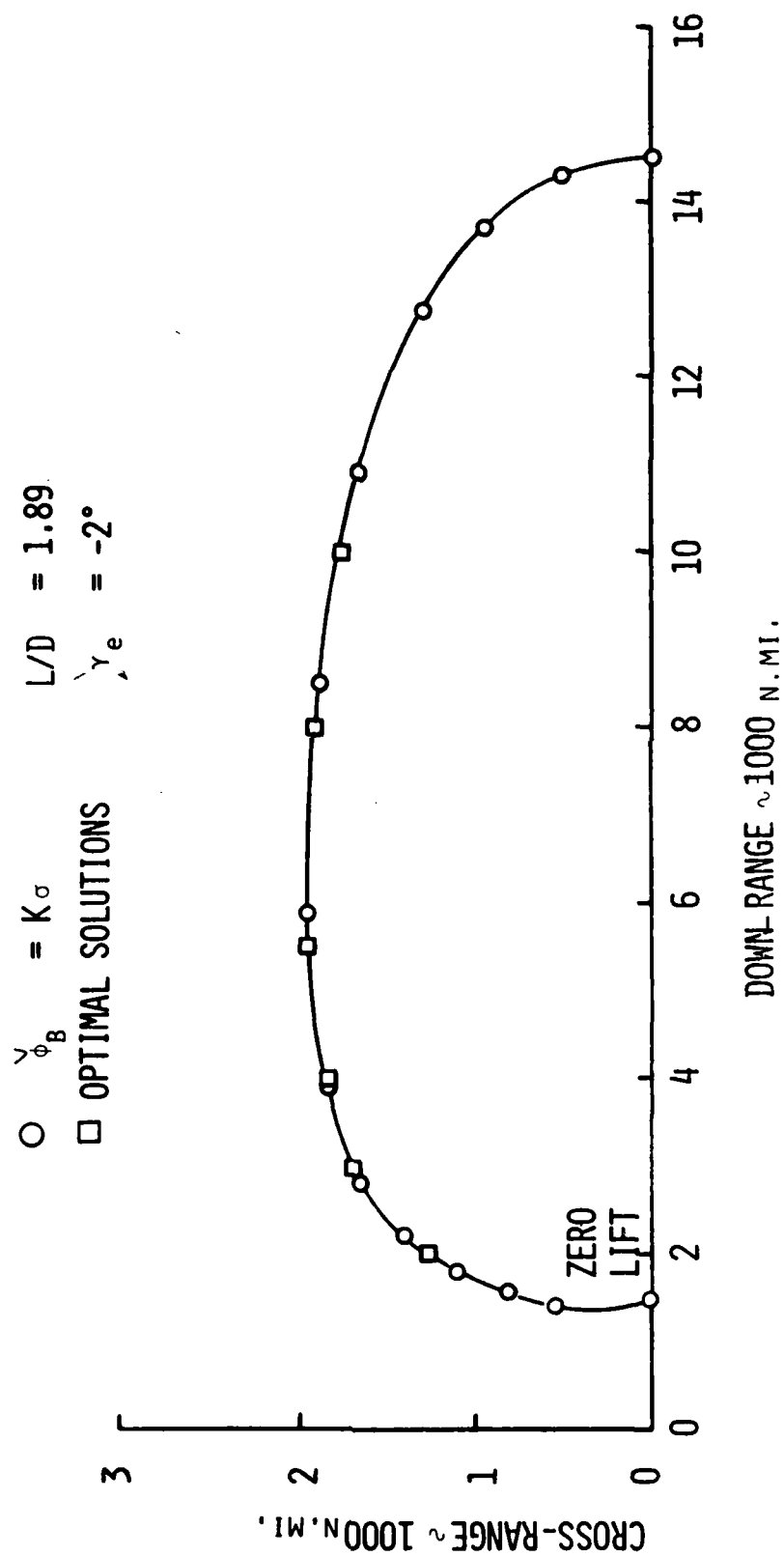
Figure 11. Comparison of Optimal and Parametric Data
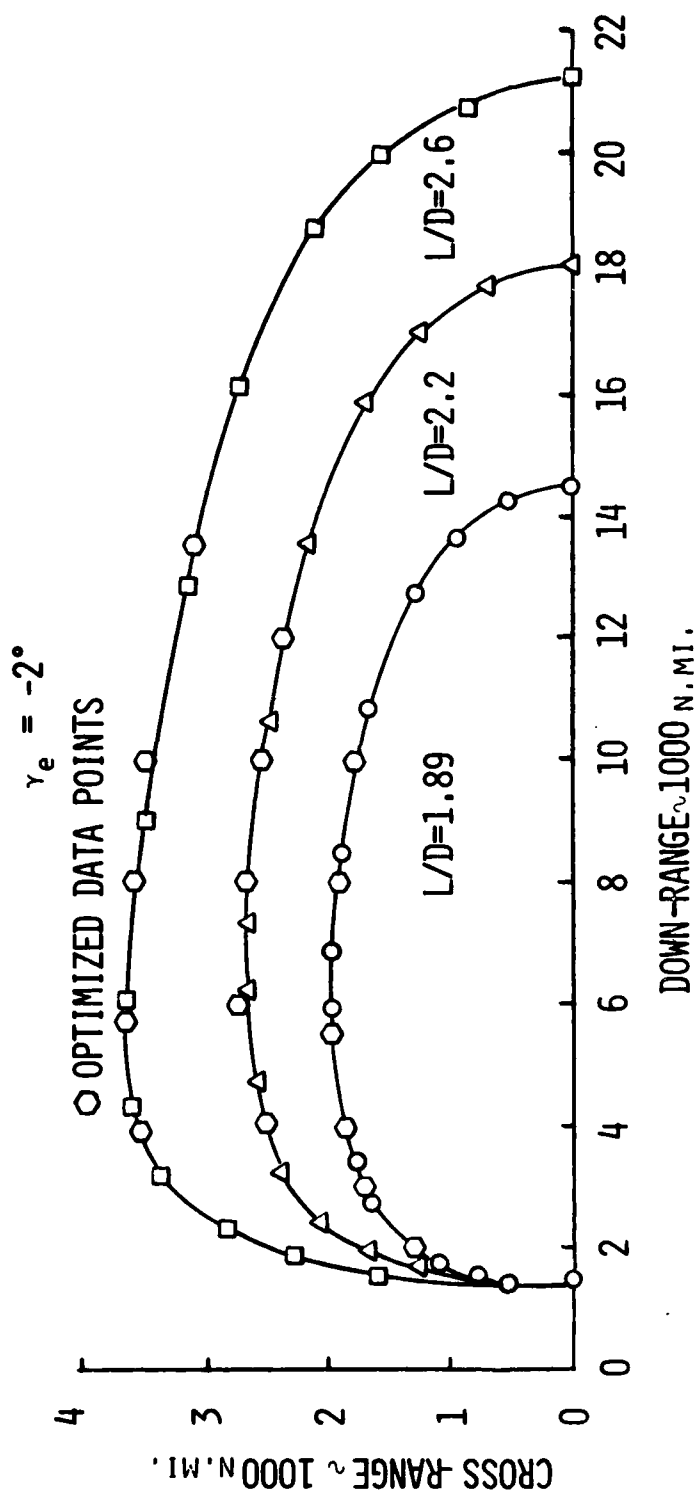
Figure 12. Optimal and Parametric Comparisons

Use of the linear control to produce a complete footprint hence requires less computer resources by a factor of 330/13 = 25. Converting this to computer solution time using an average of 30 seconds computer time per trajectory on a CDC CYBER-175 yields a decrease in time from 9900 seconds for the three optimized points to only 390 seconds for the complete footprint using the linear control.

Summarizing then, developing a footprint by the single parameter control procedure was found to closely approximate optimization results for the vehicles studied. The procedure outlined below is for an initial equatorial orbit heading east. For other inclinations, ζ (remaining heading change) must be substituted for σ in the bank angle control, where ζ is the angle between the component of the velocity vector parallel to the earth and the cross-range axis. Single parameter control procedure:

a. The initial heading and position are set. For the equatorial orbit heading east, σ = 90 degrees and the position is fixed on the equator.

b. The independent variable for the bank angle control is heading, σ (or in general ζ). Two points are required, one at the beginning (σ_0) and one at the end (σ_f) of the turn (for initial equational orbits σ_f = 0). Linear interpolation between these points forms the bank control.

c. The initial bank angle (at σ_0) is varied parametrically in 15-degree increments from 0 to 150 degrees to form the footprint. The final heading angle σ_f is 0; hence the term "single parameter control" as only the bank angle at σ_0 is being varied to form the linear control.

d. One more point (minimum down-range) is needed to complete the footprint. In this study the minimum down-range point was run at zero lift (pull downs were not considered).

7. SOME COMPARISONS AND PERTURBATIONS

The remaining work to be discussed involves the comparison of various entry conditions and control schedules. Figure 13 shows how the footprint
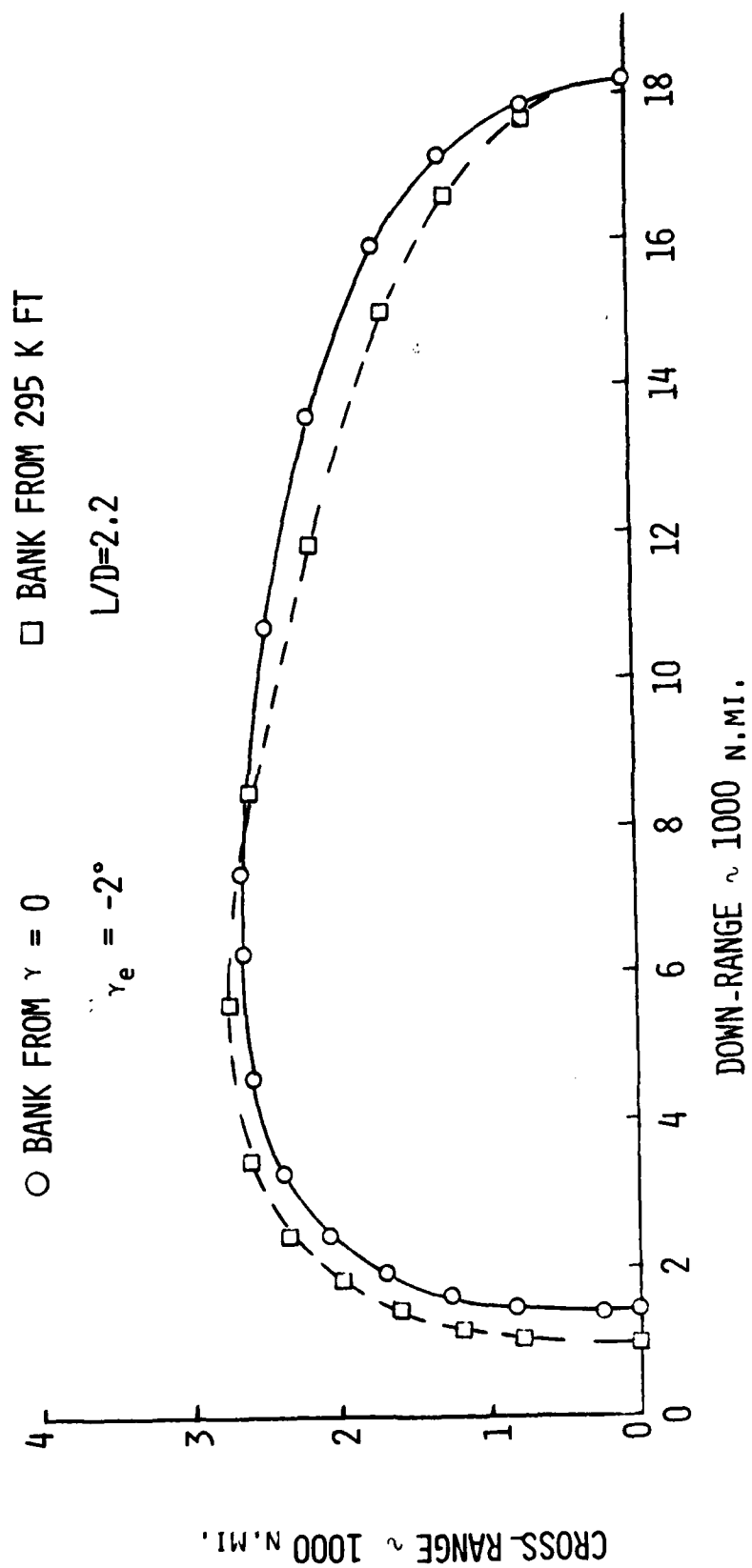
Figure 13. Effects of Bank Initiation on Footprint

changes due to initiating bank at the beginning of the sensible atmosphere, 295K ft, and at pull-out, $\gamma = 0$. Both footprints were generated using the single parameter control schedule and the L/D = 2.2 vehicle.

A bank angle control schedule much used in the past for footprint generation was to hold a constant bank angle until the heading changed by 90 degrees and then reduce the roll to zero. By varying the amount of bank, a footprint is generated. Figure 14 compares a footprint using this type of control with the single parameter control. For this case the L/D = 1.89 vehicle was used.

The effect of initial path angle on the footprint area available is shown in Figure 15 for the L/D = 1.89 vehicle. The single parameter control was used to generate this plot. The corresponding pull-cut altitudes, $\gamma = 0$, are shown in Figure 16. It should be noted that for a given set of entry conditions the initial pull-out altitude is a function of the parameter $W/(C_L S)$ rather than L/D. The Figure 16 data are for entry at L/D max, and the altitudes shown are approximately the same for the L/D = 2.2 and L/D = 2.6 vehicles. The pull-out altitude can vary appreciably depending upon the angle-of-attack schedule used during entry. The lower the value of $W/(C_L S)$ the higher the initial pull-out altitude will be. This ~ illustrated by Figure 17 which shows entry trajectories flown both at C_L max and at (L/D) max to the pull-out point, $\gamma = 0$. This figure shows that the C_L max entry, having a lower value of $W/(C_L S)$, results in pull-out at an appreciably higher altitude than the (L/D) max trajectory. Range is also increased for the C_L max entry for the case where altitude is held constant after pull-out.

Trajectories that are flown at L/D max or at a constant angle-of-attack typically oscillate in altitude. These oscillations can be damped using bank angle and/or angle-of-attack control. To maintain leve¹ flight after pull-out, the lift is reduced such that the lift plus the centrifugal force is equal to the weight. For straight down-range (no bank) the angle-of-attack is reduced to the proper value at pull-out and is increased as the speed decreases due to aerodynamic drag. The angle-o⁻-attack for

$L/D = 1.89$ $\gamma_e = -2°$

$\phi_B = K_\sigma$, L/D MAX

CONSTANT BANK, L/D MAX

CONSTANT BANK, $\alpha = 40°$

DOWN-RANGE ~ 1000 N.MI.

CROSS-RANGE ~ 1000 N.MI.
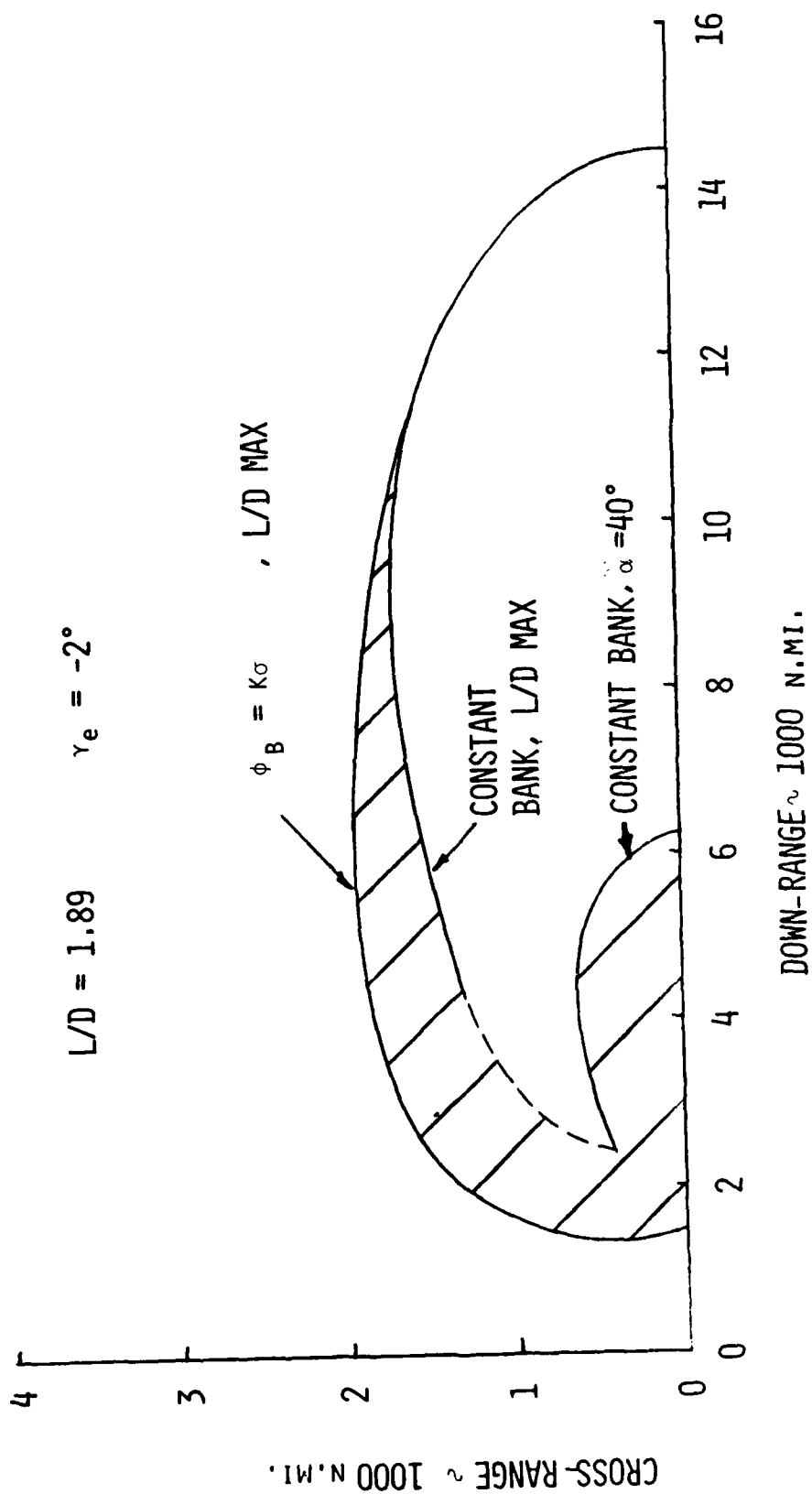
Figure 14.   Comparisons of Single Parameter and
Constant Bank Angle Controls

L/D = 1.89
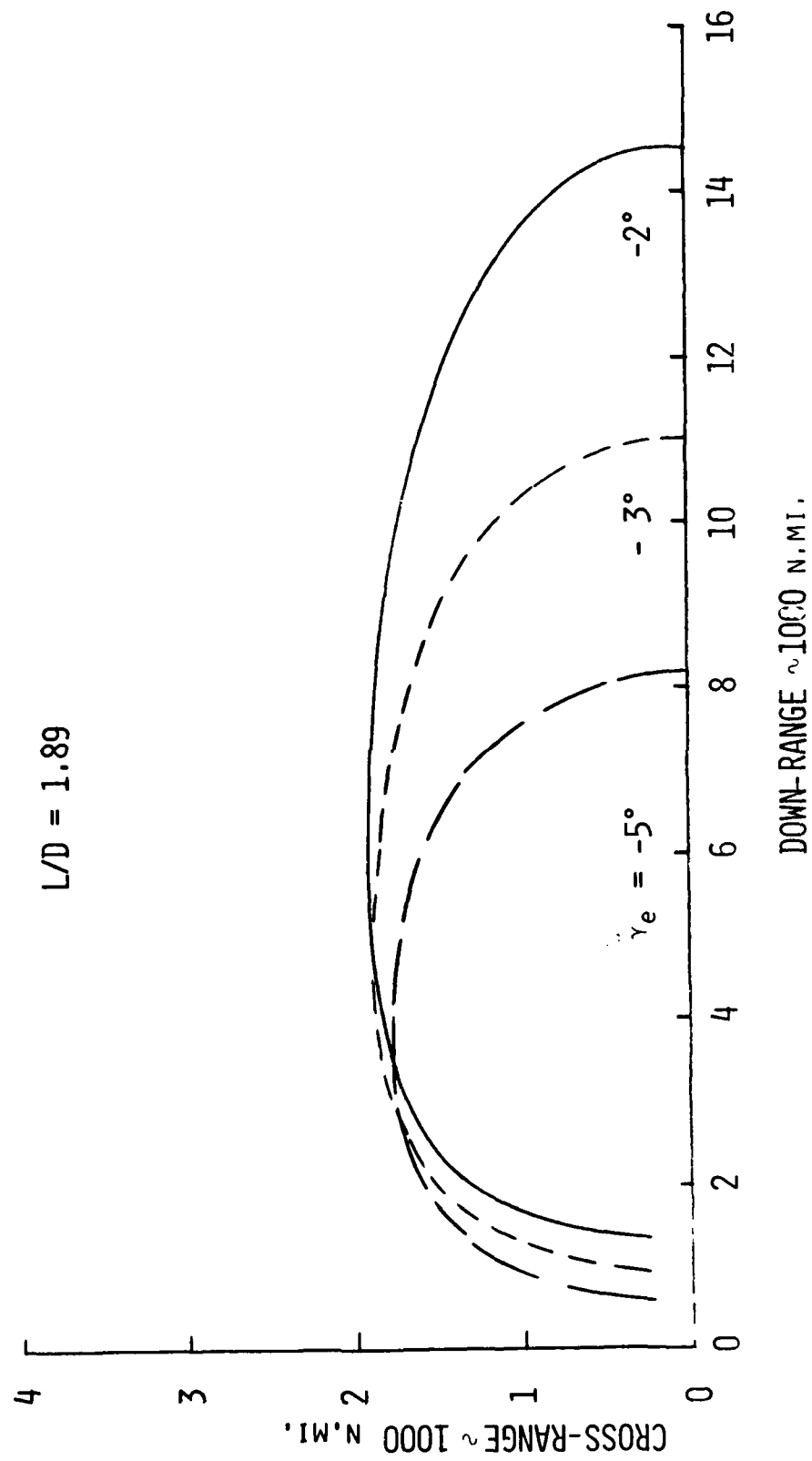
Figure 15. Effects of Initial Path Angle on Footprint
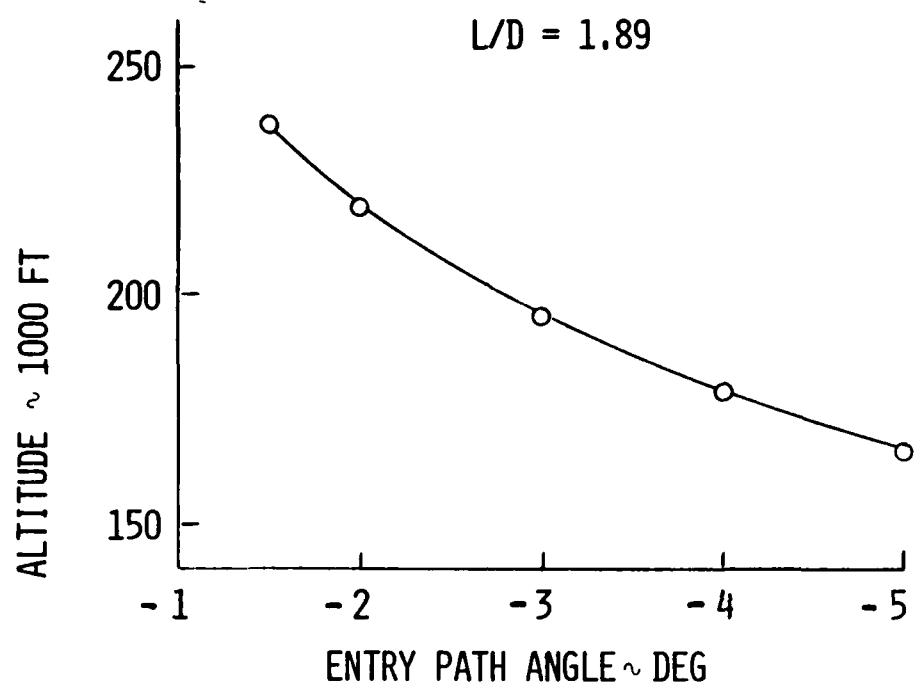
Figure 16.   Initial Pull-out Altitude

(L/D) = 2.6 γ_e = -5°
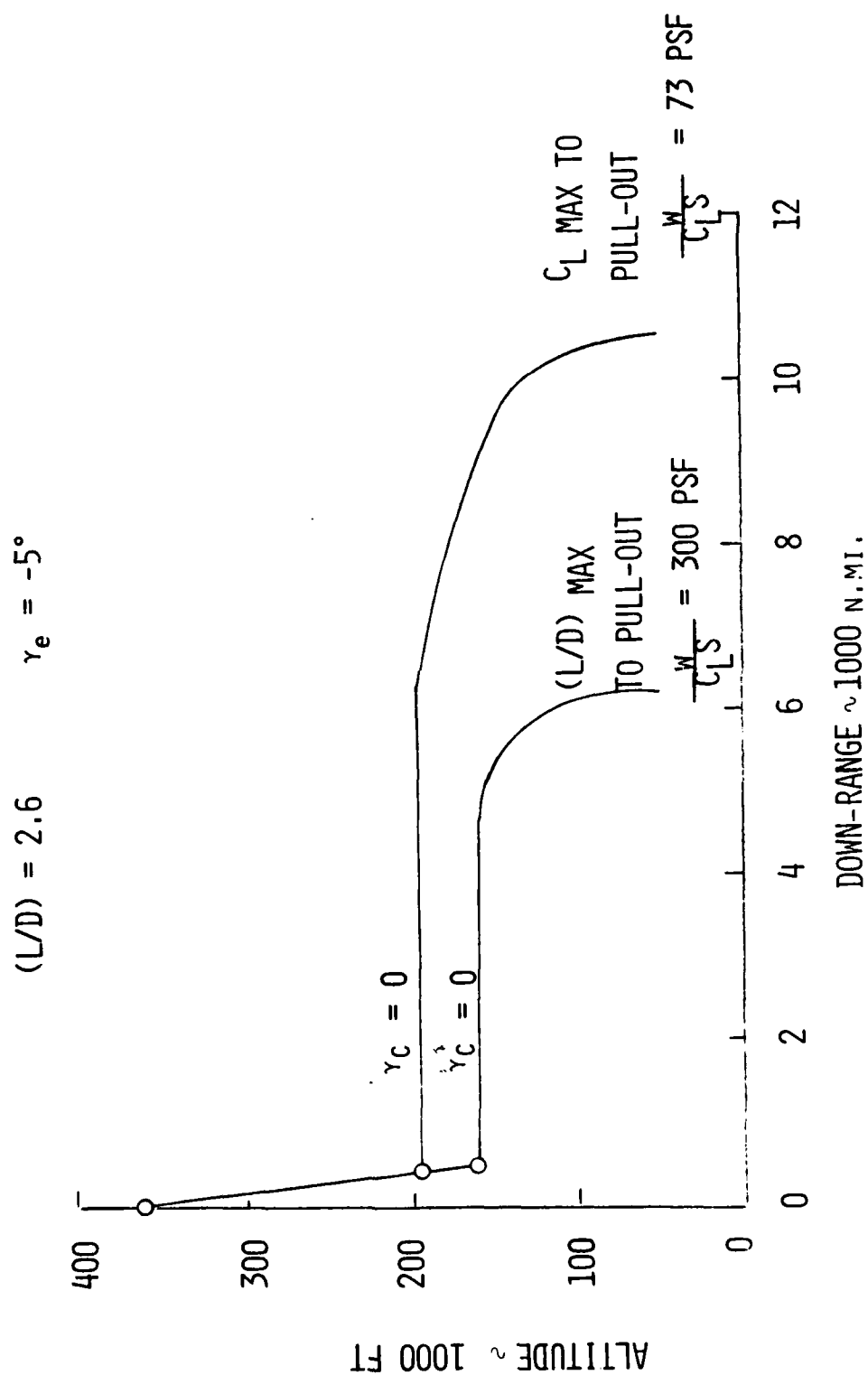
Figure 17. Comparison of C_L Max and (L/D) Max Pull-out Trajectories

L/D max is flown once the L/D max equilibrium glide trajectory is reached. In the equilibrium glide trajectory the vertical forces (lift plus centrifugal force) nearly equal the gravitational forces and hence the vehicle descends without altitude oscillations. One disadvantage of this type of trajectory is a great reduction in range since only a small part of the profile is flown at L/D max. Other variations for smoothed trajectories would be to raise the pull-out altitude by flying at C_L max until pull-out and/or flying a very small positive or negative path angle after pull-out. The effects of flying small controlled flight path angles after pull-out are shown in Figure 18. This figure also shows the (L/D) max trajectory for comparison.

Cross-range can be obtained either at constant altitude or at small flight path angles afer pull-out by using bank angle control and (L/D) max for the turn. By rolling out to wings level and switching to angle-of-attack control once a given heading change is reached, a footprint can be generated, as shown by Figure 19. The maximum amount of turn available is to maintain the turn using bank control until the wings are level. This is shown by the dashed lines in Figure 19. The altitude profiles for the down-range points with no turn in Figure 19 are the same as those shown in Figure 18 for corresponding values of the flight path angle control, γ_c.

The single parameter control and the constant altitude control have been used to generate a footprint data base. These data are shown in Appendix C.
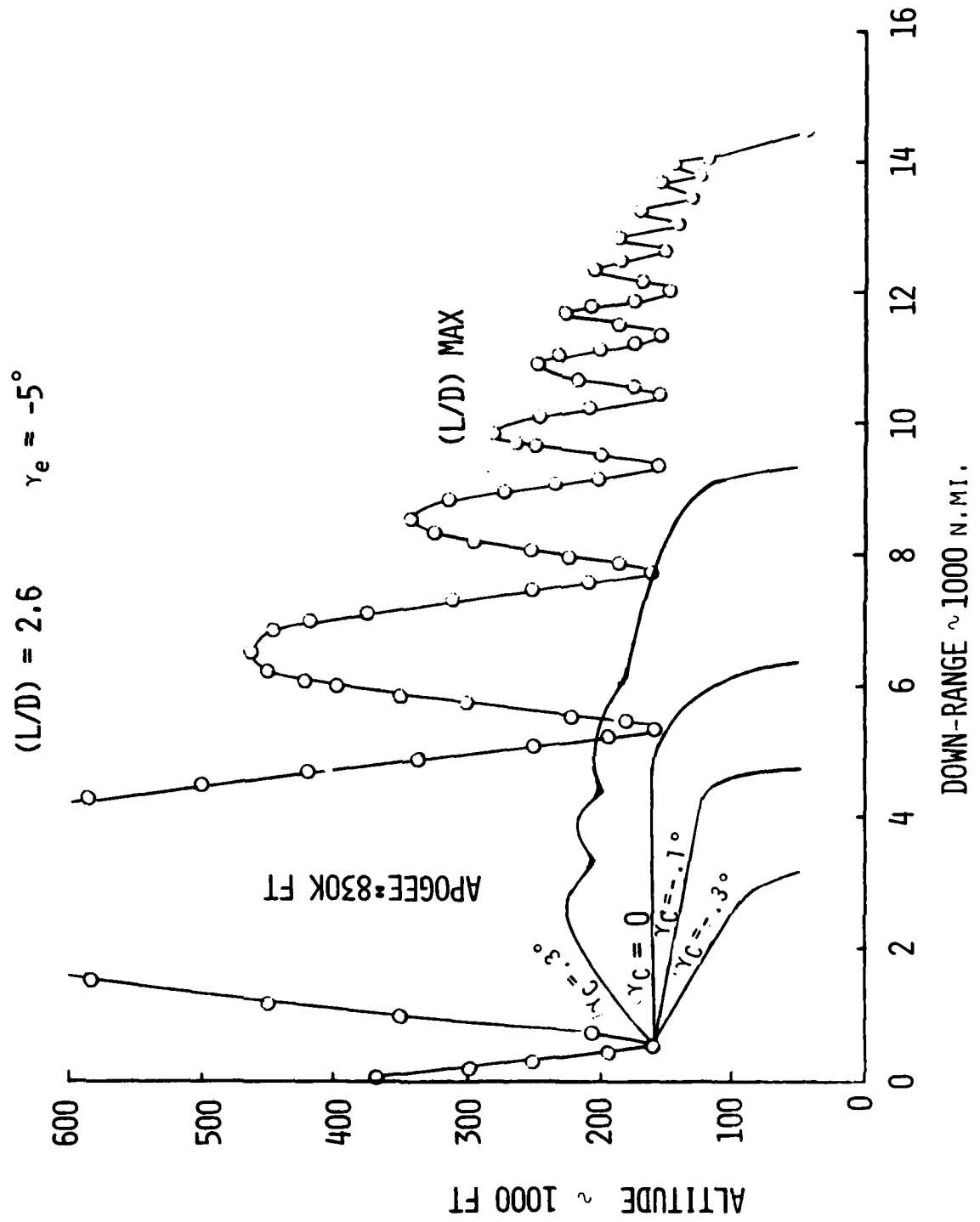
Figure 18. Comparison of Smoothed and (L/D) Max Trajectories
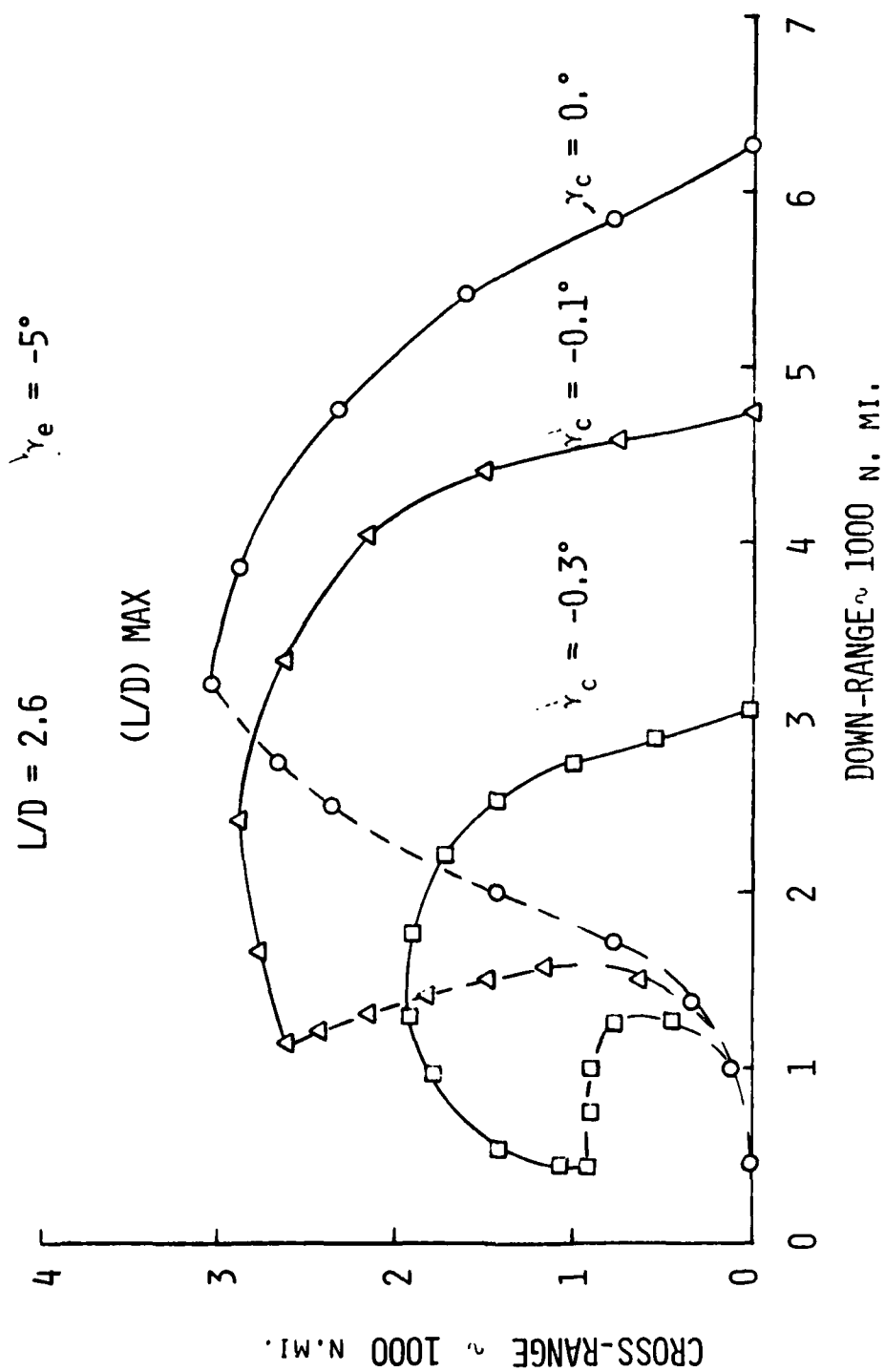
Figure 19. Lateral Range Using Bank Angle Control

SECTION III

IMPACT OF HEATING CONSIDERATIONS

In an effort to assess the impact of aerodynamic heating constraints on entry vehicle maneuvering capability, the low (L/D) configuration was selected for study. The temperatures discussed in this section were computed at a point approximately ten feet aft of the nose on the lower surface centerline of the vehicle using a one-dimensional conduction analysis on a simplified structure.

1. APPROACH AND PROCEDURES

The approach used was to calculate the heat input to the surface through the use of a "reference" heat transfer coefficient which accounted for the location of the vehicle on the entry trajectory (altitude and velocity) and a ratio of local-to-reference heating coefficient to account for vehicle attitude and point of interest on the vehicle. This approach is similar to that used in Reference 7. The following heating relationships were used to compute the radiation equilibrium wall temperature.

$$(h/h_{F\&R}) = f(\alpha) \tag{5}$$

$$\dot{q} = h_{F\&R} \ (h/h_{F\&R}) \ (H_{AW} - H_W) \tag{6}$$

$$T = [\dot{q}/(4.75 \times 10^{-13} \times \epsilon)]^{.25} \tag{7}$$

where the ratio $(h/h_{F\&R})$ is obtained from theory or wind tunnel data correlations and $(h_{F\&R})$ is calculated using the Fay and Riddell theory. Values of $(h/h_{F\&R})$ with vehicle attitude used in this study are shown in Table 1.

To maintain continuity, the same parameter optimization techniques used previously, namely "creep" and "pattern", were used for the heating analysis. To provide the capability for constraining the equilibrium wall temperature to specified values, the same penalty function approach used previously for the down-range constraint was employed.

TABLE 1

HEATING VARIATION WITH VEHICLE ATTITUDE

$(h/h_{F\&R})$	α
.17	0
.175	20
.20	25
.23	30
.23	40
.26	45
.30	50

The control philosophies employed to generate the unconstrained and temperature constrained reentry footprints are outlined in Figure 20. For the unconstrained footprint (no heating constraints), problems were formulated whereby the vehicle flew an angle-of-attack schedule for maximum lift-to-drag ratio over the entire reentry trajectory. A bank angle of zero degrees was maintained from entry to the initial flare point (γ=0 degrees). From the initial flare point to trajectory termination (H=50,000 feet), the program modulated the bank angle to maximize the cross-range. For the temperature constrained problems, both of the control parameters were modulated over the entire trajectory with the exception that during the initial plunge into the atmosphere the bank angle was set to zero degrees. Using this steering philosophy ensured that the heating criteria would not be violated at any point along the entry flight profile. Listed in Table 2 are the initial entry conditions used for the aerodynamic heating analysis.

L/D = 1.89; $\gamma_e = -2°$

CONTROL PHILOSOPHIES		
	UNCONSTRAINED	CONSTRAINED
FROM ENTRY TO INITIAL FLARE ($\dot{\gamma} = 0$)	α = (L/D) MAX $\phi_B = 0$	α MODULATED $\phi_B = 0$
AFTER INITIAL FLARE	α = (L/D) MAX ϕ_B MODULATED	$\alpha \& \phi_B$ MODULATED

CONSTRAINED TRAJECTORY

UNCONSTRAINED TRAJECTORY

ALTITUDE (10^5 FT)

TIME ~ SECONDS
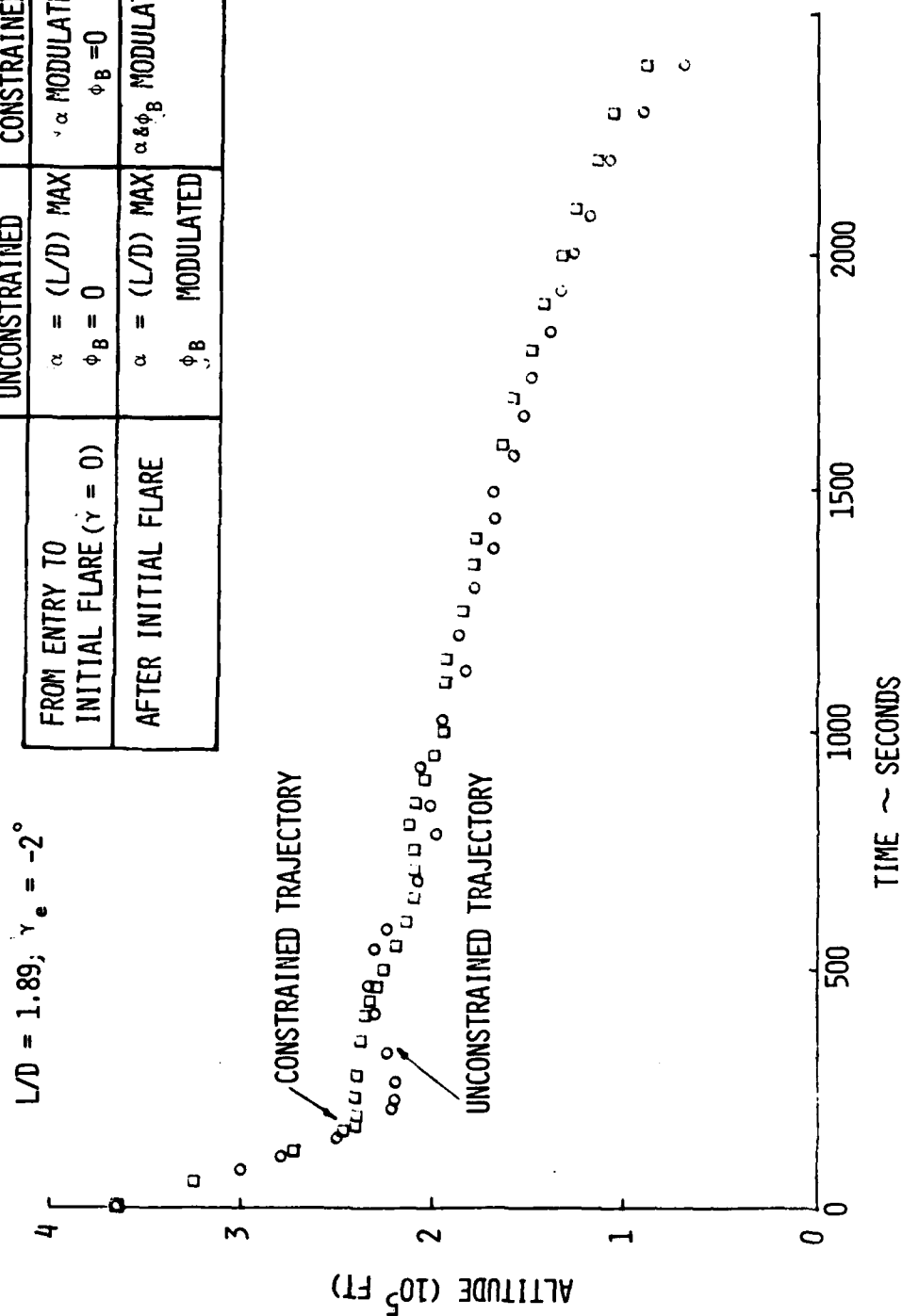
Figure 20. Control Philosophies Used for Reentry Trajectories

TABLE 2

INITIAL ENTRY CONDITIONS

h_0 = 364,800 feet

V_{I_0} = 26,031 feet per second (Inertial)

V_0 = 24,480 feet per second (Relative)

γ_0 = -2.0 degrees

σ_0 = 90 degrees

$\phi_0 = \theta_0$ = 0 degrees

(W/S) = 70 #/ft^2

All of the trajectories were terminated at 50,000 feet altitude.

To investigate the impact of aerodynamic heating constraints on
reentry vehicle maneuverability, it was desired to generate a footprint
with temperature constraints to compare to the unconstrained footprint.
Shown in Figure 21 is the unconstrained reentry footprint for the low
lift-to-drag ratio configuration. Except for the maximum down-range
point, all of the points on the footprint were obtained by maximizing
the lateral range at various down-range distances. Although the
radiation equilibrium temperature (RET) was not constrained it was
computed on all of the reentry trajectories. The maximum value of cross-
range (1964 nmi) was attained at approximately 6000 nmi down-range. For
this case the maximum radiation equilibrium temperature was 2670°R.

2. RESULTS

The initial problem investigated, with temperature constraints, was
the maximum cross-range case. 2670°R was considered to be the upper
limit since that value was obtained for the unconstrained case. Figure 22
illustrates the maximum cross-range sensitivity to changes in the maximum
allowable surface temperature. As noted in Figure 22 two cases were run
with temperature constraints of 2550 and 2600°R. The curve shows that
decreasing the temperature from 2670°R to 2550°R results in a 9.4 percent
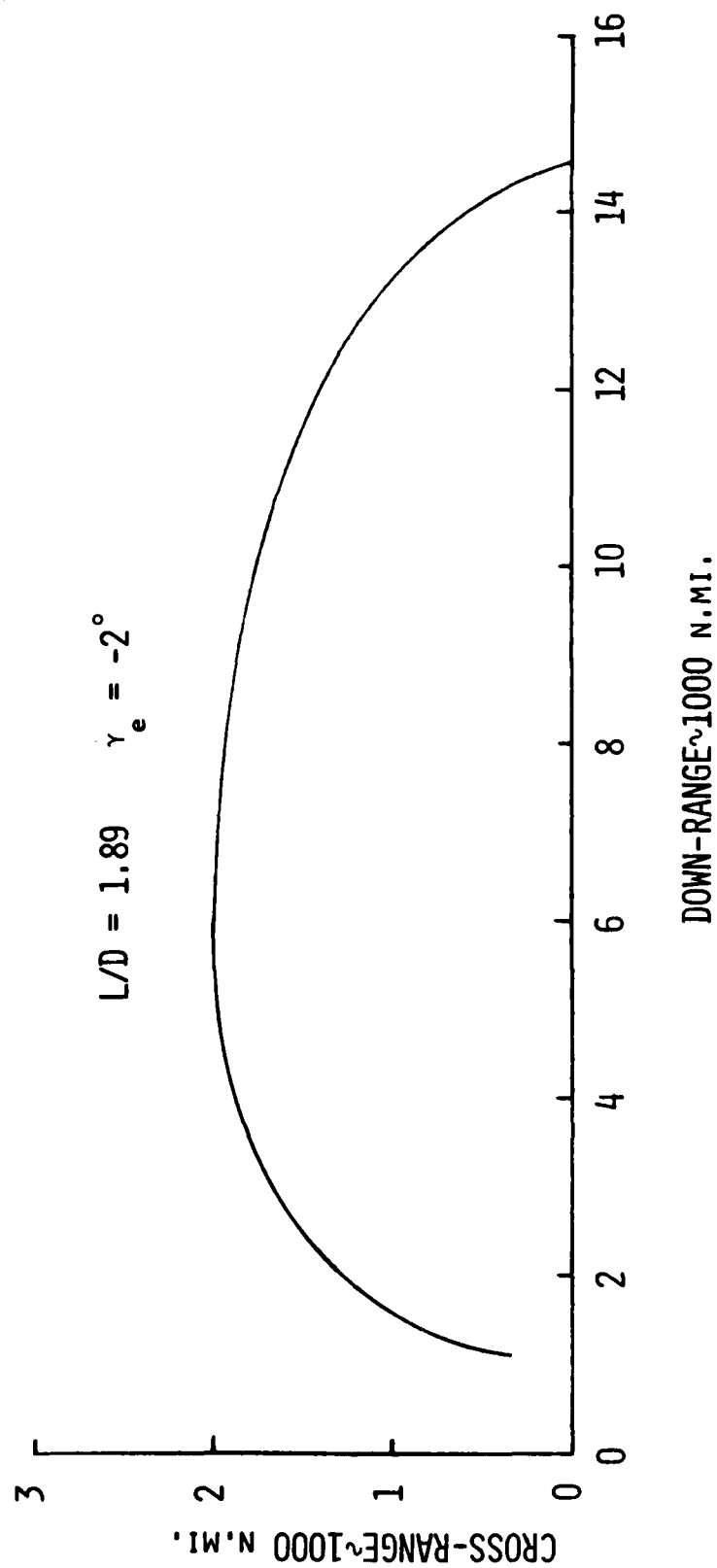
Figure 21. Reentry Footprint (No Temperature Constraints)

$$L/D = 1.89 \qquad \gamma_e = -2^\circ$$
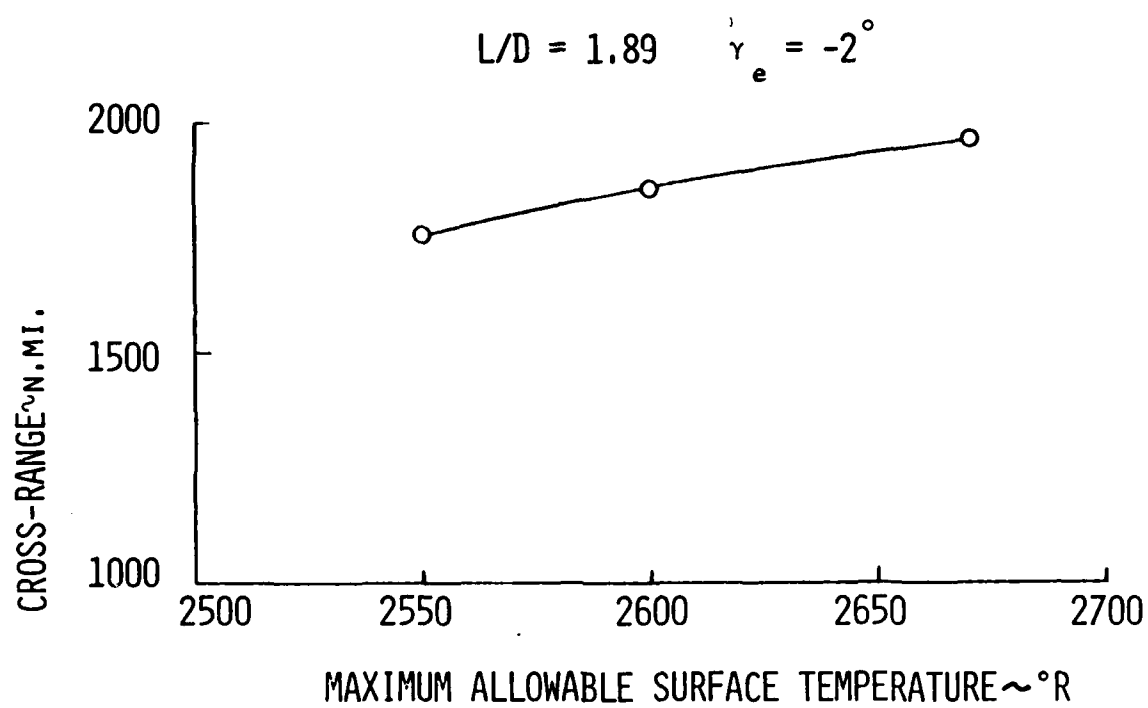
Figure 22. Variation of Cross-range with Maximum Allowable
Surface Temperature

decrease in cross-range. The time histories of the surface temperature, angle-of-attack, and bank angle are shown in Figures 23 through 28 for the three cases. Analysis of the results indicated that, as the temperature constraint used in this analysis becomes more stringent, the vehicle is forced to enter at a lift-to-drag ratio considerably less than maximum, approaching (C_L) max for the 2550°R constraint case. Also, the shape of the entry flight profile is highly influenced by the temperature constraint in that the initial pull-out altitude occurred approximately on the constraint boundary. To show the impact of temperature constraints on the complete footprint, the most stringent temperature limit, namely 2550°R was used in conjunction with down-range constraints to generate the reduced entry footprint shown in Figure 29. Inspection of these entry footprints shows the large amount of geographic coverage that is lost as the result of the temperature constraints. The reason for this reduction in maneuverability is that the vehicle reentering the earth's atmosphere, flying a temperature constrained flight profile, is forced to reenter at a higher altitude than the unconstrained case, therefore a lower dynamic pressure and lift/drag ratio.

It is interesting to note that although the maximum cross-range of the footprint was reduced only 184 nmi out of 1964 when the maximum temperature was reduced from the unconstrained condition to 2550°R, significant amounts of down-range were lost. On the forward part of the footprint the maximum down-range was reduced from 14500 to 11700 nmi and on the rear portion of the footprint the minimum range increased from around 1000 to 2000 nmi. The footprint collapses towards the center but not as much as one might expect considering that the limit of 2550°R is about the lowest that can be achieved on the initial plunge from the initial entry conditions outlined in Table 2.

3. SUMMARY AND COMMENTS

In conclusion, the footprint generated by imposing a temperature constraint of 2550°R compared to the unconstrained footprint of Section II loses 9.4% of the maximum cross-range capability, 19% of the maximum down-range, and the minimum down-range is doubled from 1000 to 2000 nmi.
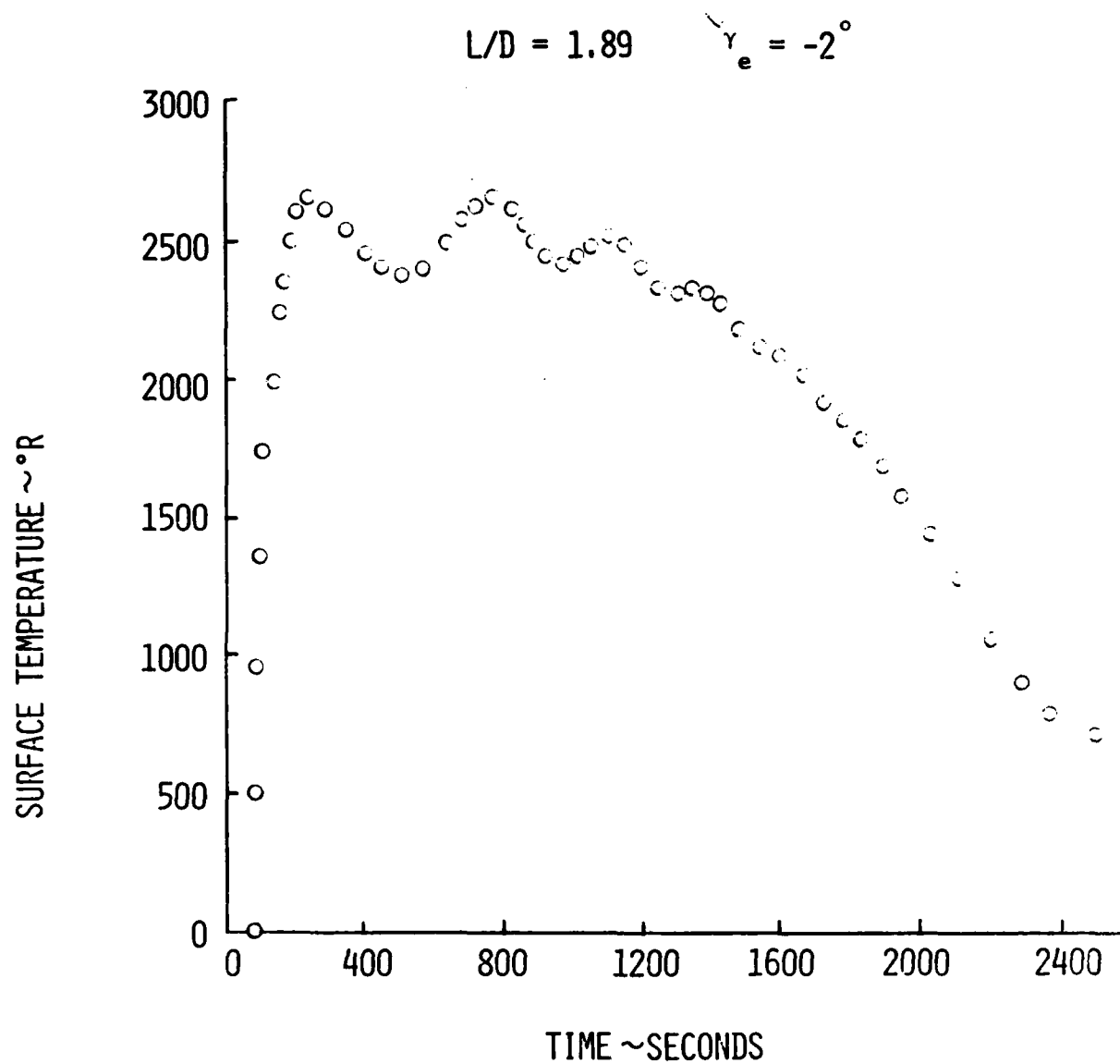
Figure 23.   Unconstrained Case, Surface Temperature History
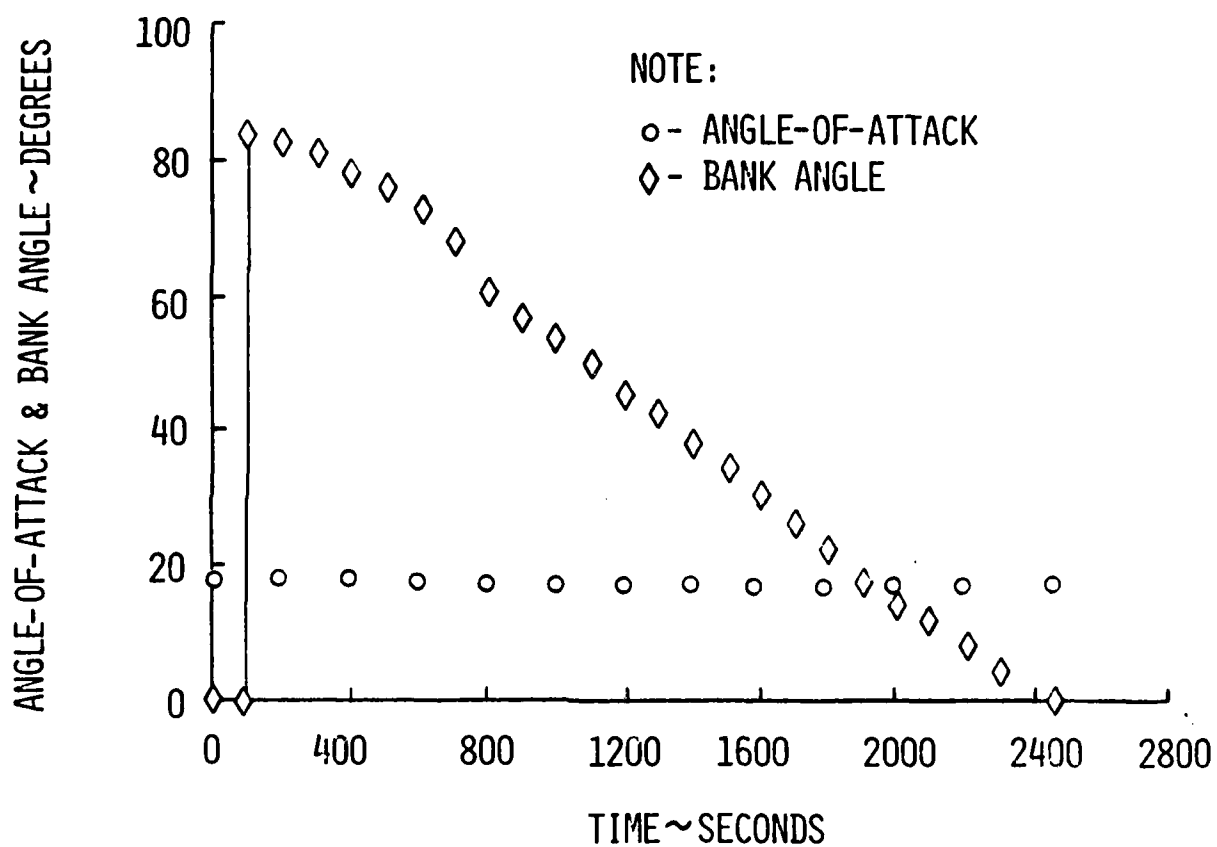
$$L/D = 1.89 \qquad \overset{.}{\gamma}_e = -2°$$

Figure 24.   Unconstrained Case, Angle-of-Attack and Bank History
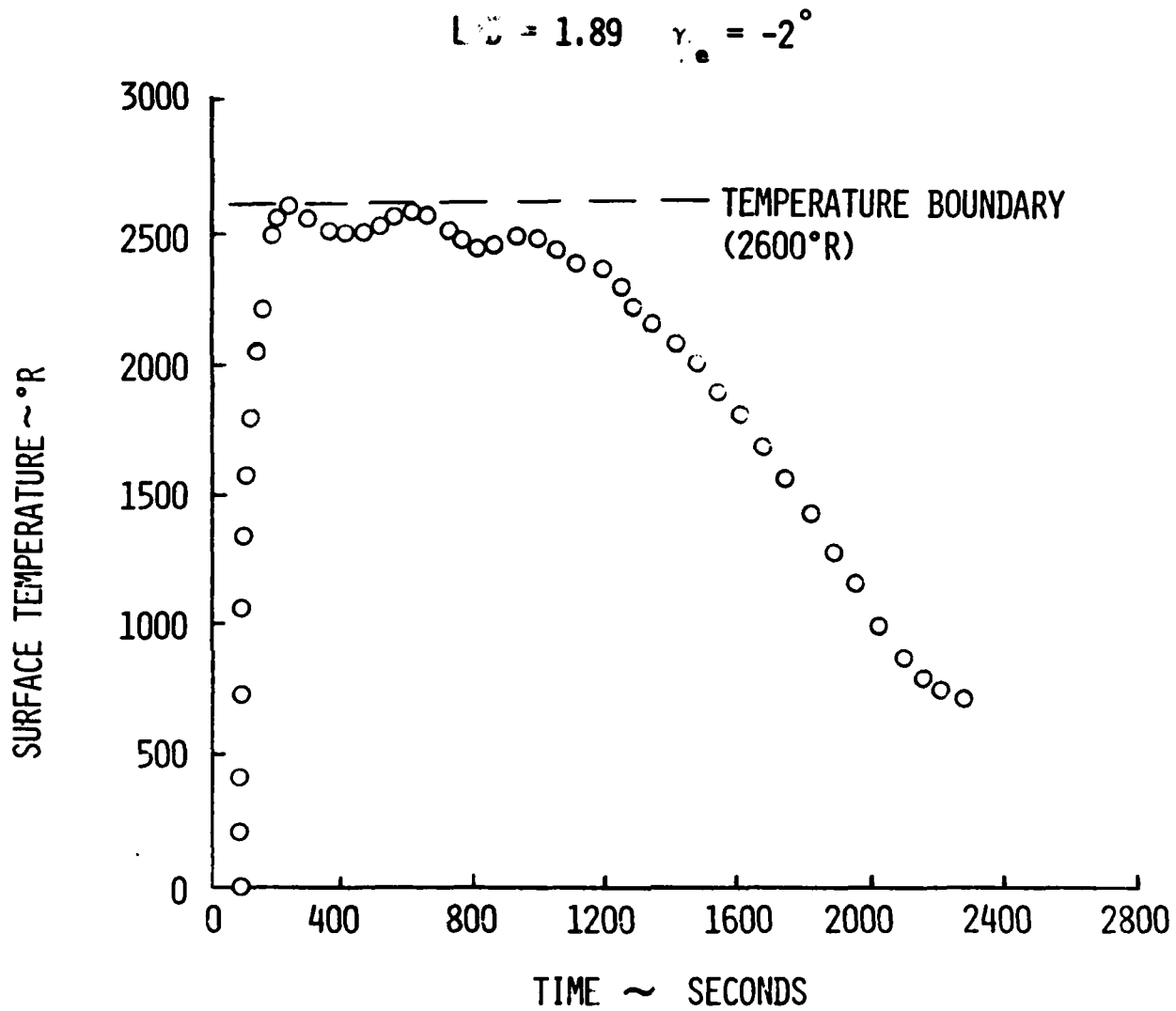
Figure 25.   Allowable Temperature 2600°R, Surface Temperature History

$$L/D = 1.89 \qquad \dot{\gamma}_e = -2^\circ$$

NOTE:

o - ANGLE-OF-ATTACK

◊ - BANK ANGLE

TEMPERATURE CONSTRAINT=2600°R
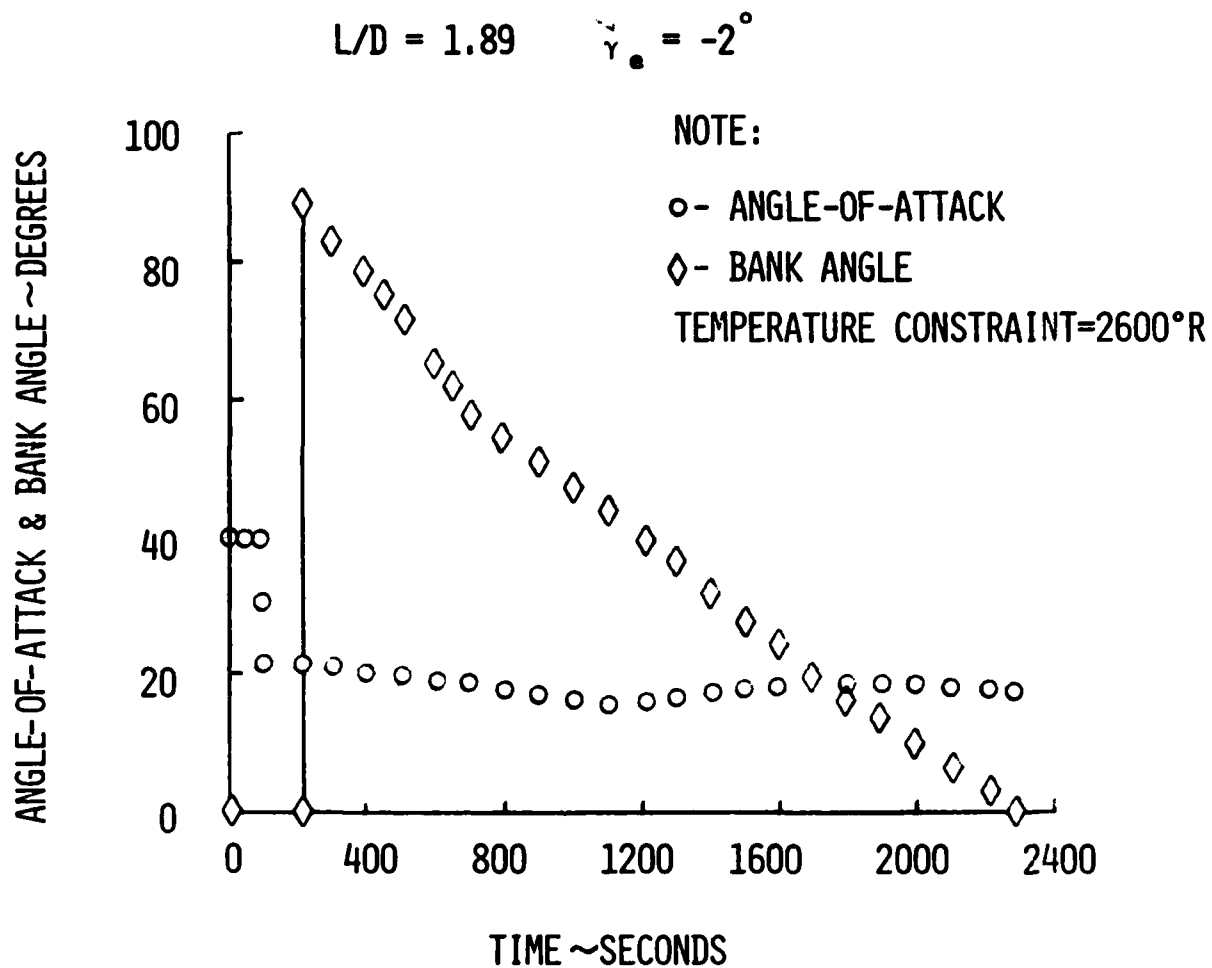
Figure 26. Allowable Temperature 2600°R, Angle-of-Attack and Bank History

$$L/D = 1.89 \qquad \gamma_e = -2°$$
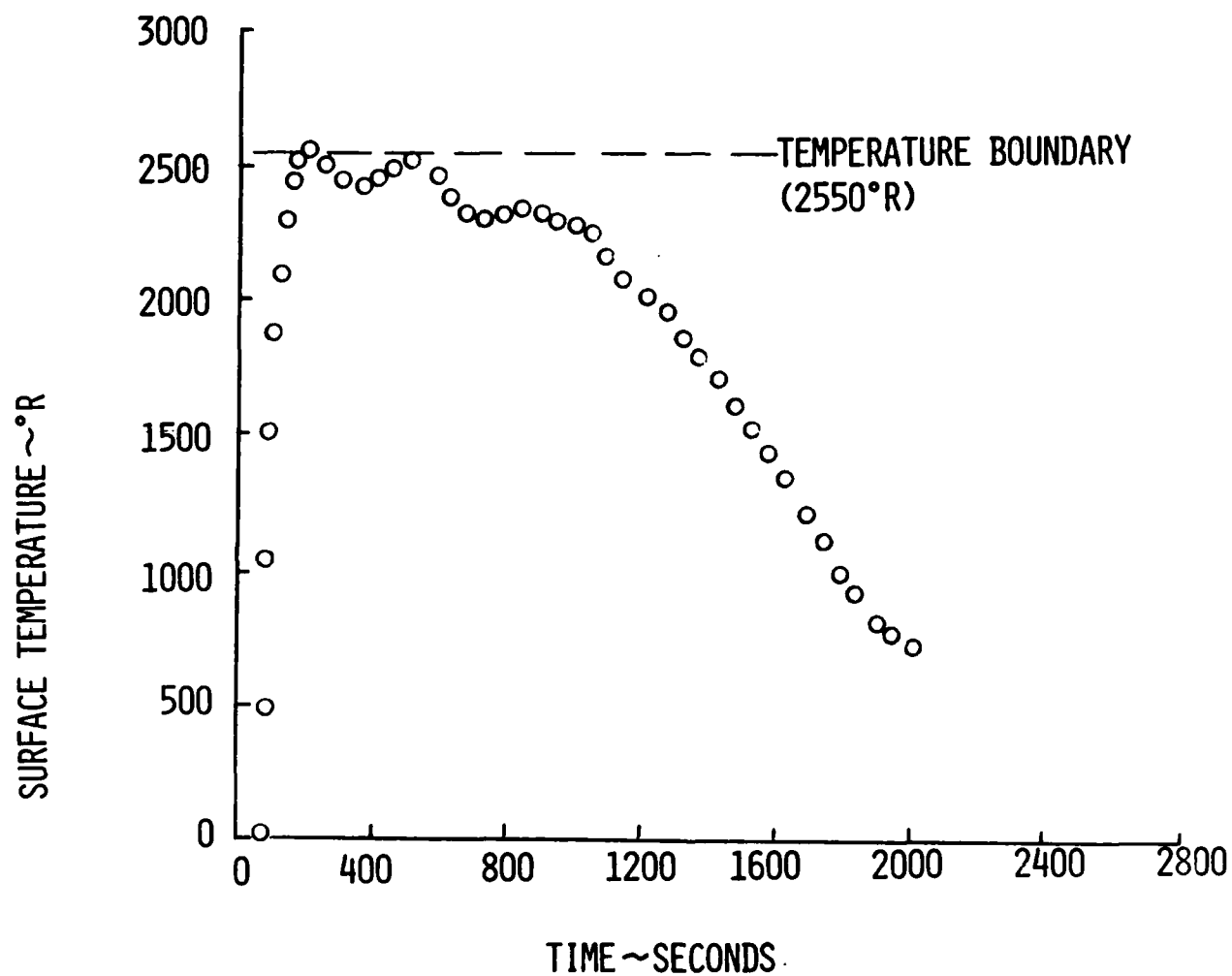
Figure 27. Allowable Temperature 2550°R, Surface Temperature History
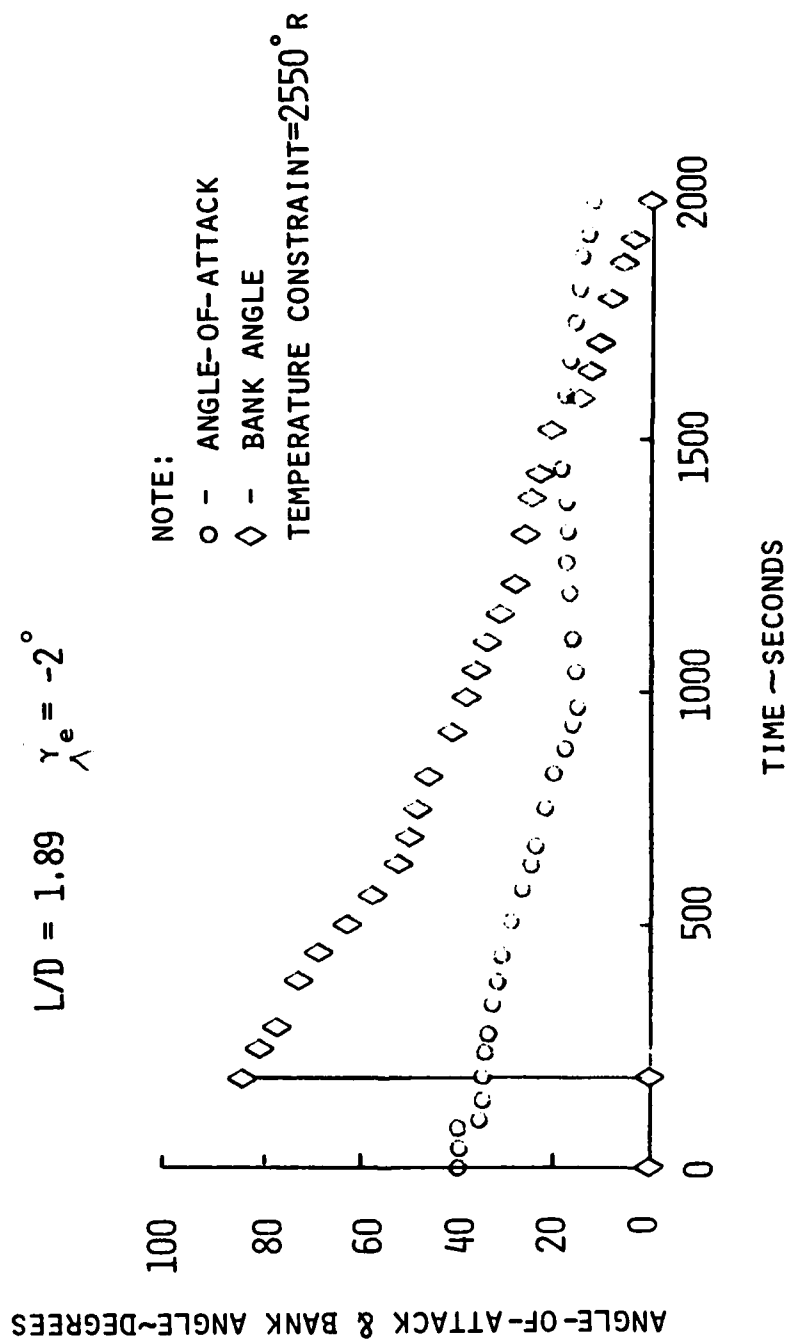
Figure 28. Allowable Temperature 2550°R, Angle-of-Attack and Bank Histories
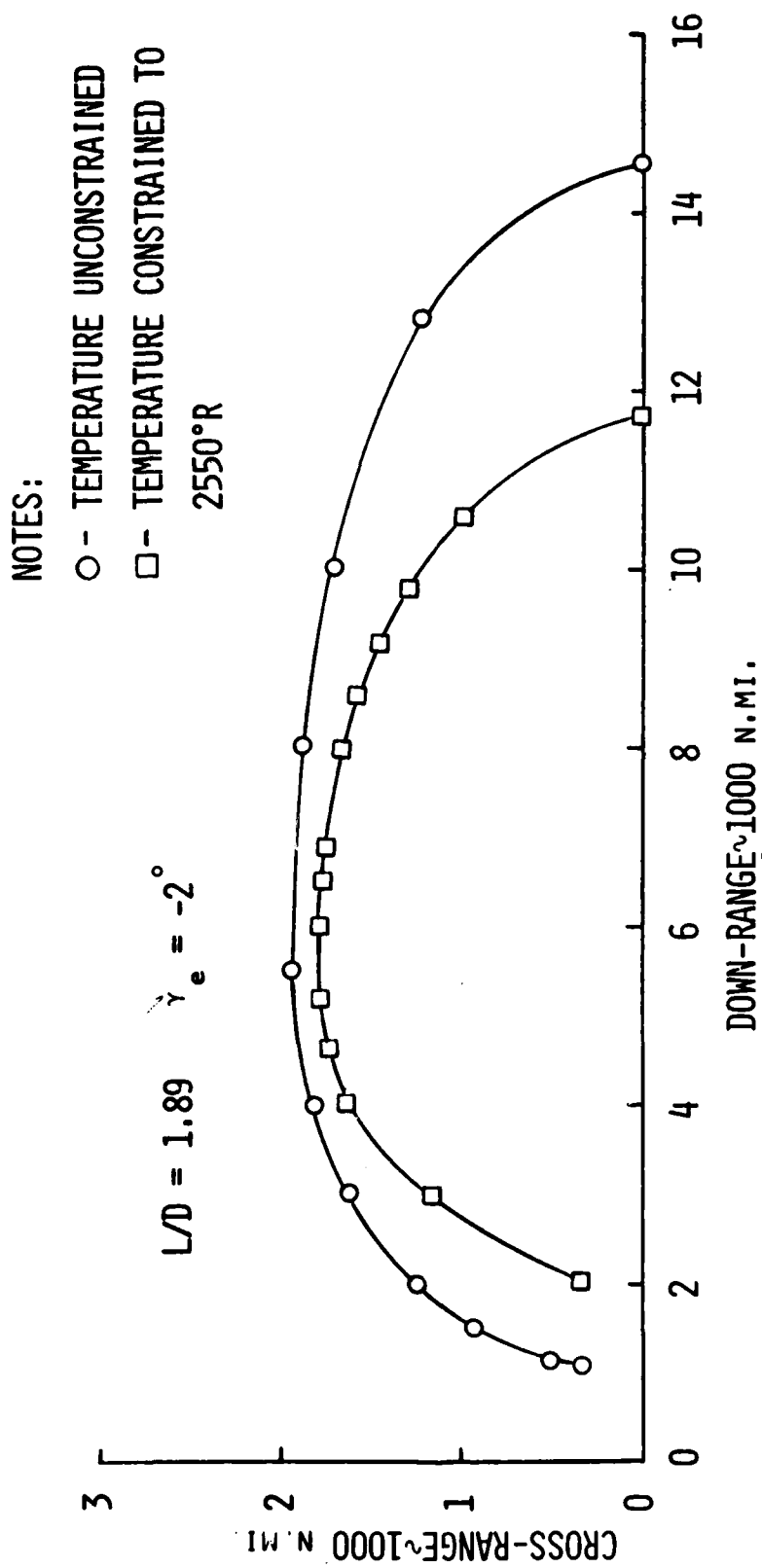
Figure 29. Sensitivity of Temperature Constraint on Reentry Footprint

Due to the substantial amount of computer time involved to run optimal
solutions, constrained footprints were not generated for other initial
conditions. The heating method used in the trajectory model has provision
for simultaneously constraining temperature on more than one point on
the vehicle. However, the lack of data for the heating model on the other
points of the low L/D vehicle or the other vehicles prevented running
them with temperature constraints.

SECTION IV

APPLICATION AND DISPLAY

The work shown to this point has been to develop a procedure for rapid, accurate, footprint calculations under the various flight constraints. However, to determine the utility of a vehicle concept in performing a given function, the footprint data must be related and applied to that function. For such concepts as an orbital based maneuvering entry vehicle, questions of interest might include the following: (1) What is the landing coverage from a specified deorbit point? (2) What are the effects of node rotations and inclination change? (3) What portions of which orbits allow landing in a set of designated landing sites? A similar set of questions could be phrased for a boost glide missile system. The procedure developed for the display and analysis portion of the footprint generator was designed as a tool to find answers to those questions.

Options are provided to display the footprint on two types of world maps and calculate a modified footprint to allow the user to change the node location, orbital inclination, or increase down-range for stepping the deorbit point around an orbit. An option is also provided to allow input of only half of a symmetrical footprint and computer generate the other half. Required inputs to the procedure are longitude, latitude, and heading angle of a reference point on the initial orbit and the longitude, latitude points of the previously calculated footprint. If a modified footprint is to be calculated, the procedures shown below on "calculating a new footprint" are used first, if display only of the generated footprint is desired this section is skipped.

1. CALCULATING A NEW FOOTPRINT

The first step is to take the longitude-latitude points from the footprint boundary calculated by the footprint generator and convert this data into cross-range and down-range from a reference such as the deorbit condition (longitude, latitude of the deorbit point plus the heading angle of the orbit at that point to define the initial great circle for down-range calculation).

48
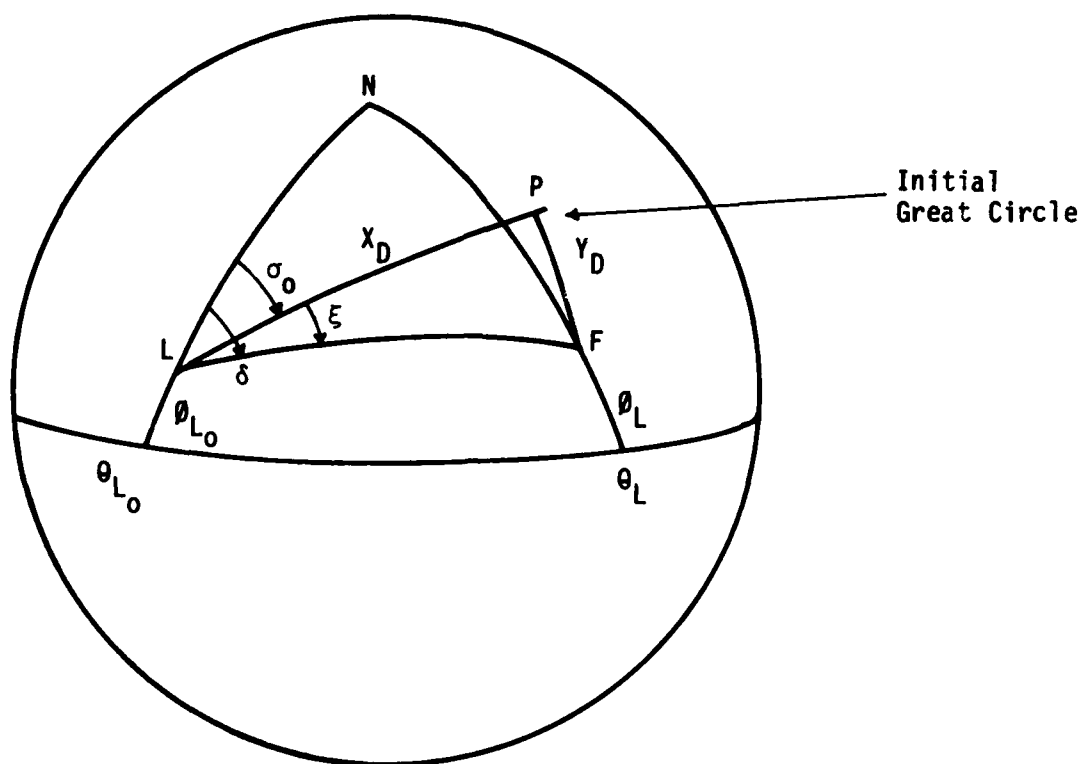
Figure 30. Down-range - Cross-range Geometry

The geometry of the problem is shown in Figure 30 where point L is the initial point, arc LP is the initial great circle, and point F is a point on the footprint boundary. The cross-range of point F is defined as the perpendicular distance from the point to the initial great circle, shown in the figure as the arc PF. The down-range is then the distance along the initial great circle from the initial point to the point at which the cross-range is measured (arc LP).

From spherical trigonometry, the great circle range LP to the point F is computed

$$LF = \cos^{-1}[\sin \phi_L \sin \phi_{L0} + \cos \phi_L \cos \phi_{L0} \cos (\theta_L - \theta_{Lc})] \qquad (8)$$

The heading ζ of the great circle from the initial point to the point F is computed from the spherical triangle LNF:

$$\tan \zeta = \frac{\sin (\theta_L - \theta_{L0}) \cos \phi_L \cos \phi_{L0}}{\sin \phi_L - \sin \phi_{L0} \cos (LF)} \tag{9}$$

and the triangle LPF is solved for the down-range X_D, and cross-range Y_D:

$$X_D = R' \cos^{-1} [\cos (LF)/\cos(\sin^{-1} (\sin(LF) \sin \xi))] \tag{10}$$

$$Y_D = R' \sin^{-1} [\sin (LF) \sin \xi] \tag{11}$$

where: $\xi = \zeta - \sigma_0$

and R' is the average radius of the earth

The next step is to modify, through input, the node location (by changing θ_{L0} of the initial point), the inclination angle of the initial orbit (by changing σ_0), or the down-range (X_D which was just calculated for stepping around the orbit). These parameters may be changed singly or in combination.

Next, this revised condition is then converted back to a new longitude, latitude point for plotting and analysis. However, what was a straightforward calculation going to cross-range and down-range now requires an interation converting back to longitude and latitude. Starting from the new down-range (X_{DM}) and heading at the initial point (σ_{OM}) holding the cross-range (arc PF) constant and rearranging Equations 3 and 4:

$$LF_M = \cos^{-1} [\cos (PF) \cos (X_{DM}/R')] \tag{12}$$

where LF_M is the new value of arc LF

$$\xi_M = \sin^{-1} [\sin (PF)/\sin (LF_M)] \tag{13}$$

and $\zeta_M = \xi_M + \sigma_{OM}$ $\qquad$ (14)

where LF_M, ξ_M, and ζ_M are the new values of LF, ξ and ζ.

Now a guess at a new latitude of the footprint point is made (ϕ_{LM}), and ($\theta_L - \theta_{LO}$)$_M$ is computed from Equation 8. Putting this in Equation 9 yields a ζ which is compared with the result obtained from Equation 14. If the values of ζ and ζ_M are not equal, a new ϕ_{LM} is chosen and the process repeated until it converges.

The new longitude is then computed by:

$$\theta_{LM} = (\theta_L - \theta_{LO})_M + \theta_{LOM} \tag{15}$$

where the subscript M denotes the new value of the variables. This procedure is repeated until all points of the footprint have been processed. At this point the new footprint is available for plotting.

2. PLOTTING A FOOTPRINT

Display of the footprint is accomplished by plotting the longitude and latitude points on a map from the world mapping capability available through the DISSPLA integrated software system and plotting language (Reference 12). From the 15 map projections available in this system two were chosen to display the results, the cylindrical equidistant and the orthographic projection. All or any portion of the world can be projected. The cylindrical equidistant shows the coordinates as they are on a flat map and in the orthographic projection one views the globe from far away-projection pole at infinity.

The plotting program is structured to make both these maps for each condition desired to be plotted. As only half the earth is visible on the orthographic projection, the viewing angle is varied so that all the footprint (or most for large footprints) can be seen unless the user instructs otherwise. Some sample results as presented in the following paragraphs were copied from a Tektronix terminal.

Figure 31 shows the footprint for the L/D = 1.89 vehicle when operated at a high angle-of-attack to reduce heating loads. The footprint was run with the starting point taken as the entry conditions of Table 2 and

51

(d) Orthographic - Heading 90°, longitude 0°, latitude 0°

(e) Orthographic - Heading 30°, longitude 0°, latitude 0°

(a) Heading 90°, longitude 0°, latitude 0°

(b) Heading 30°, longitude 0°, latitude 0°
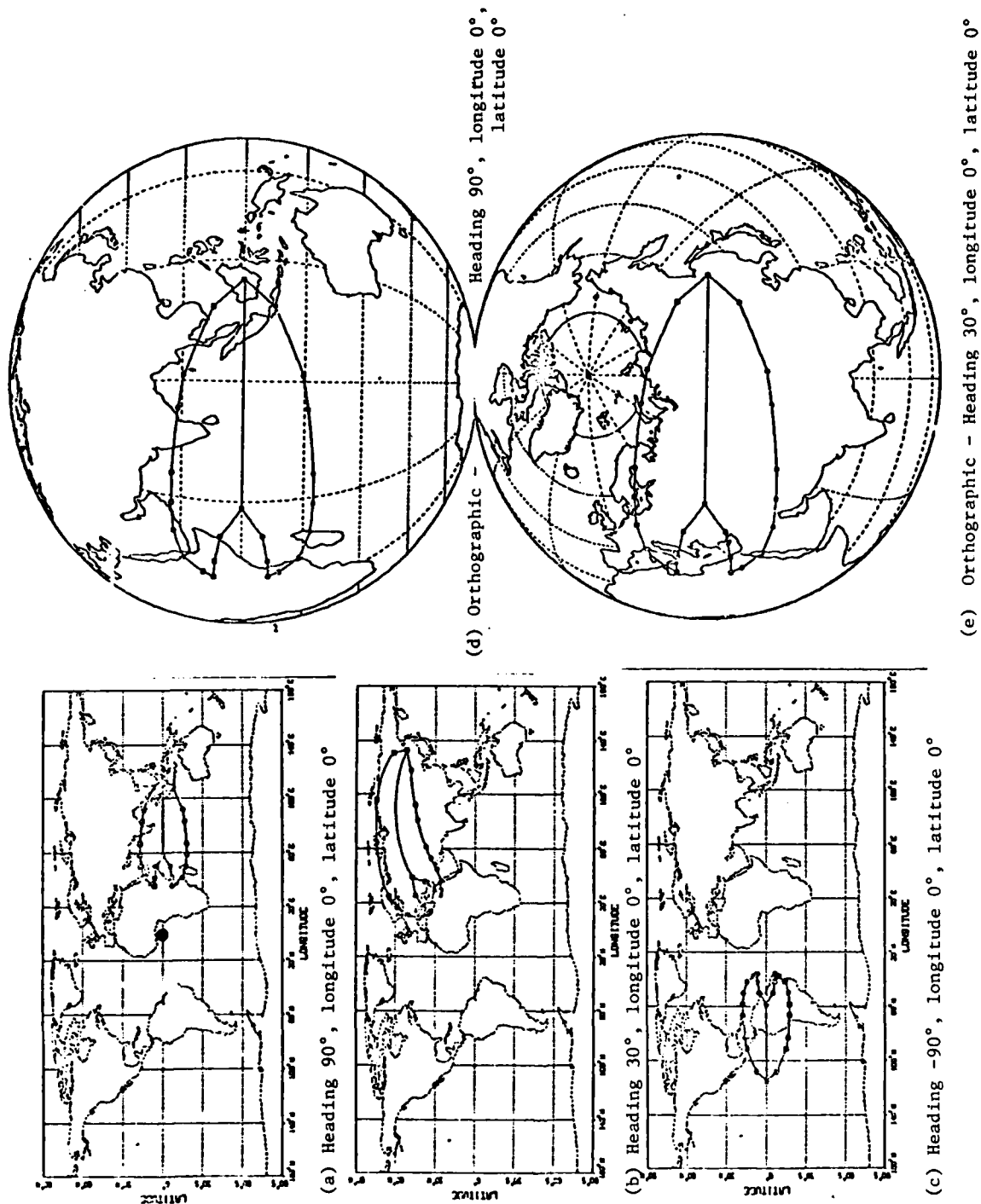
(c) Heading -90°, longitude 0°, latitude 0°

Figure 31. Sample Plots L/D = 1.89 Reduced Footprint

heading due east at 0° latitude and longitude. Note the starting point
did not lie on the footprint. The positive latitude half of the footprint
was input and the other half was calculated by symmetry in the display
program. The left side of the figure shows plotting on the cylindrical
equidistant projection. At the top in Figure 31 (a) is the footprint
"as run" at a heading angle of 90° (inclination 0°), the starting point at
0° latitude and longitude is shown by the filled circle. In Figure 31 (b)
the initial heading has been changed to 30° (inclination 60°), and at
the bottom in Figure 31(c) a heading of -90° is shown. The right side
of the figure shows inclination 0° in Figure 31 (d) and inclination 60°
in Figure 31(e) on the orthographic projection.

Figure 32 shows similar plots for the larger footprint, this for the
L/D = 2.6 vehicle. The starting point was again the conditions from
Table 2 and heading east at 0° longitude and latitude. The left side of
the figure on the cylindrical equidistant projection shows inclination
of 0° in Figure 32 (a) and 30° in 32 (b). Note, that the points are not
connected when the lines would cross longitude 180°. The right side
shows the same plots on the orthographic projection. The area of the
footprint is so large it won't fit on half the globe so only a portion
can be shown on the orthographic projection. The area of the map not
covered by the footprint is shaded for ease of viewing. Figure 32(c)
shows the inclination 0° and 32(d) inclination 30°.

3. EARTH ROTATIONAL EFFECTS

An approximation to earth rotational effects has been included as an
option in the computer model. To correctly include rotation it would be
necessary to re-run trajectories for each case being considered. However,
if it is assumed that the basic trajectory is unchanged by a rotating
earth and the predominate effect is that of the earth rotating below the
trajectory a first order approximation of the shift due to the rotation
can be obtained. This is a shift in the longitude of the end point, with
the latitude unchanged, and is computed by $\theta_{LROT} = \theta_{LNROT} - \omega_p t$; where
θ_{LROT} is the new longitude of the end point in degrees, θ_{LNROT} is the

FOOTPRINT GENERATOR
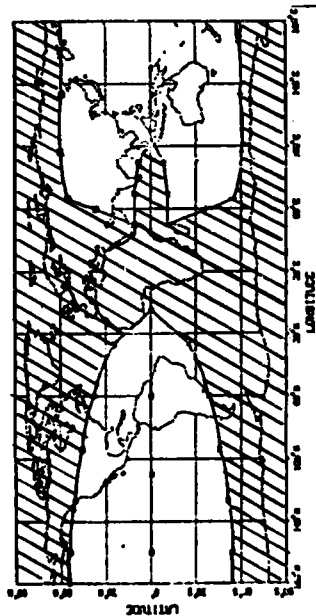
(a) Heading 90°, longitude 0°, latitude 0°
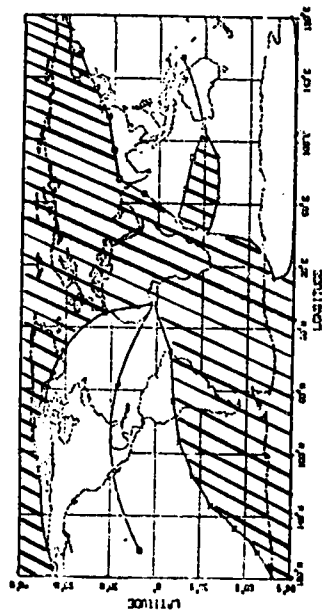
(b) Heading 60°, longitude 0°, latitude 0°

(c) Orthographic – Heading 90°, longitude 0°, latitude 0°
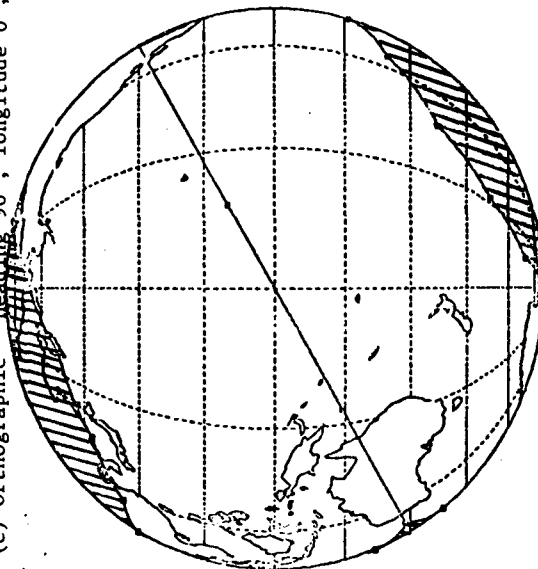
(d) Orthographic – Heading 60°, longitude 0°, latitude 0°

Figure 32.   Sample Plots L/D = 2.6 Footprint

54

longitude of the nonrotating and point ω_p is earth angular rotation
rate = .004178 deg/sec, and t is the flight time of the trajectory. The
flight time (t) is obtained from the nonrotating trajectory runs which
developed the footprint.

Typical flight times range from 2000 to 4000 seconds and are generally
shorter on the back portion of the footprint than they are on the
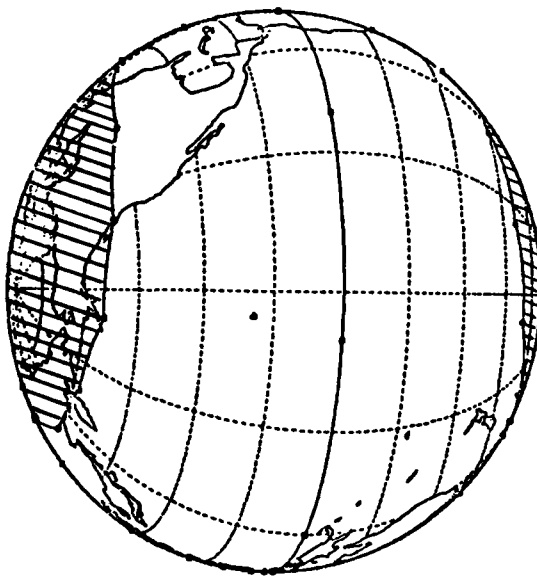forward portion. This then produces a longitude shift of 8.4 to 16.7
degrees. Note that the longitude shift is toward the west, that is toward
more negative values. This has the effect of stretching the footprint
when the initial conditions are heading west on the equator, compacting
it when heading east, and distorting it at other inclinations as shown
in Figure 33. The starting point in Figure 33 taken as the entry
conditions of Table 2, was at 0° longitude, 0° latitude and is out of
view in the diagram. This point corresponds to the time = 0 condition
and would not be moved by earth rotation.

nonrotating footprint

rotating footprint

shift due to rotation
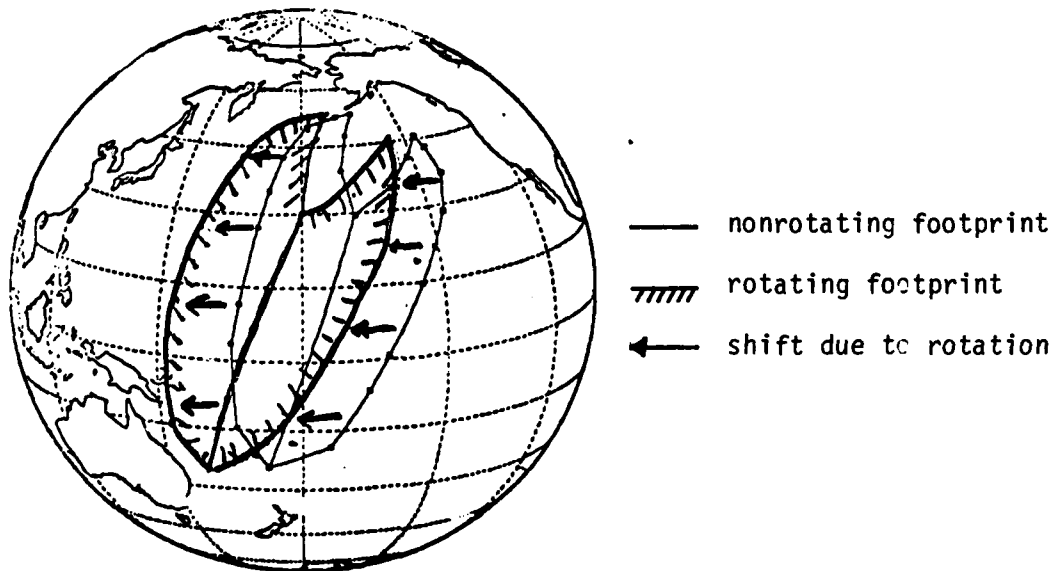
Figure 33. Shift Due to Earth Rotation

4. OTHER PLOTTING CONSIDERATIONS

This system as described represents an attempt to automate a procedure for display and manipulation of footprints requiring little user knowledge of the DISSPLA system and a minimum of input data. Many other different things may be done to tailor a program to produce the most useful plots for a particular application. Among these would be: other types of projections, mapping of only a portion of the earth, labeling and titling plots, shading of footprints, insertion of vehicle pictures, display of more than one footprint on the same map, or structuring of the analysis program to generate and plot mission oriented features. Many of these can be done with very little effort.

The footprint generator developed in this report shows potential as a powerful tool for rapid calculation of entry vehicle maneuvering capability. The application and display work developed here provides a first step towards rapidly analyzing vehicle application to a required mission and producing high quality plots.

SECTION V

CONCLUSIONS

1. Parameter optimization methods were applied to maximize lateral range with and without downrange constraints to produce performance footprints. Good convergence was obtained from using the methods "creeper" and "pattern" on the bank angle control schedule, angle-of-attack was set to L/D max.

2. A simplified bank control procedure was developed which closely approximated the optimal footprint results where no heating constraints were imposed. The procedure is outlined in Section II. The method is easy to use and is efficient requiring less computer resources than the optimization procedure by a factor of about 25 to 1.

3. No simple method was found to handle heating constraints. However, the parameter optimization procedure was able to produce solutions for the single heating point considered. Footprint shrinkage when applying the temperature constraint was most noticeable at the front and back portions with less shrinkage in maximum cross-range. For the most stringent temperature constraint considered the results were a 19% loss in maximum down-range, a doubling of the minimum down-range and a 9.4% loss in maximum cross-range.

4. An automated procedure was developed to display and move the footprint on world maps. This technique shows promise in relating results to functional performance and can be used separately or in conjunction with the footprint data.

APPENDIX A

COORDINATE SYSTEM TRANSFORMATIONS

This appendix develops the transformations necessary to relate the coordinate systems employed.
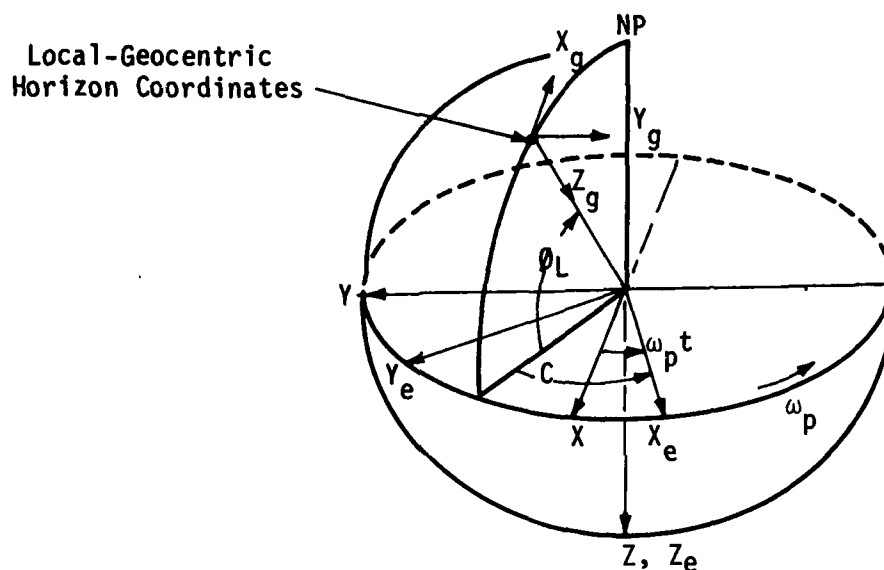
X, Y, Z Inertial Coordinates

X_e, Y_e, Z_e Earth-referenced coordinates

X_g, Y_g, Z_g Local-geocentric-horizon coordinates

To describe body motion relative to the planet, a local-geocentric-horizon coordinate system was employed. To locate the X_g, Y_g, Z_g axes with respect to the X_e, Y_e, Z_e axes, rotation was first about Z_e by an angle (180° + C) and then about Y_g through the angle (90° - ϕ_L) where ϕ_L is vehicle latitude and the angle C is related to the vehicle position by the expression:

$$C = \tan^{-1} (Y_e/X_e) \tag{A1}$$

The complete transformation reduced to a single matrix is given by:

$$
\begin{vmatrix} \dot{X}_g \\ \dot{Y}_g \\ \dot{Z}_g \end{vmatrix} =
\begin{vmatrix}
-\sin(\phi_L)\cos(c) & -\sin(\phi_L)\sin(c) & -\cos(\phi_L) \\
\sin(c) & -\cos(c) & 0 \\
-\cos(\phi_L)\cos(c) & -\cos(\phi_L)\sin(c) & \sin(\phi_L)
\end{vmatrix}
\begin{vmatrix} \dot{X}_e \\ \dot{Y}_e \\ \dot{Z}_e \end{vmatrix}
\quad (A2)
$$

or

$$
\begin{vmatrix} \dot{X}_g \\ \dot{Y}_g \\ \dot{Z}_g \end{vmatrix} =
\begin{vmatrix}
i_1 & j_1 & k_1 \\
i_2 & j_2 & k_3 \\
i_3 & j_3 & k_3
\end{vmatrix}
\begin{vmatrix} \dot{X}_e \\ \dot{Y}_e \\ \dot{Z}_e \end{vmatrix}
\quad (A3)
$$

Aerodynamic forces are conveniently summed in a wind axis coordinate system (X_A, Y_A, Z_A). Since the equations of motion are solved in (X_e, Y_e, Z_e) coordinates the wind axis components of force must then be resolved into this basic system. The transformation from local-geocentric-horizon coordinates to wind axes is given by:

$$
\begin{vmatrix} X_A \\ Y_A \\ Z_A \end{vmatrix} =
\begin{vmatrix}
\cos(\gamma_A)\cos(\sigma_A) & \cos(\gamma_A)\sin(\sigma_A) & -\sin(\gamma_A) \\
\begin{array}{l} -\sin(\sigma_A)\cos(\phi_B) \\ +\sin(\gamma_A)\cos(\sigma_A)\sin(\phi_B) \end{array} & \begin{array}{l} \cos(\sigma_A)\cos(\phi_B) \\ +\sin(\alpha_A)\sin(\alpha_A)\sin(\phi_B) \end{array} & \cos(\gamma_A)\sin(\phi_B) \\
\begin{array}{l} \sin(\sigma_A)\sin(\phi_B) \\ +\sin(\gamma_A)\cos(\sigma_A)\cos(\phi_B) \end{array} & \begin{array}{l} -\cos(\sigma_A)\sin(\phi_B) \\ +\sin(\gamma_A)\sin(\sigma_A)\cos(\phi_B) \end{array} & \cos(\sigma_A)\cos(\phi_B)
\end{vmatrix}
\begin{vmatrix} X_g \\ Y_g \\ Z_g \end{vmatrix}
\quad (A4)
$$

which defines a direction cosine set

$$
\begin{vmatrix} X_A \\ Y_A \\ Z_A \end{vmatrix} =
\begin{vmatrix}
r_1 & s_1 & t_1 \\
r_2 & s_2 & t_2 \\
r_3 & s_3 & t_3
\end{vmatrix}
\begin{vmatrix} X_g \\ Y_g \\ Z_g \end{vmatrix}
\quad (A5)
$$

the resolution from wind axes to local-geocentric then become

$$
\begin{vmatrix} F_{x_g} \\ F_{y_g} \\ F_{z_g} \end{vmatrix} =
\begin{vmatrix}
r_1 & r_2 & r_3 \\
s_1 & s_2 & s_3 \\
t_1 & t_2 & t_3
\end{vmatrix}
\begin{vmatrix} F_{x_A} \\ F_{y_A} \\ F_{z_A} \end{vmatrix}
\quad (A6)
$$

The local-geocentric components are then resolved into the X_e, Y_e, Z_e system through a transposition of the i,j,k matrix, as follows:

$$
\begin{vmatrix} F_{x_e} \\ F_{y_e} \\ F_{z_e} \end{vmatrix} = \begin{vmatrix} i_1 & i_2 & i_3 \\ j_1 & j_2 & j_3 \\ k_1 & k_2 & k_3 \end{vmatrix} \begin{vmatrix} F_{x_g} \\ F_{y_g} \\ F_{z_g} \end{vmatrix} \tag{A7}
$$

The forces acting on the vehicle are the sum of the aerodynamic and gravity forces.

$$
\Sigma F_x = D + mg_x
$$

$$
\Sigma F_y = Y = 0 \tag{A8}
$$

$$
\Sigma F_z = L + mg_z
$$

The side force, Y, is zero since only coordinated turns with zero side slip were considered. The drag and lift terms are:

$$
D = C_D \, q \, S
$$
$$
L = C_L \, q \, S \tag{A9}
$$

Where the dynamic pressure, q, is a function of velocity and altitude and the lift and drag coefficients are functions of Mach, angle-of-attack, and altitude. Thrust was not used in this analysis.

The gravity equations used are as follows:

$$
g_{z_g} = \frac{\mu}{R^2} \left[1 + J \left(\frac{R_e}{R} \right)^2 P_2 + \frac{4H}{5} \left(\frac{R_e}{R} \right)^3 P_3 + \frac{K}{6} \left(\frac{R_e}{R} \right)^4 P_4 \right] \tag{A10}
$$

$$
g_{x_g} = \frac{\mu}{R^2} \left[-2J \left(\frac{R_e}{R} \right)^2 P_5 + \frac{3H}{5} \left(\frac{R_e}{R} \right)^3 P_6 + \frac{2K}{3} \left(\frac{R_e}{R} \right)^4 P_7 \right]
$$

where

$$P_2 = 1 - 3 \sin^2 \phi_L$$

$$P_3 = 3 \sin \phi_L - 5 \sin^3 \phi_L$$

$$P_4 = 3 - 30 \sin^2 \phi_L + 35 \sin^4 \phi_L$$

$$P_5 = \sin \phi_L \cos \phi_L$$

$$P_6 = \cos \phi_L (1 - 5 \sin^2 \phi_L)$$

$$P_7 = \sin \phi_L \cos \phi_L (-3 + 7 \sin^2 \phi_L)$$

The constants used for the planet earth are as follows:

$$\mu = 1.407698 \times 10^{16} \text{ ft}^3/\text{sec}^2$$

$$R_e = 20,925,631 \text{ ft}$$

$$J = 1623.41 \times 10^{-6}$$

$$H = 6.04 \times 10^{-6}$$

$$K = 6.37 \times 10^{-6}$$

The polar radius used in the oblate earth calculations for latitude and altitude is $R_p = 20,885,965$ ft.

APPENDIX B

AERODYNAMIC CHARACTERISTICS

This appendix presents the aerodynamic coefficient data used for trajectory calculations. Sketches of the configurations are shown in Figure 1a through 1c in the main part of this report and in Figures C-1 through C-3 in Appendix C. 'These data were obtained from References 8, 9, 10, 13, and 14.

Tables B-1 and B-2 present the aerodynamics for the vehicle shown in Figure 1a, Table B-3 for the vehicle of 1b, and Tables B-4 and B-5 for the vehicle of 1c. Tables B-6 and B-7 show the aerodynamics for the vehicle shown in Figure C-1 and Table B-8 for the vehicle of C-3.

The configuration shown in Figure C-2 is the same as the configuration shown in Figure 1c in the main part of this report and its aerodynamics were given in Tables B-4 and B-5.

TABLE B-1

(L/D) = 1.89 CONFIGURATION LIFT COEFFICIENT DATA

Mach \ α(deg)→	7.5	12.5	17.5	20.	25.	30.	35.	40.	
2.	.242	.420	.602	.689	.846	.998	1.	1.	
5.	.097	.214	.351	.424	.570	.720	.846	.961	h = 0. to 100,000 ft
8.	.060	.161	.300	.365	.518	.669	.799	.910	
20.	.056	.153	.290	.356	.509	.645	.784	.884	
2.	.242	.420	.602	.356	.509	.645	.784	.884	
5.	.097	.214	.351	.356	.509	.645	.784	.784	h = 185,000 ft
8.	.060	.161	.300	.356	.509	.645	.784	.884	
20.	.056	.153	.290	.356	.509	.645	.784	.884	
2.	.242	.420	.602	.354	.506	.641	.779	.879	
5.	.097	.214	.351	.354	.506	.641	.779	.879	h = 220,000 ft
8.	.060	.161	.300	.354	.506	.641	.779	.879	
20.	.056	.153	.290	.354	.506	.641	.779	.879	
2.	.242	.420	.602	.349	.500	.633	.771	.869	
5.	.097	.214	.351	.349	.501	.633	.771	.869	h = 250,000 ft
8.	.060	.161	.300	.349	.501	.633	.771	.869	
20.	.056	.153	.290	.349	.501	.633	.771	.869	
2.	.242	.420	.602	.323	.465	.588	.719	.811	
5.	.097	.214	.351	.322	.465	.588	.719	.811	h = 300,000 ft
8.	.060	.161	.300	.323	.465	.588	.719	.811	
20.	.065	.153	.290	.323	.465	.588	.719	.811	

TABLE B-2

(L/D) = 1.89 CONFIGURATION DRAG COEFFICIENT DATA

Mach \ α (deg) →	7.5	12.5	17.5	20.	25.	30.	35.	40.	
2.	.156	.210	.301	.359	.498	.675	1.0	1.0	
5.	.086	.118	.181	.225	.339	.492	.673	.891	h = 0. to 100,000 ft
8.	.074	.098	.157	.196	.309	.458	.636	.844	
20.	.074	.095	.153	.192	.304	.443	.624	.821	
2.	.156	.210	.301	.192	.304	.443	.624	.821	
5.	.086	.118	.181	.192	.304	.443	.624	.821	h = 185,000 ft
8.	.074	.098	.157	.192	.304	.443	.624	.821	
20.	.074	.095	.153	.192	.304	.443	.624	.821	
2.	.156	.210	.301	.198	.310	.450	.630	.827	
5.	.086	.118	.181	.198	.310	.450	.630	.827	h = 220,000 ft
8.	.074	.098	.157	.198	.310	.450	.630	.827	
20.	.074	.095	.153	.198	.310	.450	.630	.827	
2.	.156	.210	.301	.210	.323	.463	.643	.839	
5.	.086	.118	.181	.210	.323	.463	.643	.839	h = 250,000 ft
8.	.074	.098	.157	.210	.323	.463	.642	.839	
20.	.074	.095	.153	.210	.323	.463	.642	.839	
2.	.156	.210	.301	.283	.398	.542	.717	.908	
5.	.086	.118	.181	.283	.398	.542	.717	.909	h = 300,000 ft
8.	.074	.098	.157	.283	.398	.542	.717	.909	
20.	.074	.095	.153	.283	.398	.542	.717	.909	

TABLE B-3

$(L/D) = 2.2$ CONFIGURATION LIFT AND DRAG COEFFICIENT DATA

Mach \ α (deg)→	0.	4.	8.	12.	16.	20.	40.
	(Drag Coefficient C_D)						
0.2	.0417	.0421	.0433	.0701	.1134	.1757	.300
1.2	.085	.086	.090	.114	.159	.247	.590
5.	.040	.045	.050	.0655	.0972	.146	.723
10.	.029	.025	.034	.0584	.089	.134	.622
20.	.032	.030	.035	.061	.0924	.136	.613
	(Lift Coefficient C_L)						
0.2	-.075	.040	.159	.291	.448	.580	1.00
1.2	-.030	.078	.185	.297	.387	.530	1.00
5.	-.025	.034	.095	.167	.244	.326	.745
10.	-.028	.028	.033	.143	.209	.288	.697
20.	-.026	.017	.054	.134	.201	.276	.680

TABLE B-4

(L/D) = 2.6 CONFIGURATION
NORMAL FORCE COEFFICIENT

Mach\α (deg)→	0.	4.	8.	12.	16.	20.
1.1	-.02	.039	.100	.226	.350	.485
1.89	-.02	.039	.113	.204	.310	.420
3.0	-.04	.016	.113	.175	.274	.380
6.0	-.04	.01	.085	.137	.214	.295
8.0	-.045	.003	.065	.140	.219	.300
10.	-.045	.003	.065	.140	.219	.300

TABLE B-5

(L/D) = 2.6 CONFIGURATION AXIAL FORCE COEFFICIENT

Alt (K ft) \ α (deg) →	0.	4.	8.	12.	16.	20.	
0.	.0778	.0755	.0730	.0700	.0665	.0628	
40.	.0788	.0765	.0740	.0710	.0675	.0638	
80.	.0810	.0787	.0762	.0732	.0697	.0660	Mach = 1.1
100.	.0822	.0799	.0774	.0744	.0709	.0672	
150.	.0992	.0969	.0944	.0914	.0879	.0842	
200.	.1442	.1419	.1394	.1364	.1329	.1292	
250.	.3242	.3219	.3194	.3164	.3129	.3092	
300.	.7742	.7719	.7694	.7664	.7629	.7592	
0.	.0506	.0435	.0366	.0313	.0275	.0246	
40.	.0512	.0441	.0372	.0319	.0281	.0252	
80.	.0523	.0452	.0383	.0330	.0292	.0263	Mach = 3.0
100.	.0532	.0461	.0392	.0340	.0301	.0272	
150.	.0540	.0469	.0400	.0347	.0309	.0280	
200.	.0601	.0539	.0470	.0417	.0379	.0350	
250.	.0805	.0734	.0665	.0612	.0574	.0545	
300.	.1676	.1605	.1536	.1483	.1445	.1416	

TABLE B-5 (Concluded)
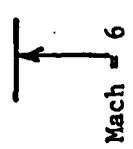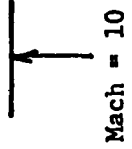
Alt (K ft) \ α (deg) →	0.	4.	8.	12.	16.	20.	
0.	.0230	.0188	.0156	.0140	.0140	.0140	
40.	.0234	.0192	.0160	.0144	.0144	.0144	
80.	.0245	.0203	.0170	.0155	.0155	.0155	
100.	.0250	.0208	.0176	.0160	.0160	.0160	
150.	.0257	.0215	.0182	.0167	.0167	.0167	
200.	.0318	.0275	.0243	.0228	.0228	.0228	Mach = 6
250.	.0467	.0425	.0393	.0377	.0377	.0377	
300.	.1159	.1116	.1084	.1069	.1069	.1069	
0.	.0220	.0178	.0145	.0130	.0130	.0130	
40.	.0223	.0181	.0148	.0133	.0133	.0133	
80.	.0229	.0187	.0154	.0139	.0139	.0139	
100.	.0233	.0191	.0158	.0143	.0143	.0143	
150.	.0239	.0198	.0165	.0149	.0149	.0149	
200.	.0274	.0232	.0199	.0184	.0184	.0184	Mach = 10
250.	.0389	.0347	.0314	.0299	.0299	.0299	
300.	.0932	.0890	.0857	.0842	.0842	.0842	

TABLE B-6

LOW (L/D) CONFIGURATION
NORMAL FORCE COEFFICIENT

Mach \ α(deg) →	0.	5.	10.	15.	20.
1.3	0.	.030	.060	.117	.203
2.0	0.	.032	.075	.168	.285
2.5	0.	.035	.098	.191	.288
3.95	0.	.041	.093	.165	.248
4.63	0.	.042	.090	.158	.225
10.	0.	.032	.076	.136	.214

TABLE B-7

LOW (L/D) CONFIGURATION AXIAL FORCE COEFFICIENT

Mach = 1.3

Alt (K ft) \ (deg)	0.	5.	10.	15.	20.
0.	.03559	.03559	.03484	.03258	.02808
20.	.03664	.03664	.03589	.03363	.02913
40.	.03724	.03724	.03649	.03423	.02973
60.	.03874	.03874	.03799	.03573	.03123
80.	.03934	.03934	.03859	.03633	.03183
100.	.04054	.04054	.03979	.03753	.03303
150.	.04310	.04310	.04335	.04009	.03559
200.	.05754	.05754	.05679	.05453	.05003
250.	.10699	.10699	.10624	.10398	.09948
300.	.28699	.28699	.28624	.28398	.27948

Mach = 2.0

Alt (K ft) \ (deg)	0.	5.	10.	15.	20.
0.	.02778	.02703	.02703	.02628	.02553
20.	.02816	.02741	.02741	.02666	.02591
40.	.02868	.02793	.02793	.02718	.02643
60.	.02943	.02868	.02868	.02793	.02718
80.	.13048	.02973	.02973	.02898	.02923
100.	.03153	.03078	.03078	.03003	.02928
150.	.03348	.03273	.03273	.03198	.03123
200.	.04293	.04218	.04218	.04143	.04068
250.	.09568	.08493	.08493	.08418	.08343
300.	.22218	.22143	.22143	.22068	.21993

Mach = 2.5

Alt (K ft) \ (deg)	0.	5.	10.	15.	20.
0.	.02375	.02375	.02375	.02375	.02375
20.	.02412	.02412	.02412	.02412	.02412
40.	.02465	.02465	.02465	.02465	.02465
60.	.02540	.02540	.02540	.02540	.02540
80.	.32622	.02622	.02622	.02622	.02622
100.	.02735	.02735	.02735	.02735	.02735
150.	.02832	.02832	.02832	.02832	.02832
200.	.03852	.03852	.03852	.03852	.03852
250.	.07452	.07452	.07452	.07452	.07452
300.	.20802	.20802	.20802	.20802	.20802

TABLE B-7 (Concluded)

Mach = 3.95

Alt (K ft) \ α(deg) →	0.	5.	10.	15.	20.
0.	.01864	.02014	.02089	.02314	.02615
20.	.01897	.02047	.02122	.02347	.02648
40.	.01931	.02081	.02156	.02381	.02682
60.	.01787	.02137	.02212	.02437	.02738
80.	.02062	.02212	.02287	.02512	.02813
100.	.02152	.02302	.03377	.02602	.02903
150.	.02220	.02370	.02445	.02670	.02971
200.	.03007	.03157	.03232	.03457	.03758
250.	.05273	.05422	.05497	.05722	.06023
300.	.07147	.07297	.07372	.07597	.07898

Mach = 4.63

Alt (K ft)	0.	5.	10.	15.	20.
0.	.01512	.01662	.01812	.02112	.02488
20.	.01542	.01672	.01842	.02142	.02518
40.	.01580	.01730	.01880	.02180	.02556
60.	.01632	.01782	.01932	.02232	.02608
80.	.01700	.01850	.02000	.02300	.02676
100.	.01812	.01962	.02112	.02412	.02788
150.	.01887	.02037	.02187	.02487	.02863
200.	.02772	.02922	.03072	.03372	.03748
250.	.04722	.04872	.05022	.05322	.05698
300.	.06072	.06222	.06372	.06672	.07048

Mach = 10.

Alt (K ft)	0.	5.	10.	15.	20.
0.	.01065	.01198	.01331	.01596	.01979
20.	.01078	.01211	.01344	.01609	.01942
40.	.01099	.01232	.01365	.01630	.01963
60.	.01131	.01264	.01397	.01662	.01995
80.	.01165	.01298	.01431	.01696	.02029
100.	.01207	.01340	.01473	.01738	.02071
150.	.01282	.01415	.01548	.01813	.02146
200.	.01680	.01813	.01946	.02211	.02544
250.	.03480	.03613	.03746	.04011	.04344
300.	.08430	.08563	.08696	.08961	.09294

TABLE B-8

HIGH (L/D) CONFIGURATION AXIAL AND NORMAL FORCE COEFFICIENT

Mach\Alt (K ft) →	0.	40.	80.	100.	150.	200.	250.	300.
0.9	.01050	.01120	.01270	.01400	.01332	.02087	.04280	.13394
1.0	.01220	.01295	.01460	.01550	.01332	.02087	.04280	.13394
1.5	.01060	.01130	.01250	.01350	.01332	.02087	.04280	.13394
2.0	.00960	.01000	.01120	.01200	.01332	.02087	.04280	.13394
3.0	.00780	.00825	.00930	.01000	.01110	.01751	.03580	.11413
4.0	.00675	.00720	.00800	.00870	.00927	.01454	.02920	.09471
6.0	.00490	.00520	.00600	.00640	.00692	.01147	.02272	.07470
8.0	.00370	.00400	.00460	.00490	.00538	.00872	.01826	.06098
10.0	.00260	.00285	.00330	.00360	.00408	.00669	.01533	.05614

Normal Force Coefficient

α(deg)\Mach →	.9	1.0	1.5	2.0	3.0	4.0	6.0	8.0	10.
0.	0.	0.	0.	0.	0.	0.	0.	0.	0.
20.	.54	.62	.540	.480	.380	.330	.240	.180	.136

APPENDIX C

REENTRY APPLICATIONS

C-1. INTRODUCTION

Two different sets of data are presented to show the maneuvering capability available for lifting entry when two different types of controls are used. The first shown as data set 1 below, uses the single parameter control $\phi_B = K\sigma$ discussed in the main part of this report. The second shown as data set 2 uses a combination of bank and angle-of-attack control to hold altitude constant after pull-out.

Three vehicles were used for this analysis: (1) a conventional circular missile having "low" (L/D) characteristics, (2) a reentry configuration having "medium" (L/D) characteristics, and (3) an aero-configured missile shape having "high" (L/D) characteristics. Sketches of these vehicles are shown in Figures C-1 through C-3 and the aerodynamic characteristics used are given in Appendix B. All three vehicles were used in developing data set 1 and the medium (L/D) vehicle was used to develop data set 2. All trajectories were initiated at 300,000 feet altitude and were terminated at a speed of 2,000 feet/second. This speed termination allowed the terminal altitude to vary from 50,000 to 80,000 feet. The data shown represent aerodynamic capability only. No constraints, such as aerodynamic heating have been imposed.

C-2. DATA SET 1, (L/D) MAX TRAJECTORIES

Reentry footprints were generated using (L/D) max and the single parameter control for the major portion of the footprint boundary and C_L max for minimum down-range. Initial conditions include entry velocities (inertial) which vary from 20,000 to 24,800 feet/second and entry path angles from -1.5 to -25 degrees. These data are shown in Figures C-4 through C-33. Data set 1 therefore contains a complete set of footprints for the three configurations and can be used as a reference for maneuvering capability available for a range of configuration types and initial conditions.

C-3. DATA SET 2, CONSTANT ALTITUDE TURNS

This data set is for trajectories where the altitude is held constant during the turn. All trajectories were flown at zero bank angle and at L/D max until the initial pull-out, $\gamma = 0$. For straight down-range with no turns, the angle-of-attack was set to hold level flight after pull-out until L/D max was reached. From this point on the trajectories were flown at L/D max. For three-dimensional trajectories, turns were initiated at the pull-out point. The angle-of-attack was set to that required for L/D max and level flight was maintained by varying the bank angle. The footprints were generated by varying the amount of turn allowed. Once a specified heading change had been reached, the bank was set to zero and the altitude allowed to vary for the remainder of the trajectory.

Entry conditions include variations in initial velocity (inertial) from 12,000 to 25,800 feet/second and entry path angles from -5 to -25 degrees. Constant velocity (iso-velocity) contours are shown for 2000, 4000, 6000, 8000, and 10,000 feet/second.

The altitude at the initial pull-out point and the corresponding range are shown in Figures C-34 and C-35, respectively, for the parametric variations in entry velocity and path angle considered. The iso-velocity contours are shown in Figures C-36 through C-54. The dashed line closing the back side of these contours represents the maximum amount of turn possible when using bank angle to maintain constant altitude during the turn with the angle-of-attack set for L/D max. To obtain a faster rate of turn than shown by the dashed line without increasing angle-of-attack a steeper bank angle would be required allowing altitude to decrease during the turn. A heading can be obtained for any of the possible trajectories within the envelope by taking a tangency point to this dashed line and drawing a straight line through the iso-velocity contours. An example is shown in Figure C-36 for changes in heading $\Delta\sigma$, of 30, 45, and 90 degrees.

Data set 2 (Figures C-36 through C-54) then contains a set of footprints for the medium L/D configuration showing the maneuvering capability available if the turn is performed at level altitude after pull-out. The pull-out altitude is the same as used in data set 1. Hence, a comparison of data set 2 with the medium L/D configuration of data set 1 (Figures C-14 to C-23) shows the large loss in maneuvering due to the constant altitude turn.

For example comparing an entry velocity of 25800 feet/second it can be seen that the maximum cross-range of 3200 nmi of Figure C-21 is much larger than the 930 nmi of Figure C-46.

168

W = 2500 lb
S = 35.4 ft^2
W/S = 70. lb/ft^2
Dia = 24 in

36

60°
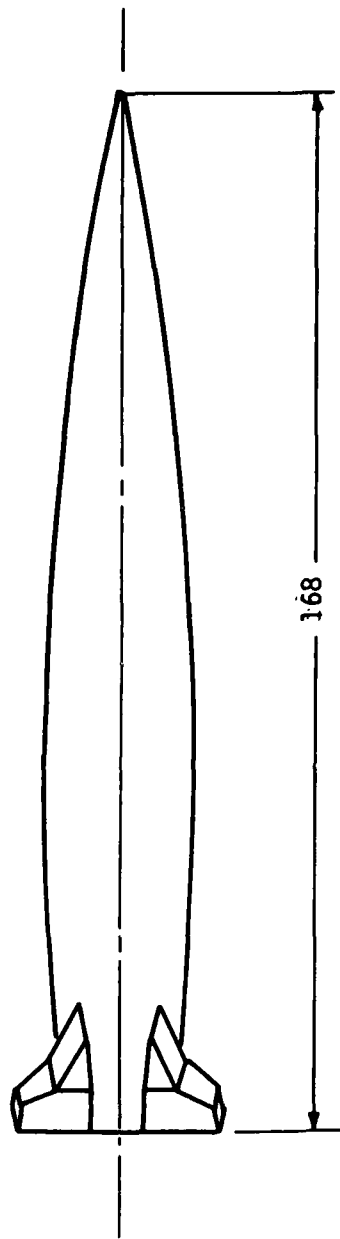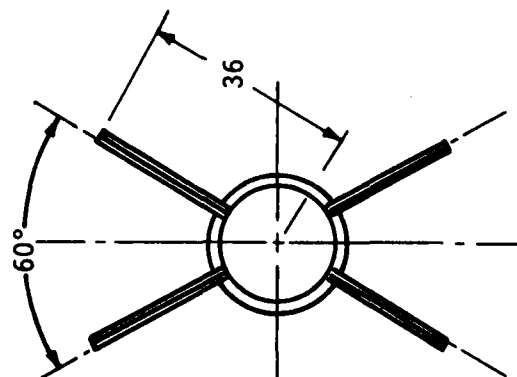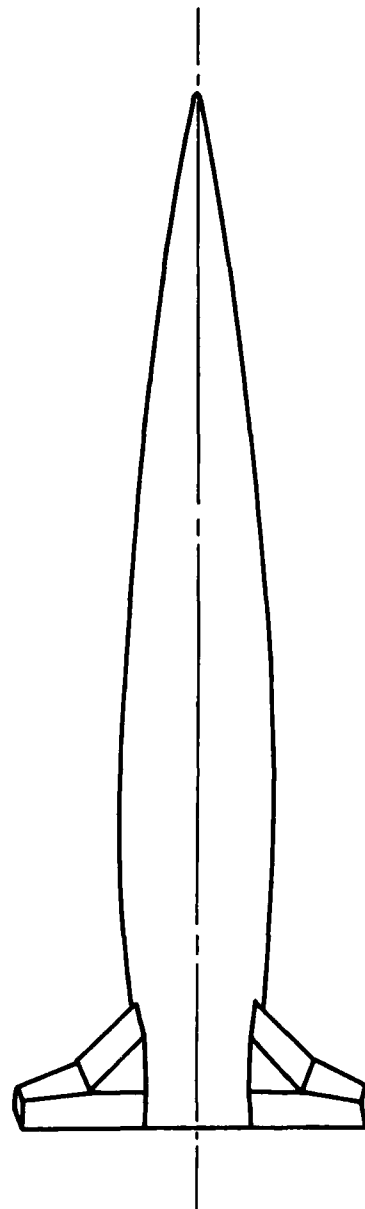
Figure C-1. Low (L/D) Configuration

$S = 35.38 \text{ ft}^2$
$W = 2500 \text{ lb}$
$W/S = 70 \text{ lb/ft}^2$

32.1

Dimensions in inches

60.65

168
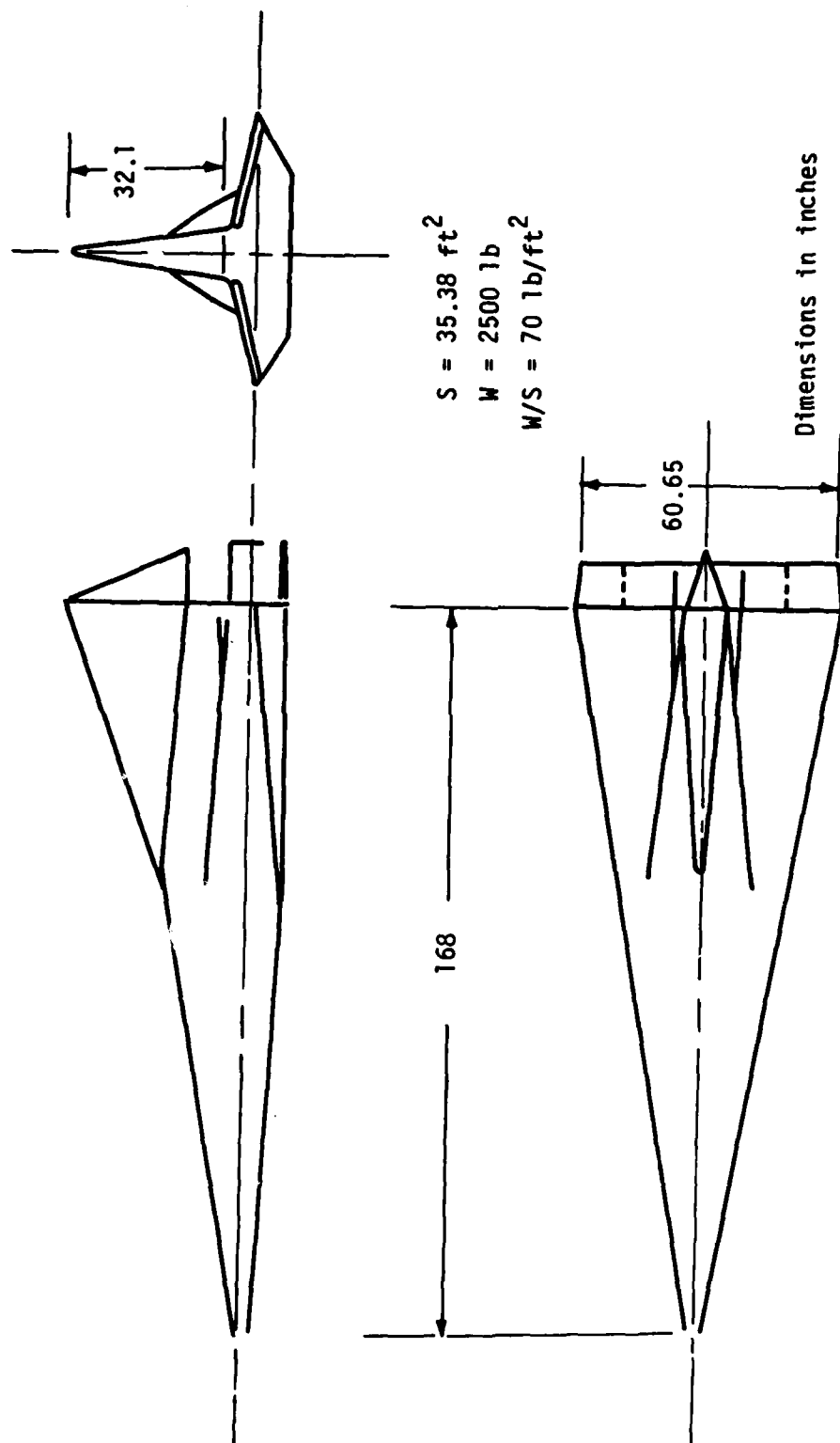
Figure C-2. Medium (L/D) Vehicle

78

67.2

151.6

Dimension in inches

W = 2500 lb
S = 35.4 ft^2
W/S = 70 lb/ft^2

15°
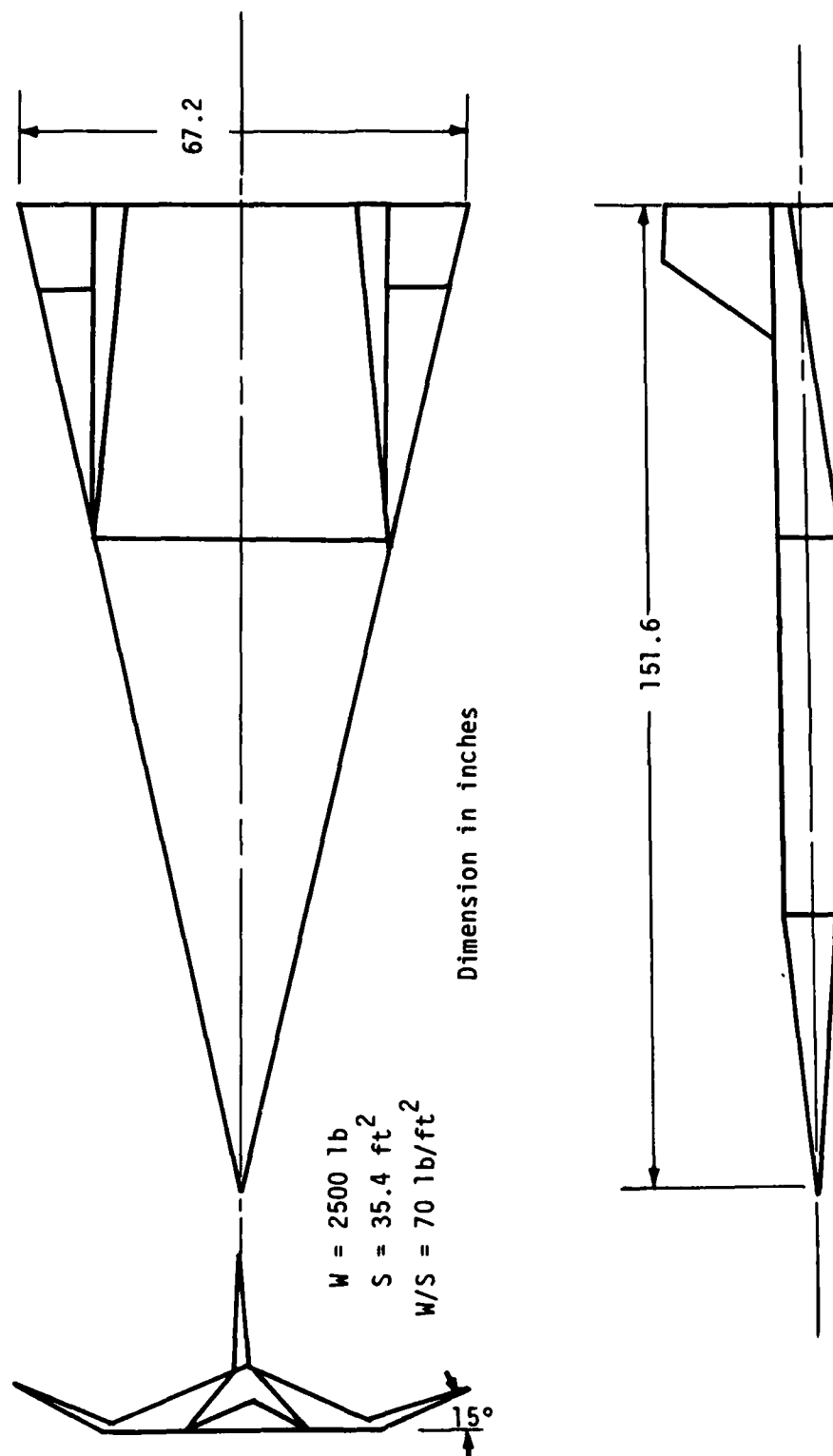
Figure C-3. High (L/D) Configuration

CIRCULAR MISSILE

$\gamma_E = -1.5°$

$\sigma_i = 90°$

$\theta = \emptyset = 0°$

W/S = 120 PSF

LOW L/D

$(V_I)_i = 25,800$ fps

DOWN-RANGE ~ KN.MI.

CROSS-RANGE ~ KN.MI.
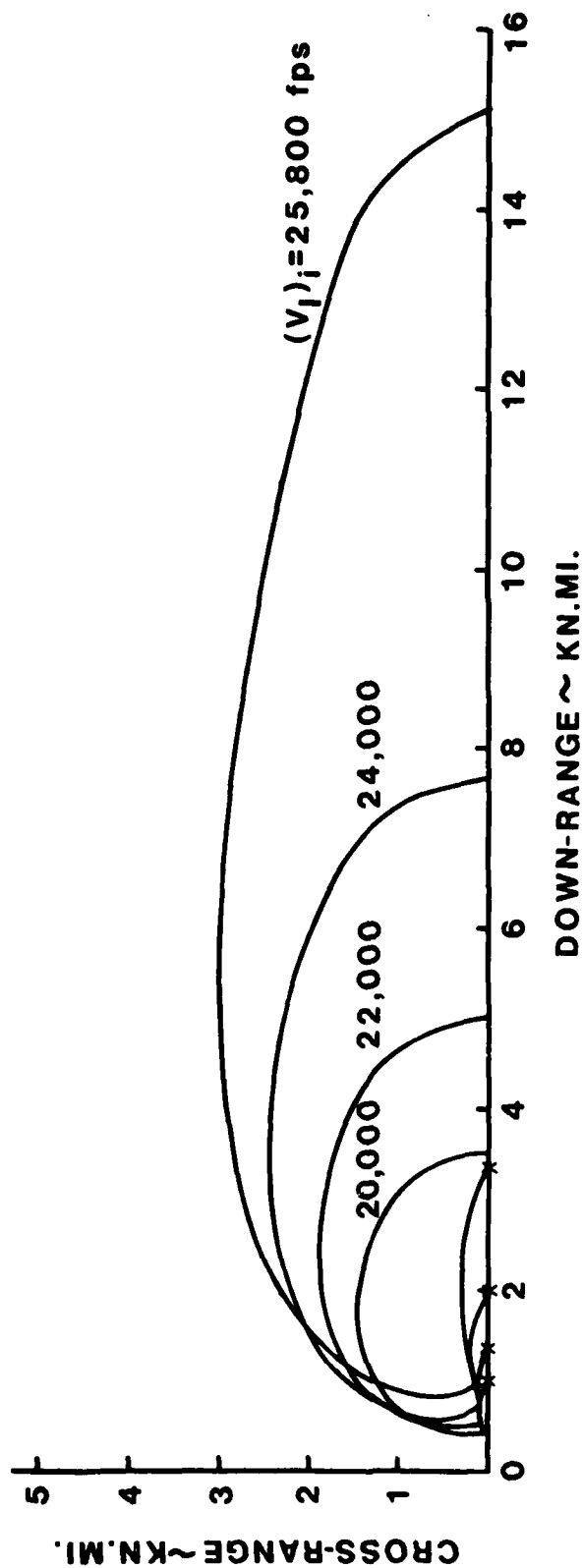
Figure C-4. Low (L/D) Footprint, Entry Angle = -1.5°

CIRCULAR MISSILE

$\delta_E = -2.0°$

$\sigma_i = 90°$

$\theta = \emptyset = 0°$

W/S = 120 PSF

LOW L/D

$(V_I)_i = 25,800$ fps

24,000

22,000

20,000

DOWN-RANGE ~ KN.MI.

CROSS-RANGE ~ KN.MI.
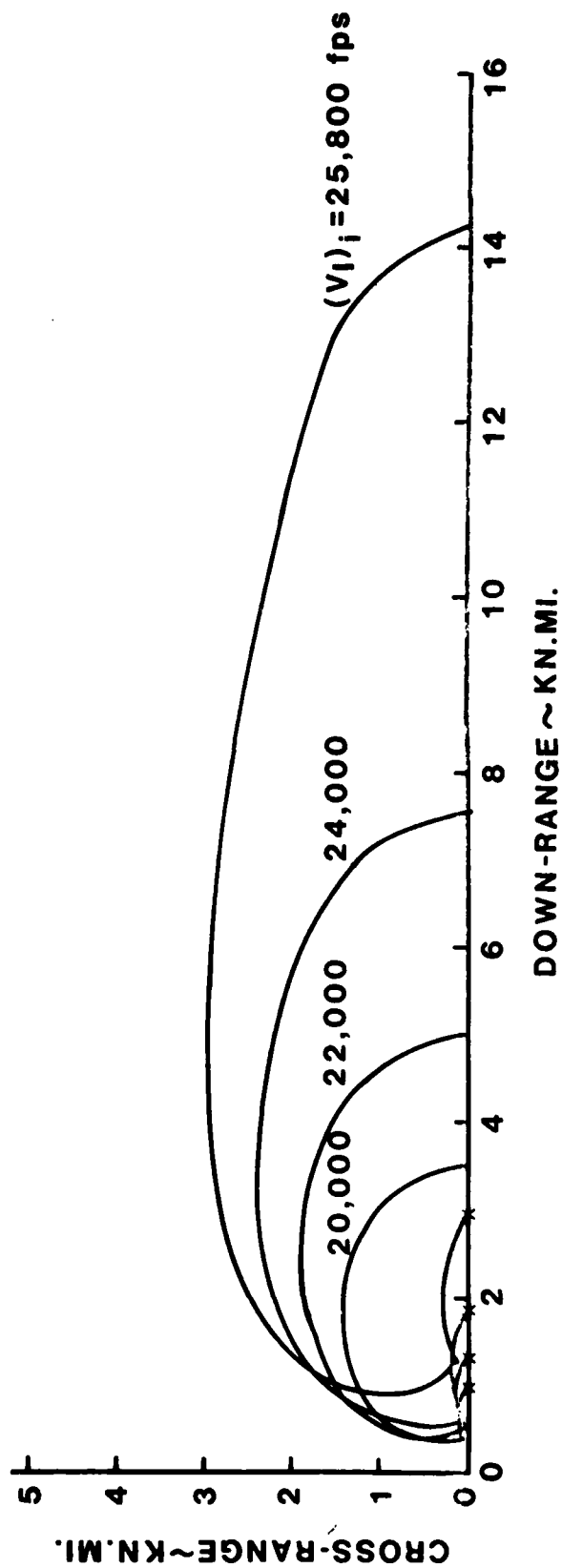
Figure C-5. Low (L/D) Footprint, Entry Angle = -2°

81
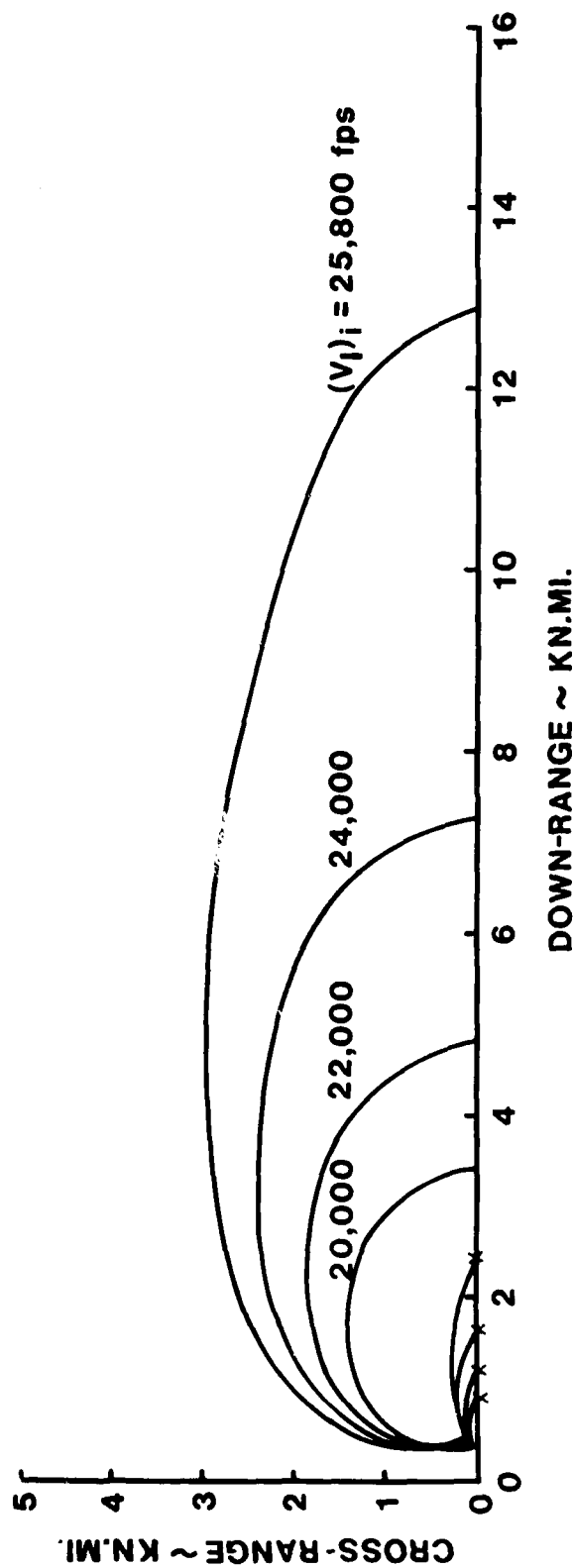
Figure C-6. Low (L/D) Footprint, Entry Angle = -3°
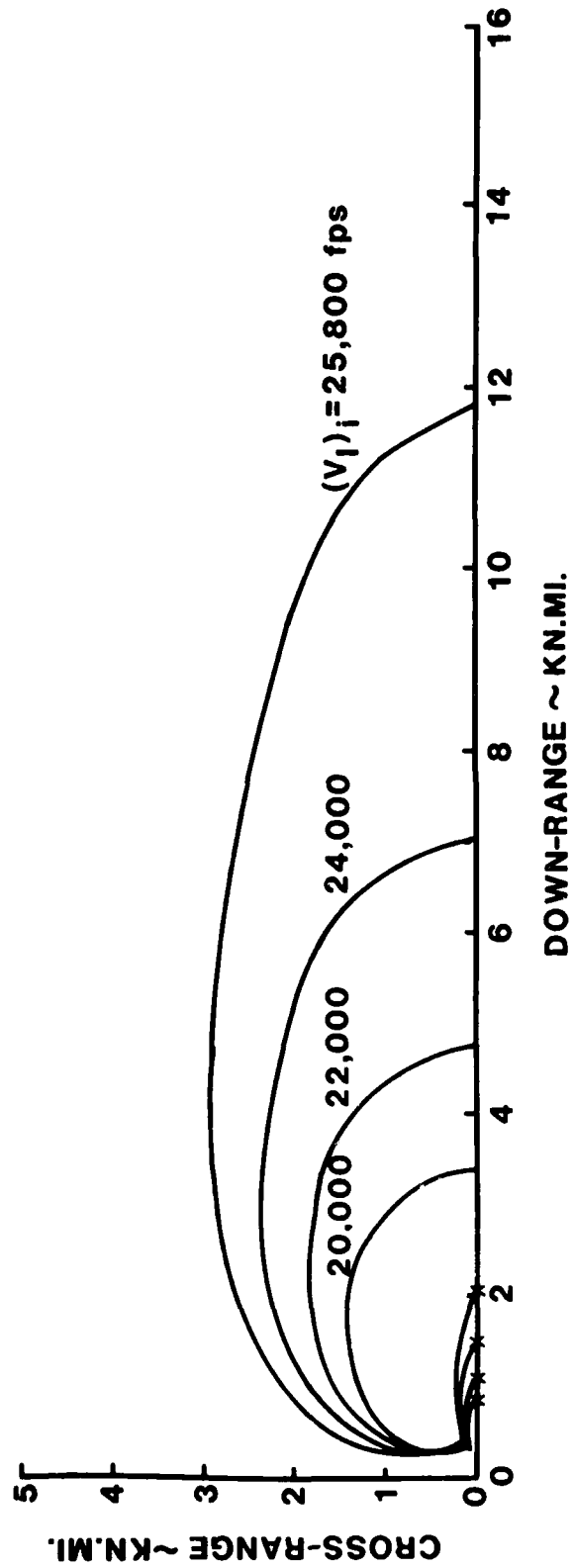
Figure C-7. Low (L/D) Footprint, Entry Angle = -4°

CIRCULAR MISSILE

$\gamma_E = -5.0°$

$\sigma_i = 90°$

$\theta = \phi = 0°$

W/S = 120 PSF

LOW L/D

$(V_I)_i = 25,800$ fps

24,000

22,000

20,000

DOWN-RANGE ~ KN.MI.

CROSS-RANGE ~ KN.MI.
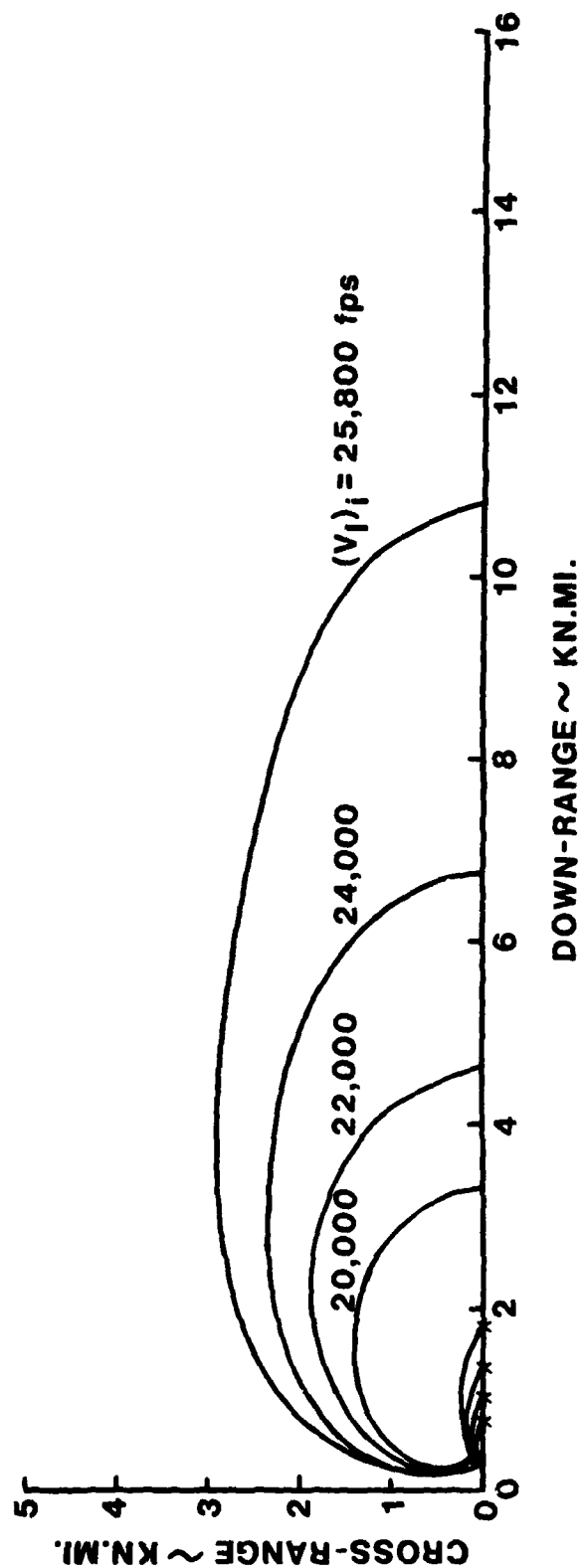
Figure C-8. Low (L/D) Footprint, Entry Angle = -5°
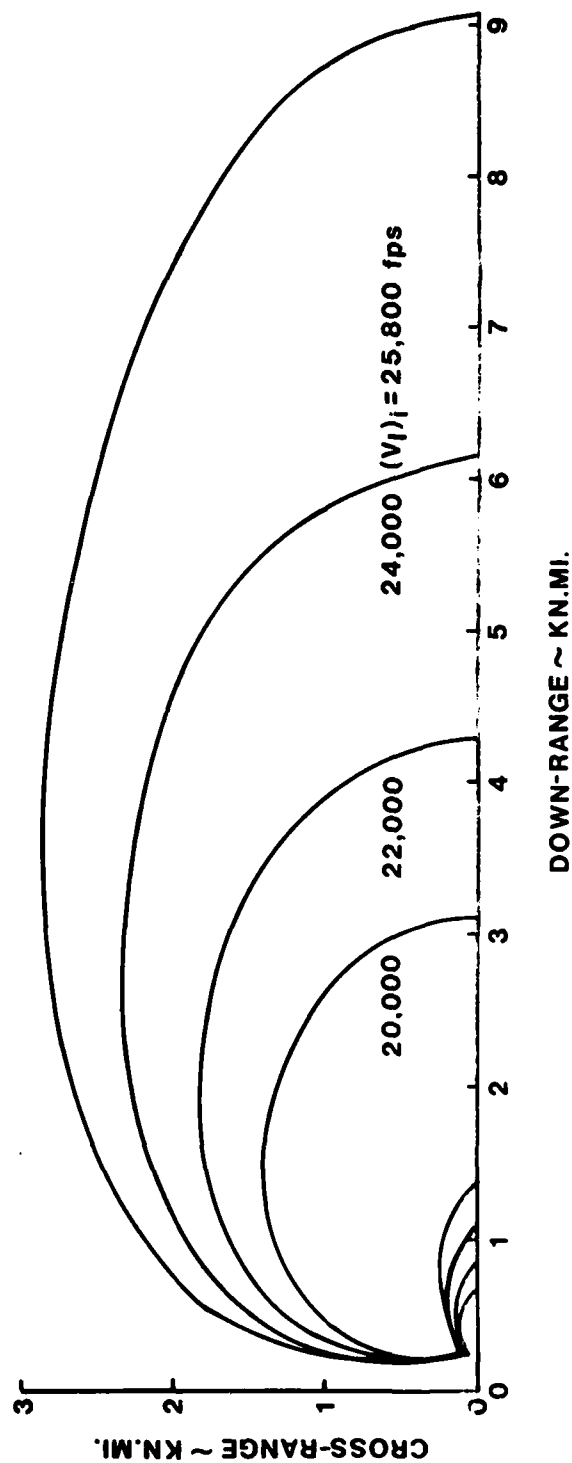
Figure C-9. Low (L/D) Footprint, Entry Angle = -7.5°

LOW (L/D)

$\gamma_E = -10.0°$

$\sigma_i = 90.0°$

$\theta = \phi = 0°$
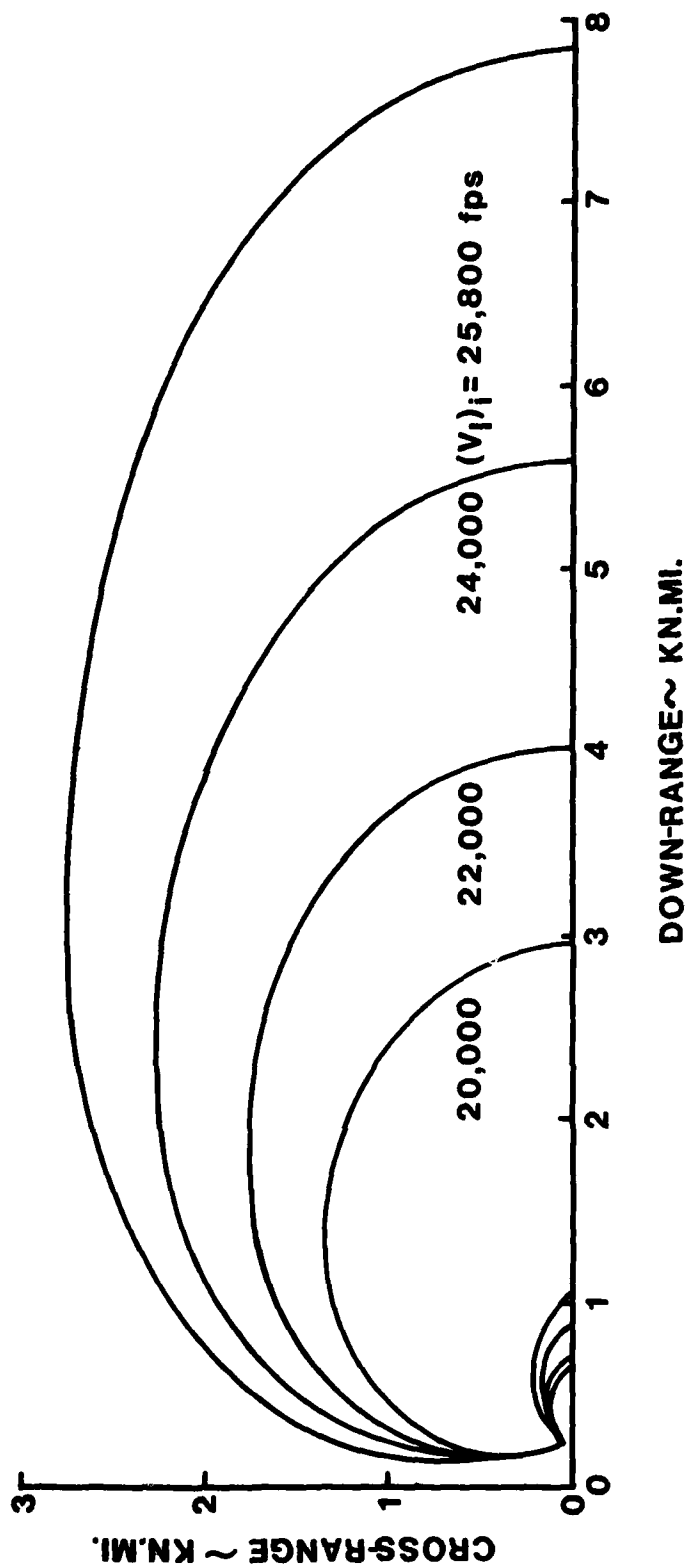
Figure C-10. Low (L/D) Footprint, Entry Angle = -10°

DOWN-RANGE~ KN.MI.

CROSS-RANGE ~ KN.MI.

$(V_I)_i = 25,800$ fps

24,000

22,000

20,000
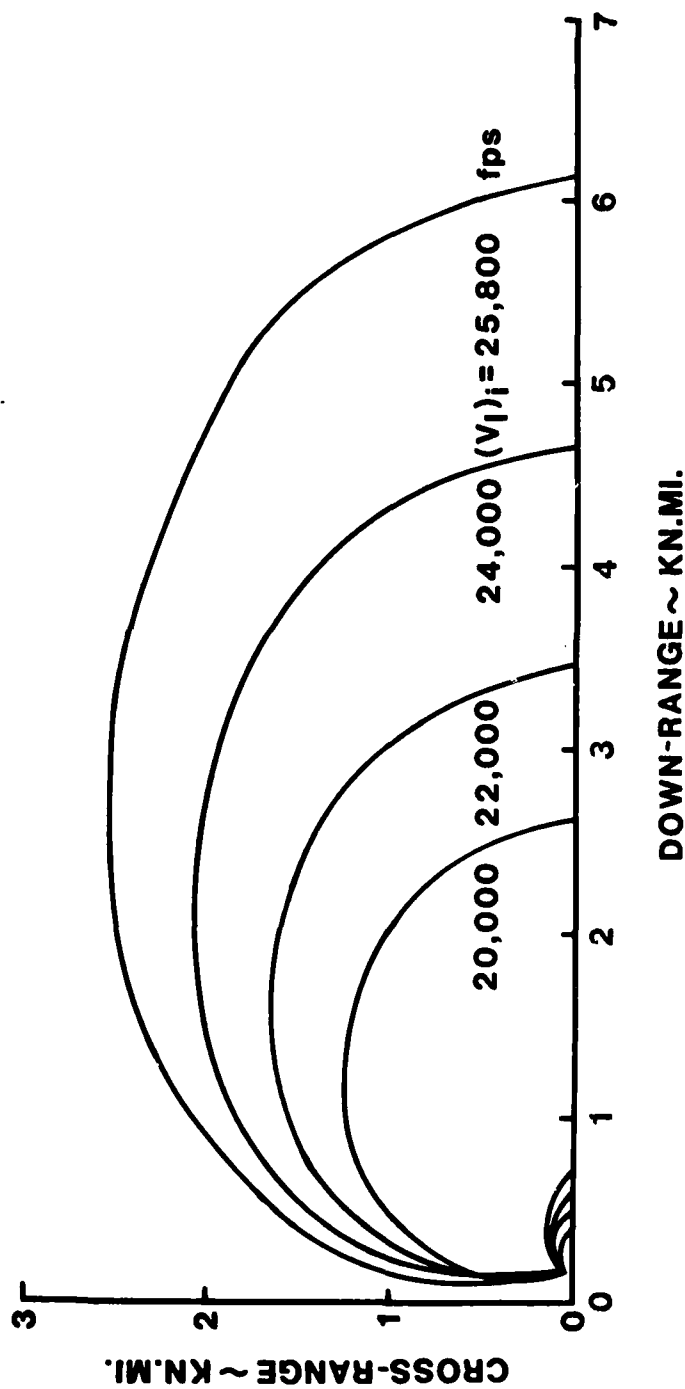
Figure C-11. Low (L/D) Footprint, Entry Angle = -15°

LOW (L/D)

$\delta_E = -20°$

$\sigma_i = 90°$

$\theta = \phi = 0°$

DOWN-RANGE ~ KN.MI.

CROSS-RANGE ~ KN.MI.

$(V_I)_i = 25,800$ fps

20,000   22,000   24,000
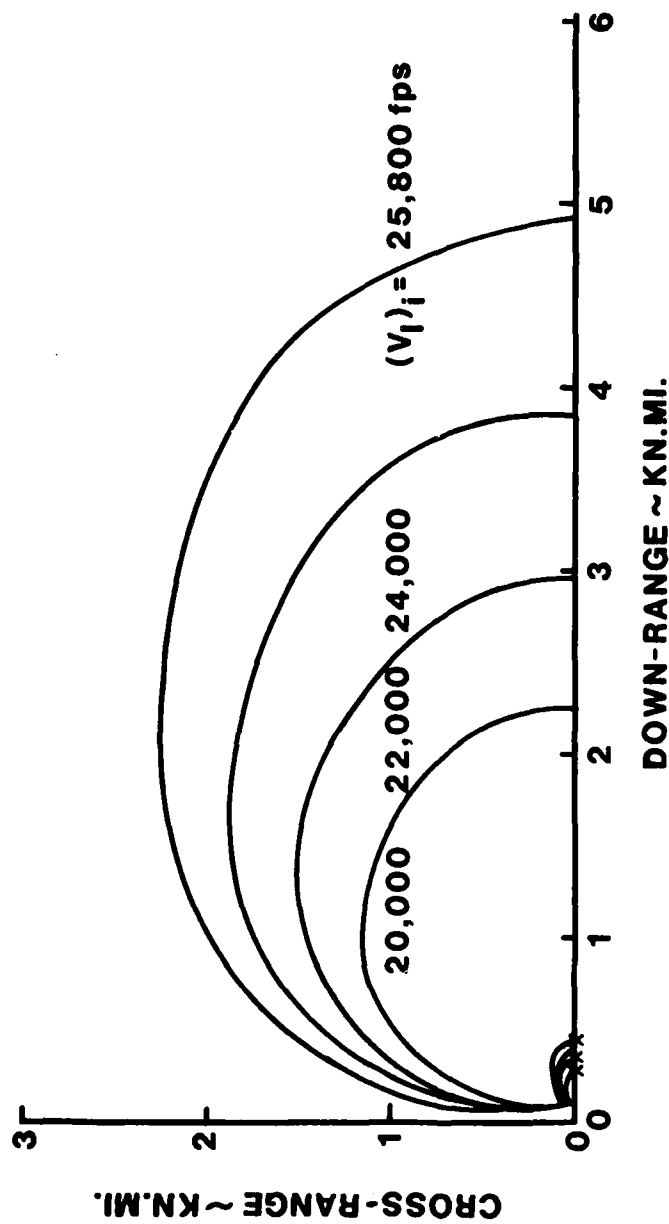
Figure C-12.   Low (L/D) Footprint, Entry Angle = -20°

LOW (L/D)

$\gamma_E = -25°$

$\sigma_i = 90°$

$\theta = \emptyset = 0°$
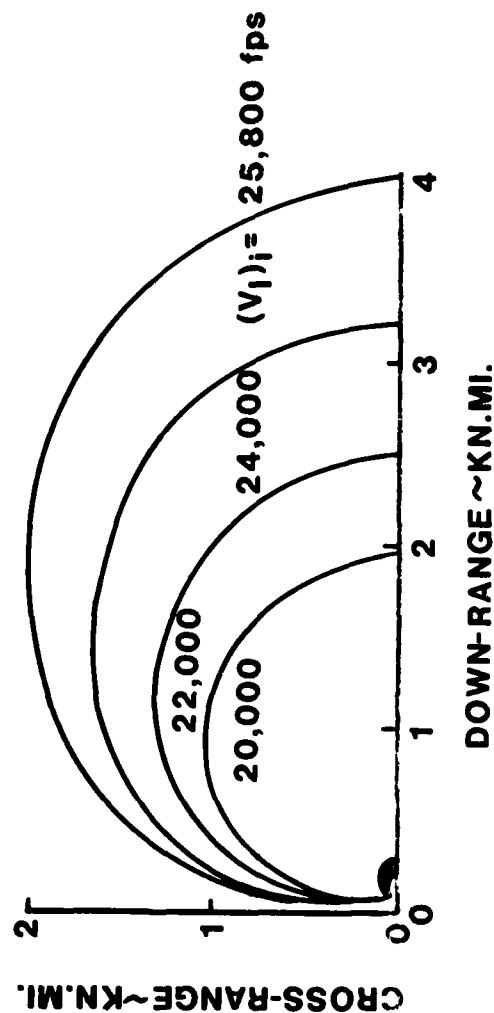
Figure C-13. Low (L/D) Footprint, Entry Angle = -25°

MEDIUM (L/D)

$\gamma_E = -1.5°$

$\sigma_i = 90°$

$\theta = \phi = 0°$

W/S = 70 PSF
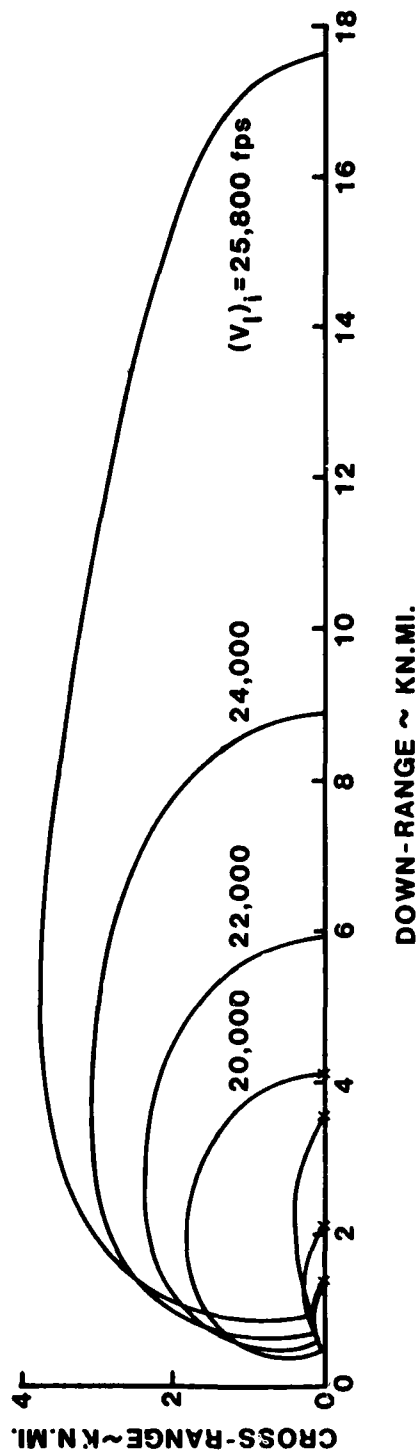
Figure C-14. Medium (L/D) Footprint, Entry Angle = -1.5°

MEDIUM (L/D)

$\delta_E = -2.0°$

$\sigma_i = 90°$

$\Theta = \phi = 0°$

W/S = 70 PSF
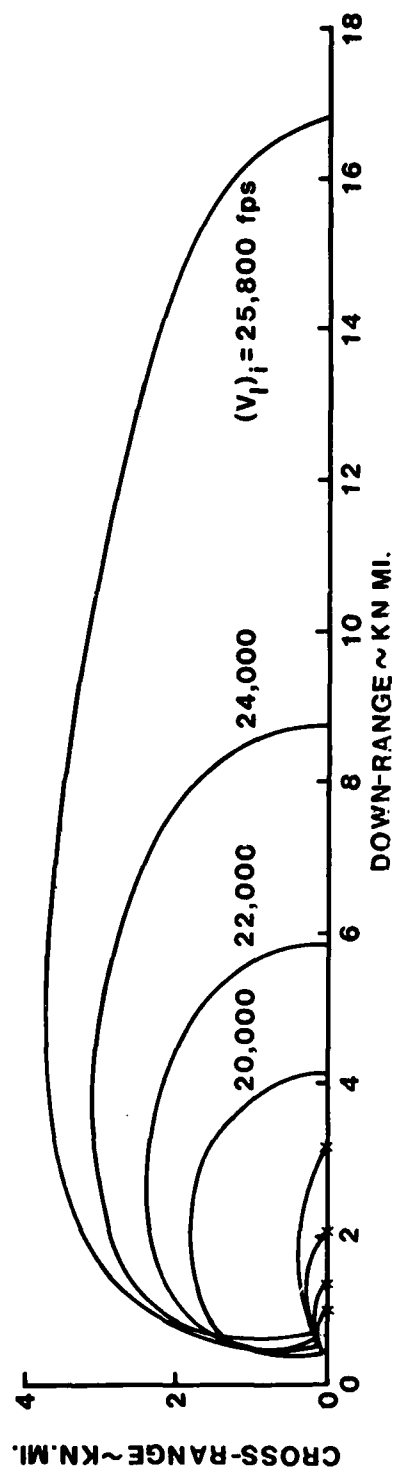
Figure C-15. Medium (L/D) Footprint, Entry Angle = -2°

MEDIUM (L/D)

$\gamma_E = -3.0°$

$\sigma_i = 90°$

$\theta = \phi = 0°$

W/S = 70 PSF
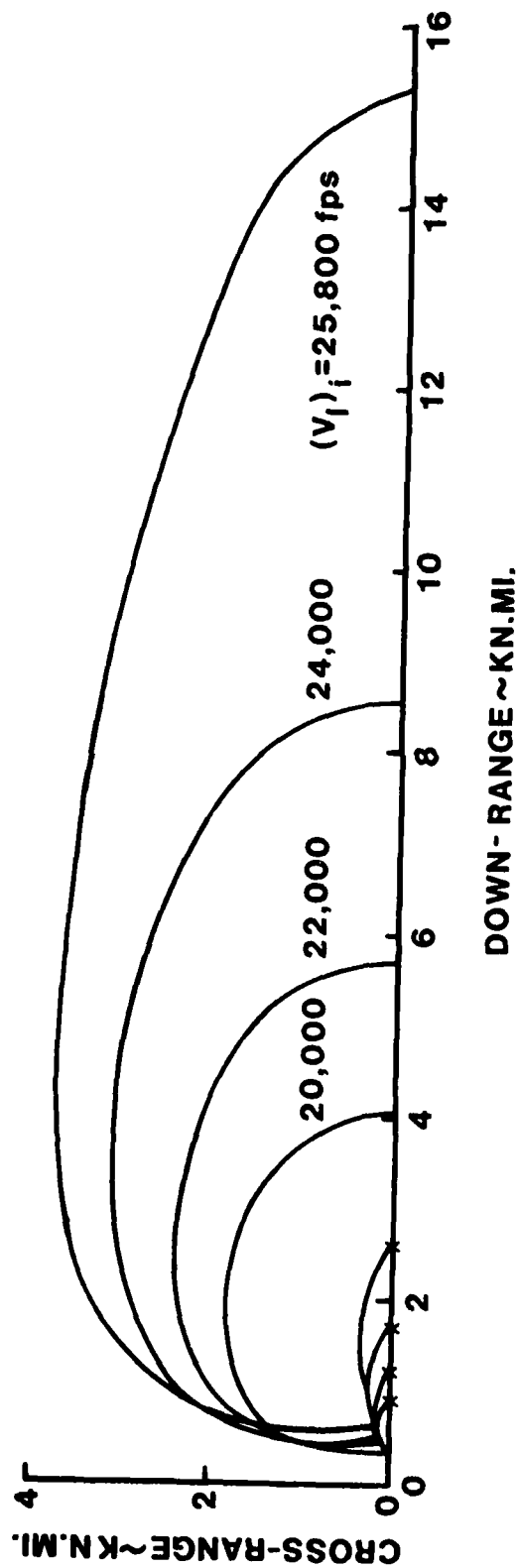
Figure C-16. Medium (L/D) Footprint, Entry Angle = -3°

MEDIUM (L/D)

$\gamma_E = -4.0°$

$\sigma_i = 90°$

$\theta = \emptyset = 0°$

W/S = 70 PSF
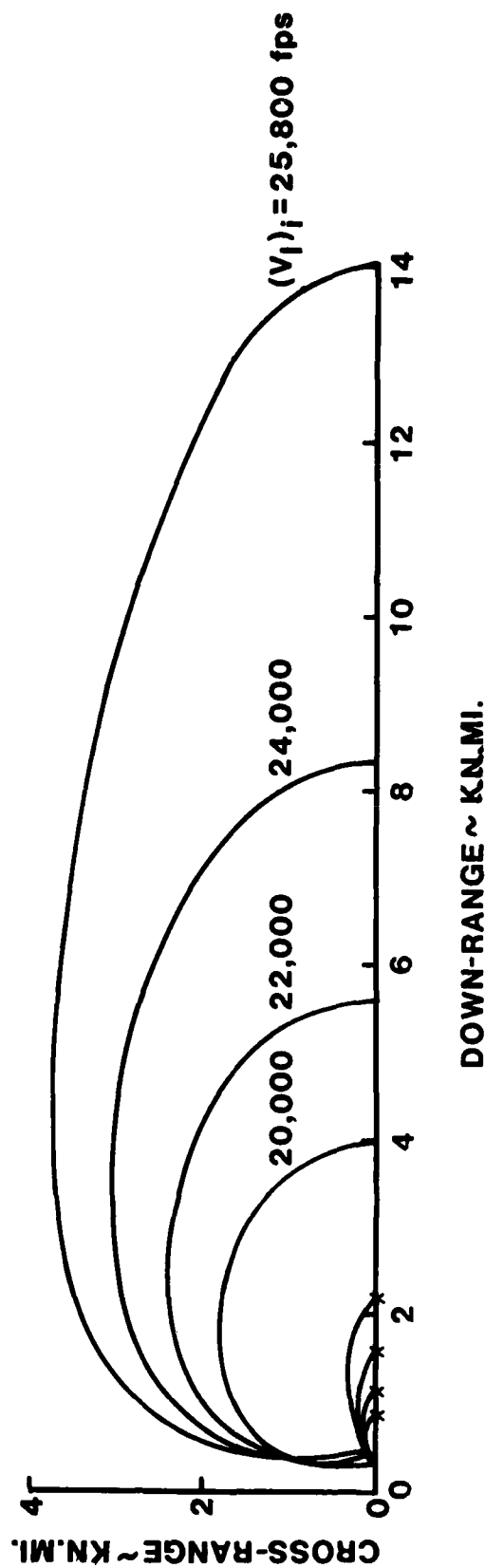
Figure C-17. Medium (L/D) Footprint, Entry Angle = -4°

MEDIUM (L/D)

$\gamma_E = -5.0°$

$\sigma_i = 90°$

$\theta = \phi = 0°$

W/S = 70 PSF
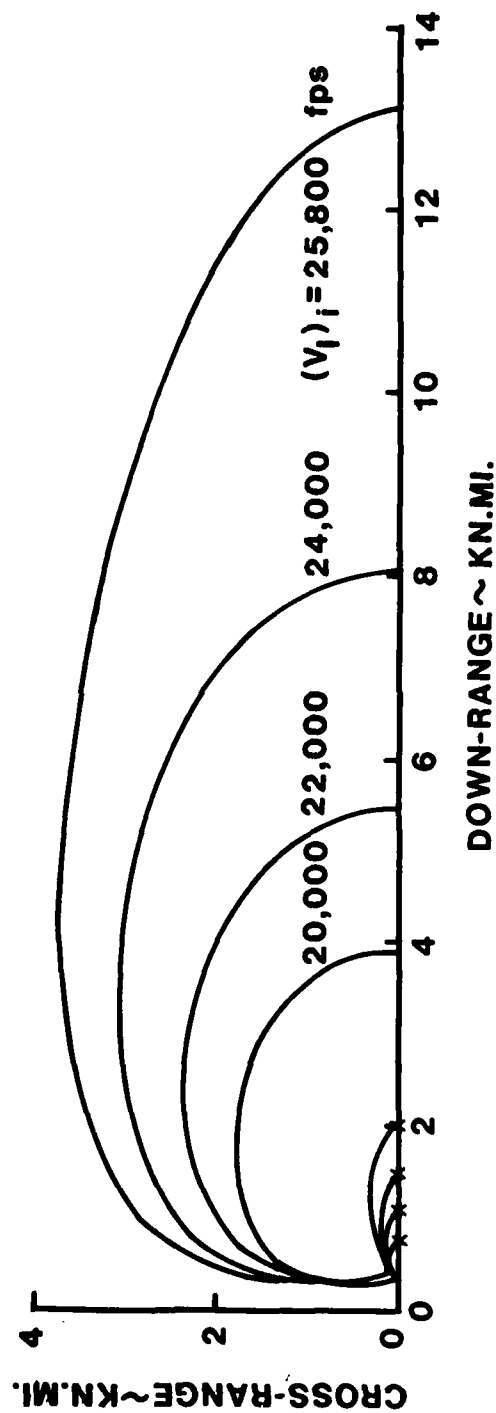
Figure C-18. Medium (L/D) Footprint, Entry Angle = -5°

MEDIUM (L/D)

$\gamma_E = -7.5°$

$\sigma_i = 90°$

$\theta = \phi = 0°$

$(V_I)_i = 25,800$ fps

CROSS-RANGE ~ KN.MI.

DOWN-RANGE ~ KN.MI.

20,000 22,000 24,000
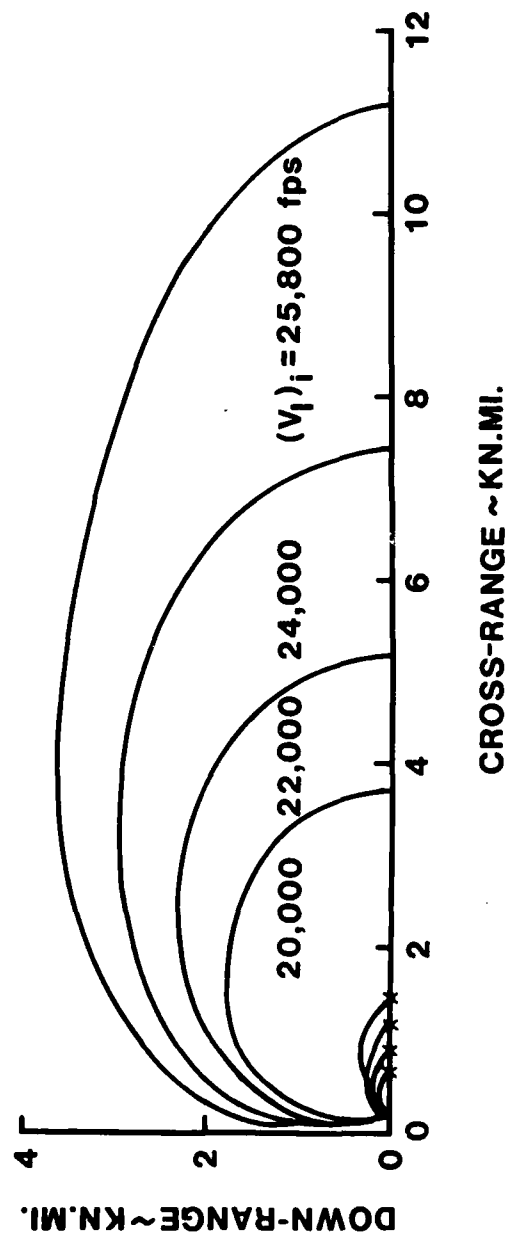
Figure C-19. Medium (L/D) Footprint, Entry Angle = -7.5°

MEDIUM (L/D)

$\gamma_E = -10°$

$\sigma_i = 90°$

$\Theta = \phi = 0°$
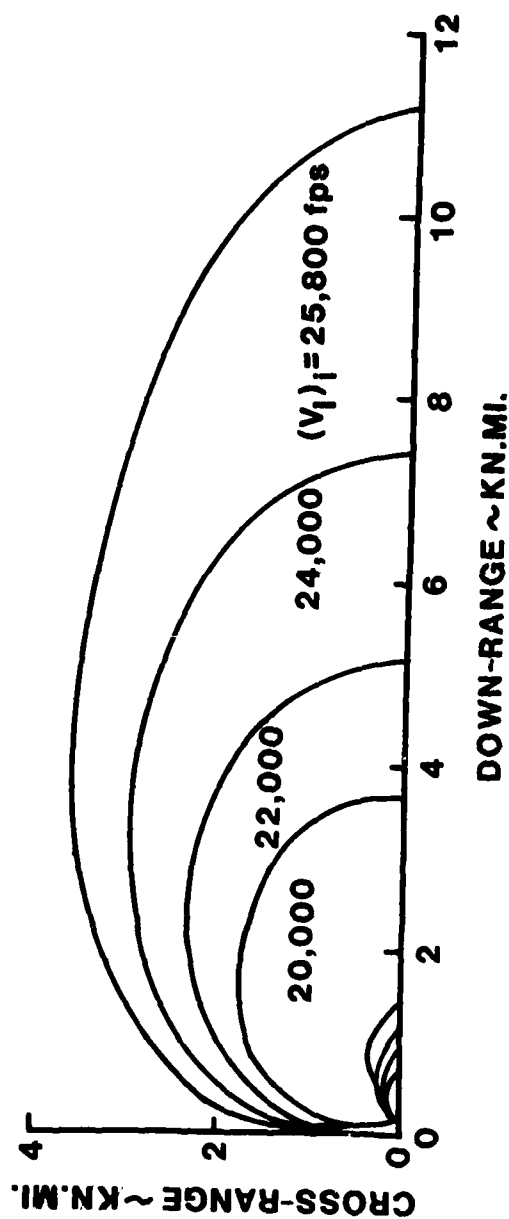
Figure C-20. Medium (L/D) Footprint, Entry Angle = -10°

96

MEDIUM (L/D)

$\gamma_E = -15°$

$\sigma_i = 90°$

$\Theta = \phi = 0°$

CROSS-RANGE ~ KN.MI.

DOWN-RANGE ~ KN.MI.

$(V_I)_i = 25,800$ fps

24,000

22,000

20,000
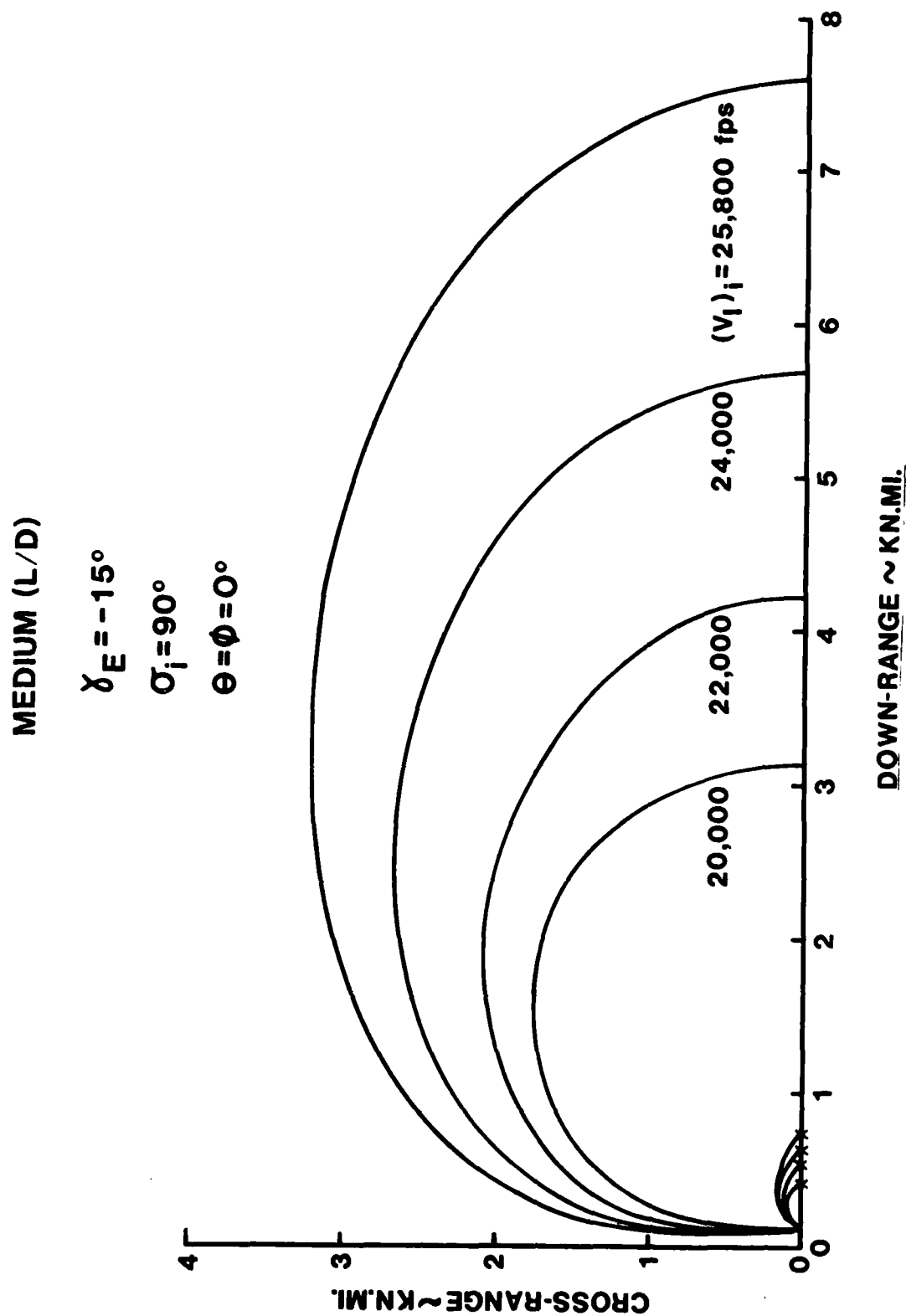
Figure C-21. Medium (L/D) Footprint, Entry Angle = -15°

Figure C-22. Medium (L/D) Footprint, Entry Angle = -20°

MEDIUM (L/D)

$\gamma_E = -25°$

$\sigma_i = 90°$

$\theta = \phi = 0°$

20,000 22,000 24,000 $(V_1)_i = 25,800$ fps

DOWN-RANGE ~ KN.MI.

CROSS-RANGE ~ KN.MI.
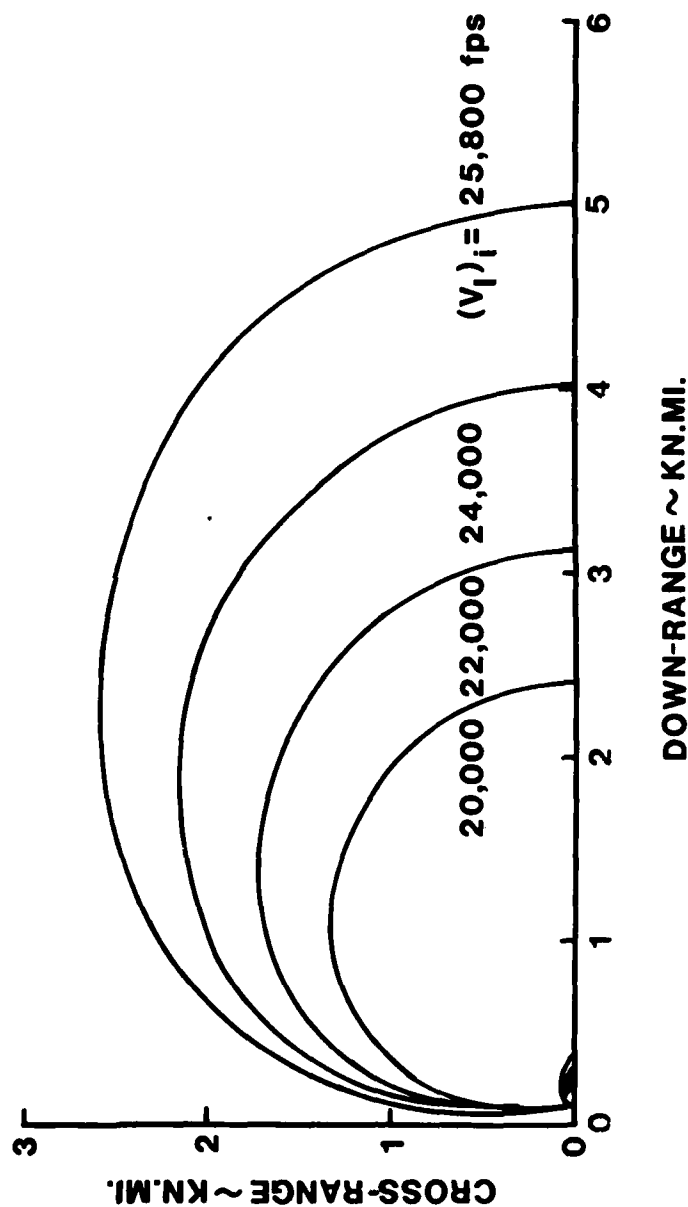
Figure C-23. Medium (L/D) Footprint, Entry Angle = -25°

99
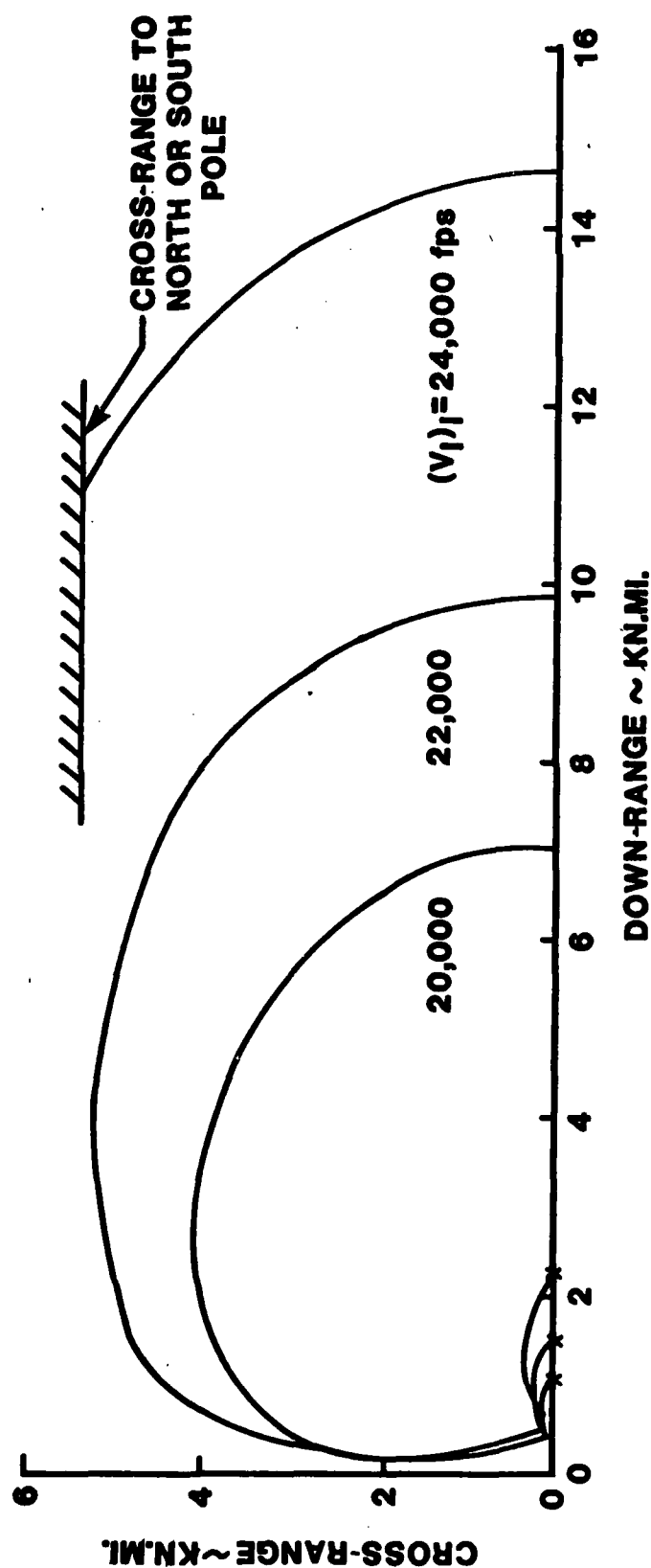
Figure C-24. High (L/D) Footprint, Entry Angle = -1.5°
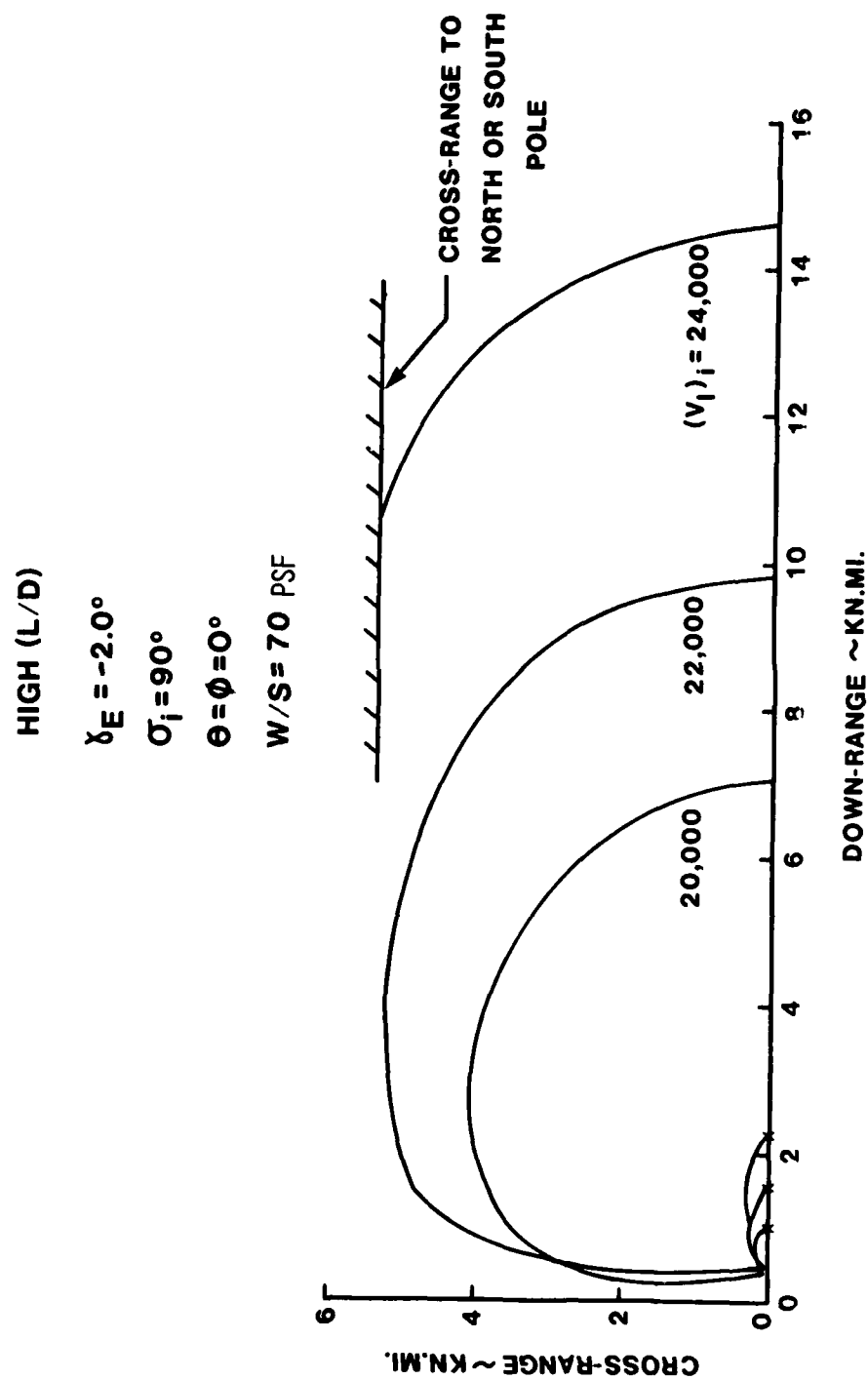
Figure C-25. High (L/D) Footprint, Entry Angle = -2°

HIGH (L/D)

$\gamma_E = -3.0°$

$\sigma_i = 90°$

$\theta = \phi = 0°$

W/S = 70 PSF

CROSS-RANGE TO
NORTH OR SOUTH
POLE

$(V_1)_i = 24,000$ fps

22,000

20,000

DOWN-RANGE ~ KN.MI.

CROSS-RANGE ~ KN.MI.
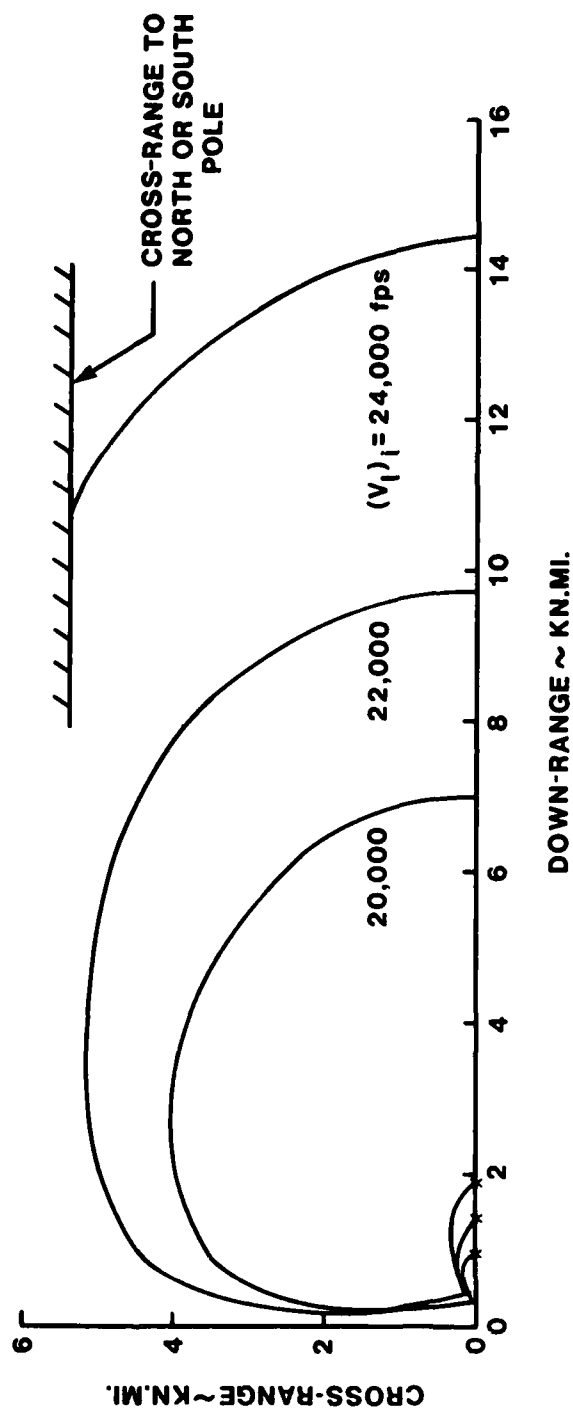
Figure C-26. High (L/D) Footprint, Entry Angle = -3°

HIGH (L/D)

$\gamma_E = -4.0°$

$\sigma_i = 90°$

$\Theta = \emptyset = 0°$

W/S = 70 PSF

CROSS-RANGE TO NORTH OR SOUTH POLE

$(V_I)_i = 24,000$ fps

22,000

20,000

DOWN-RANGE ~ KN.MI.

CROSS-RANGE ~ KN.MI.
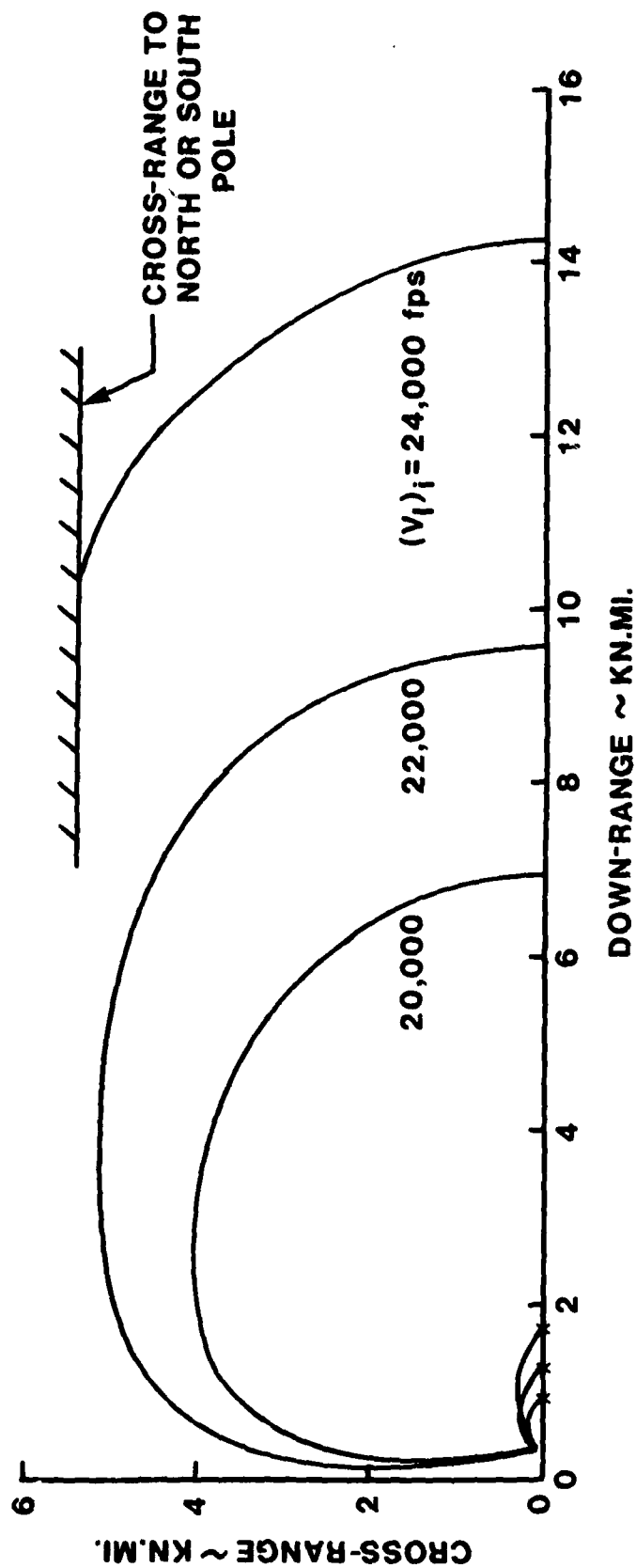
Figure C-27. High (L/D) Footprint, Entry Angle = -4°

HIGH (L/D)

$\gamma_E = -5.0°$

$\sigma_i = 90°$

$\theta = \phi = 0°$

W/S=70 PSF

CROSS-RANGE TO
NORTH OR SOUTH
POLE

$(V_l)_i = 24,000$ fps

22,000

20,000

DOWN-RANGE ~ KN.MI.

CROSS-RANGE ~ KN.MI.
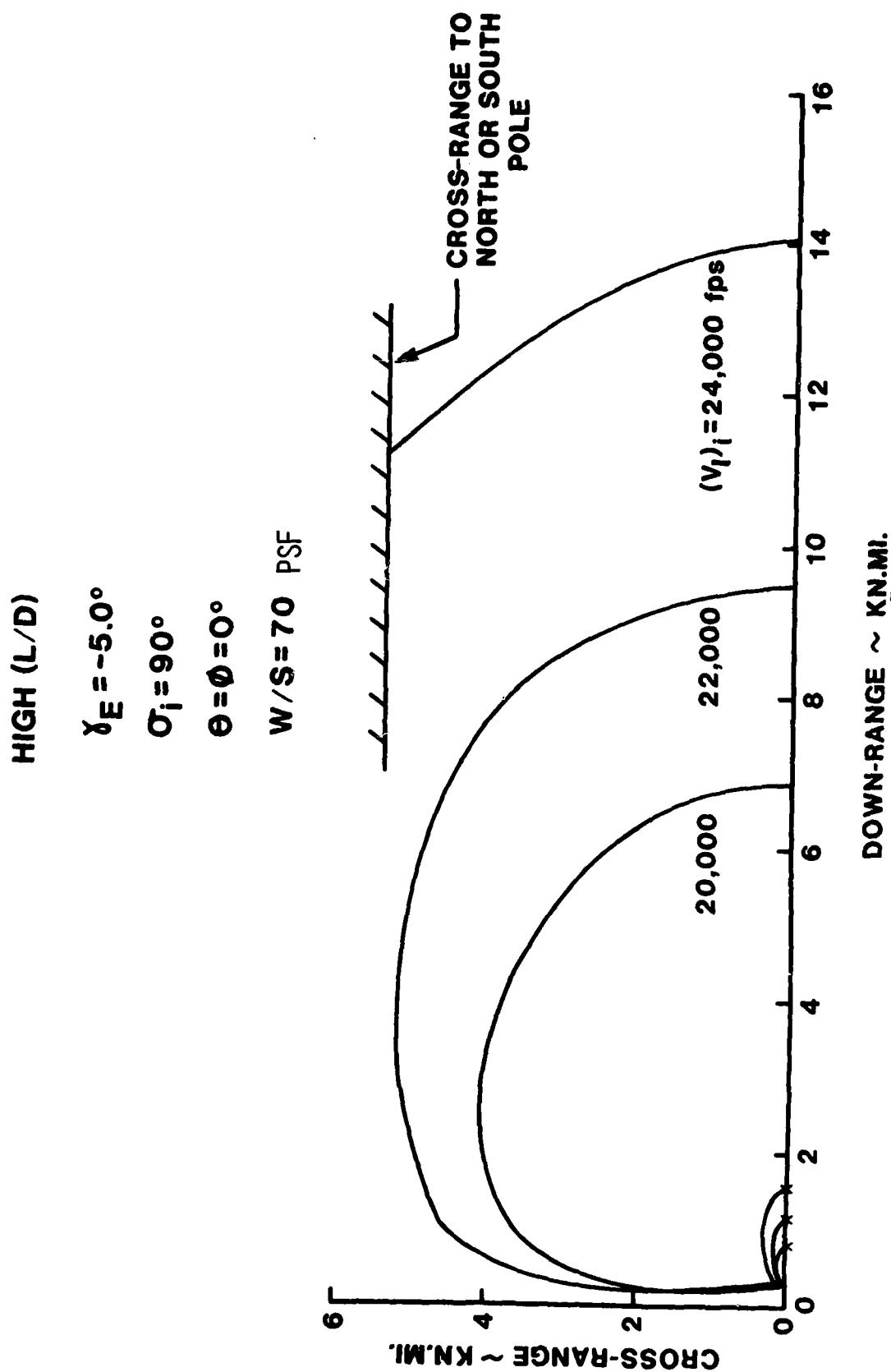
Figure C-28. High (L/D) Footprint, Entry Angle = -5°

HIGH (L/D)

$\gamma_E = -7.5°$

$\sigma_i = 90°$

$\theta = \phi = 0°$
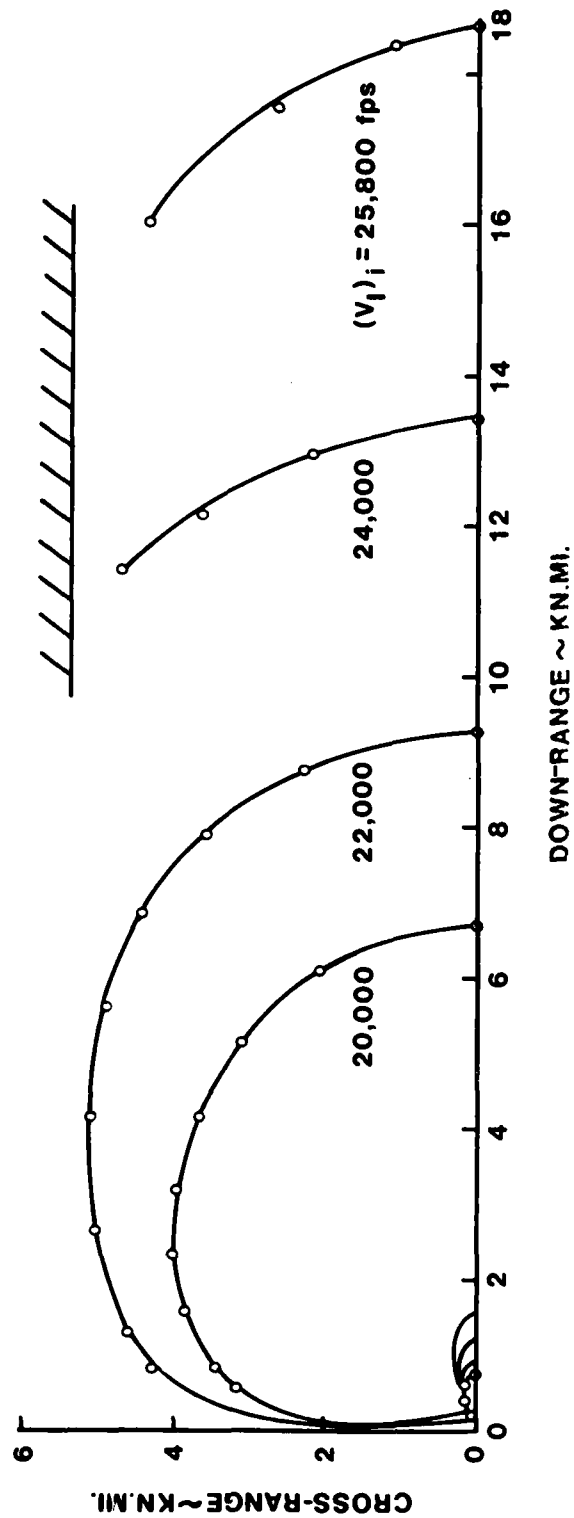
Figure C-29. High (L/D) Footprint, Entry Angle = -7.5°

Figure C-30. High (L/D) Footprint, Entry Angle = -10°

HIGH (L/D)

$\gamma_E = -10°$

$\sigma_i = 90°$

$\Theta = \phi = 0°$

$(V_I)_i = 25,800$ fps

20,000 22,000 24,000

DOWN-RANGE ~KN.MI.

CROSS-RANGE ~KN.MI.

HIGH (L/D)

$\gamma_E = -15°$

$\sigma_i = 90°$

$\theta = \emptyset = 0°$

$(V_I)_i = 25,800$ fps

24,000

22,000

20,000
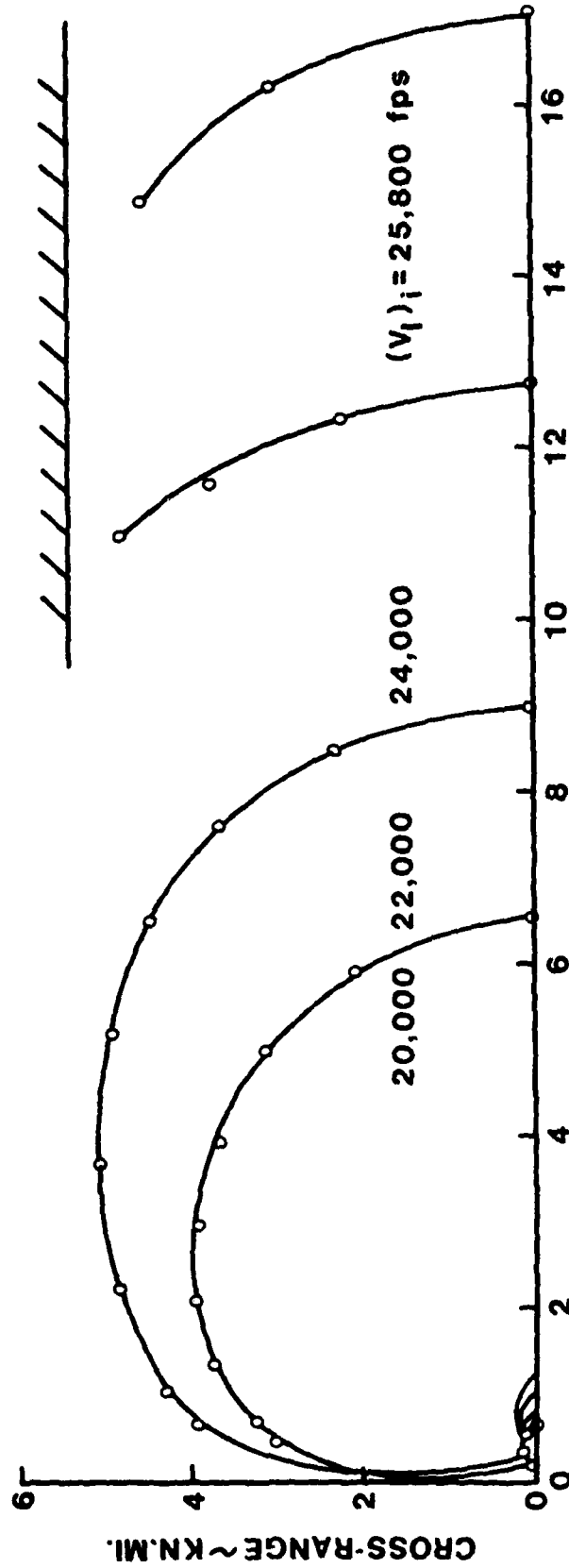
DOWN-RANGE ~KN.MI.

CROSS-RANGE~KN.MI.
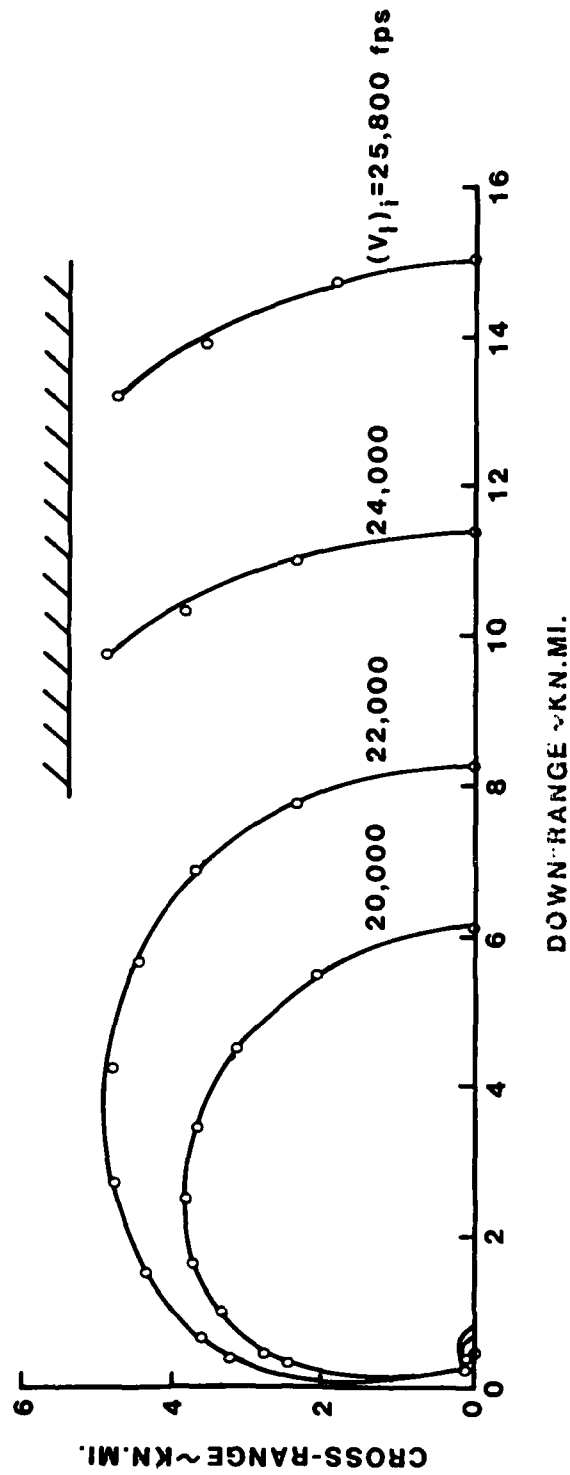
Figure C-31. High (L/D) Footprint, Entry Angle = -15°

HIGH (L/D)

$\delta_E = -20°$

$\sigma_i = 90°$

$\theta = \phi = 0°$

$(V_I)_i = 25,800$ fps

DOWN-RANGE ~ KN.MI.

CROSS-RANGE ~ KN.MI.

20,000   22,000   24,000
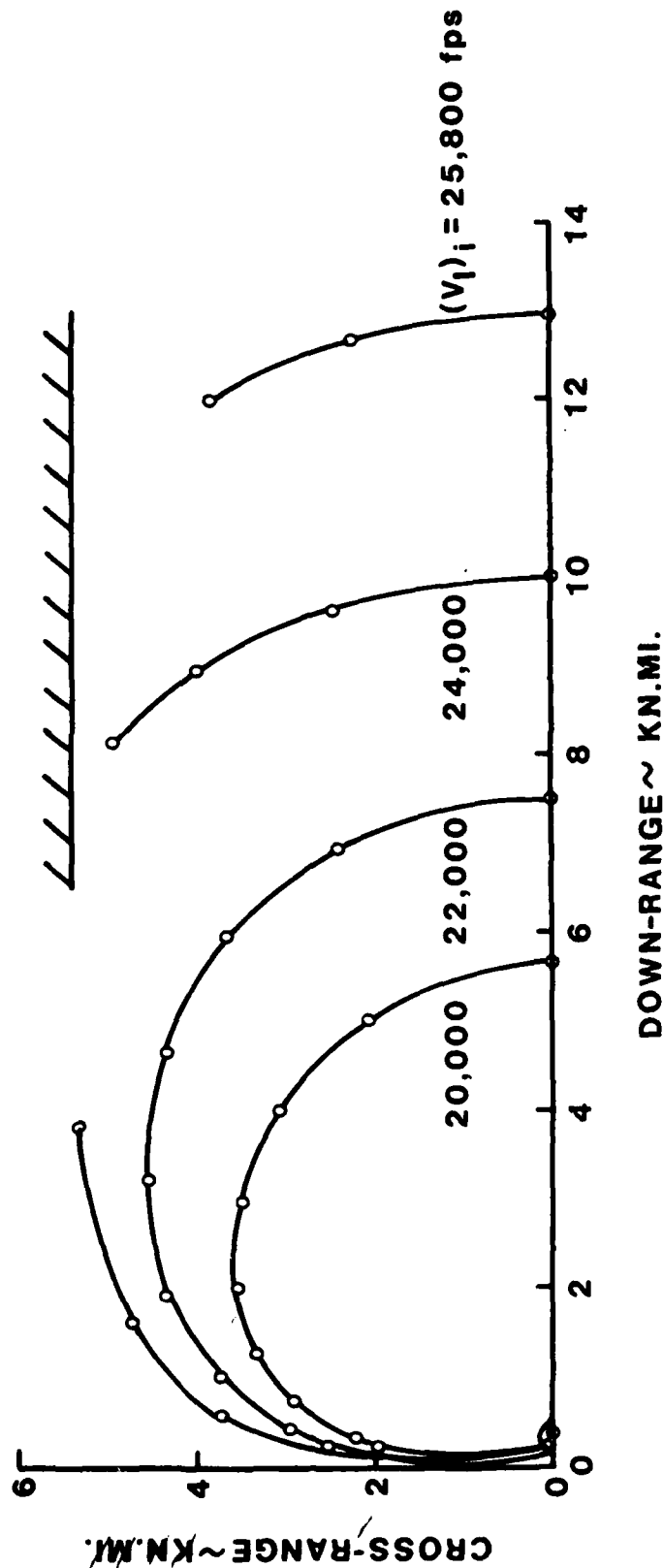
Figure C-32.   High (L/D) Footprint, Entry Angle = -20°

HIGH (L/D)

$\gamma_E = -25°$

$\sigma_i = 90°$

$\theta = \phi = 0°$
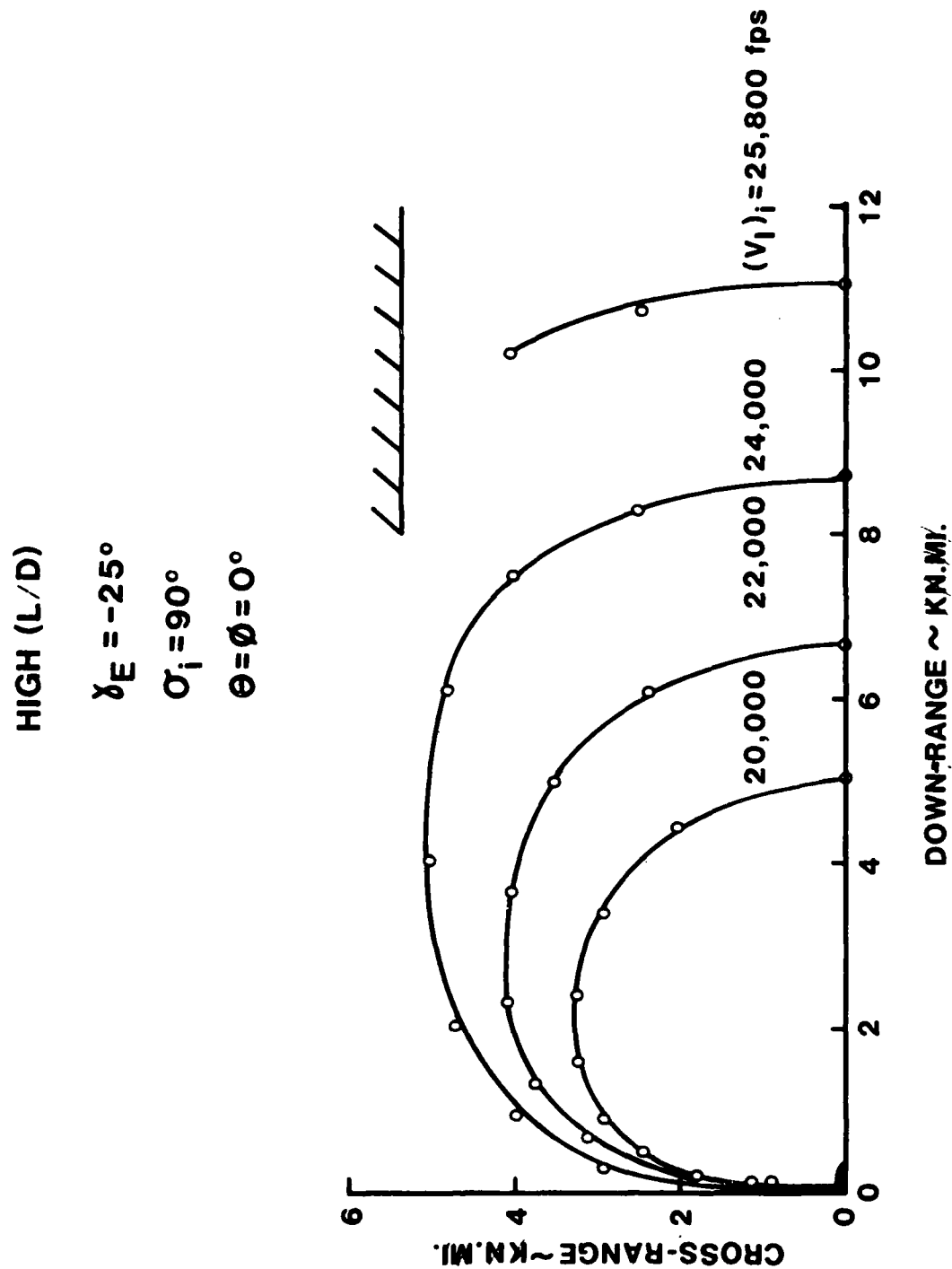
Figure C-33. High (L/D) Footprint, Entry Angle = -25°
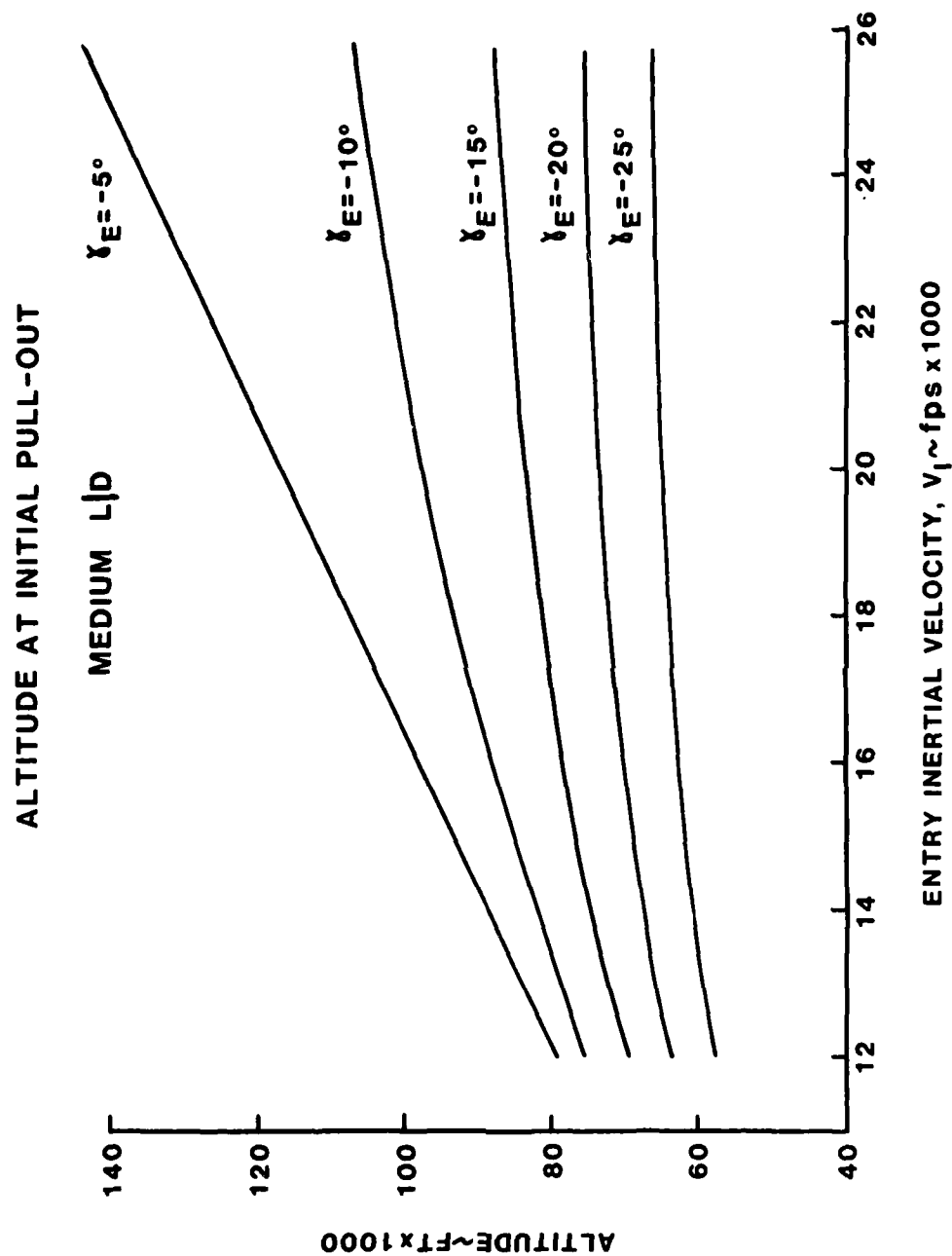
Figure C-34. Medium (L/D) Pull-Out Altitudes

MEDIUM L|D

RANGE TO INITIAL PULL-OUT
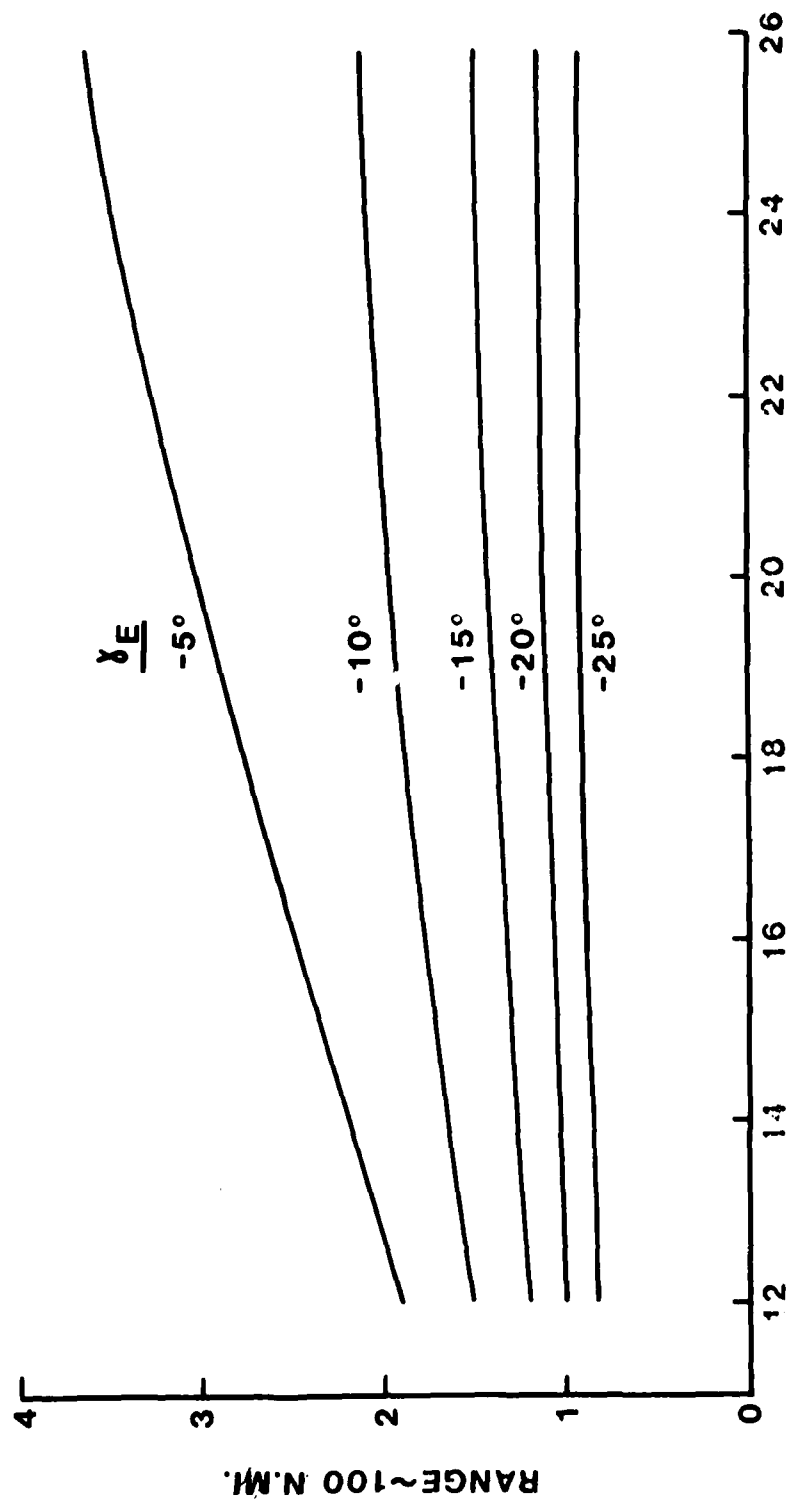
Figure C-35. Medium (L/D) Range to Initial Pull-Out

MEDIUM L|D

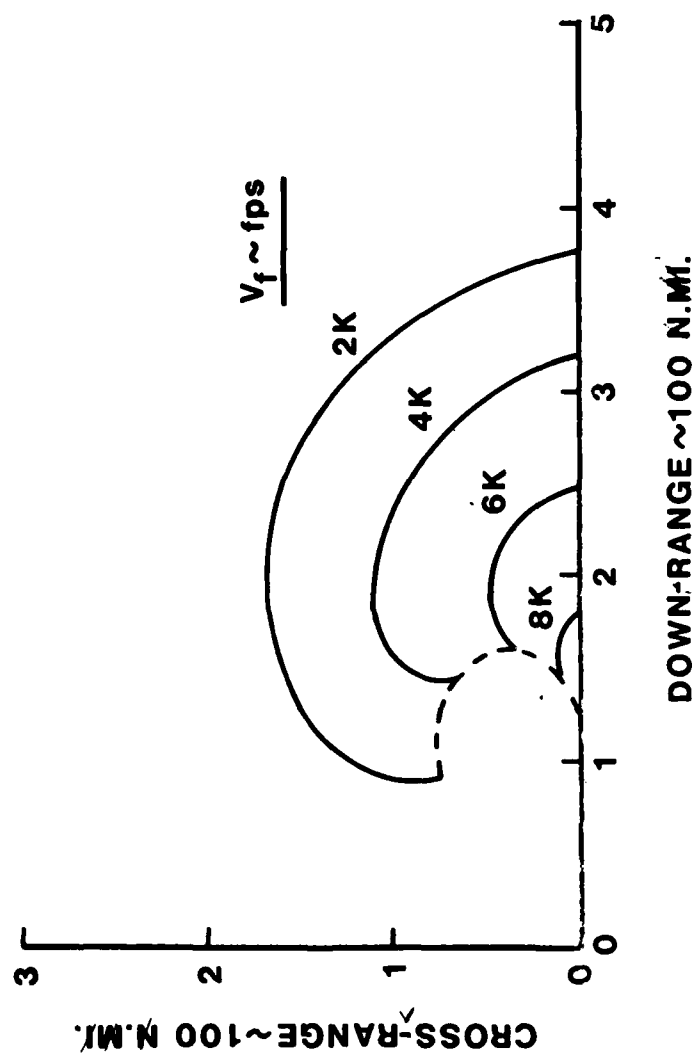ISO-VELOCITY CONTOURS

$(V_I)_i = 12,000$ fps

$\gamma_E = -5°$
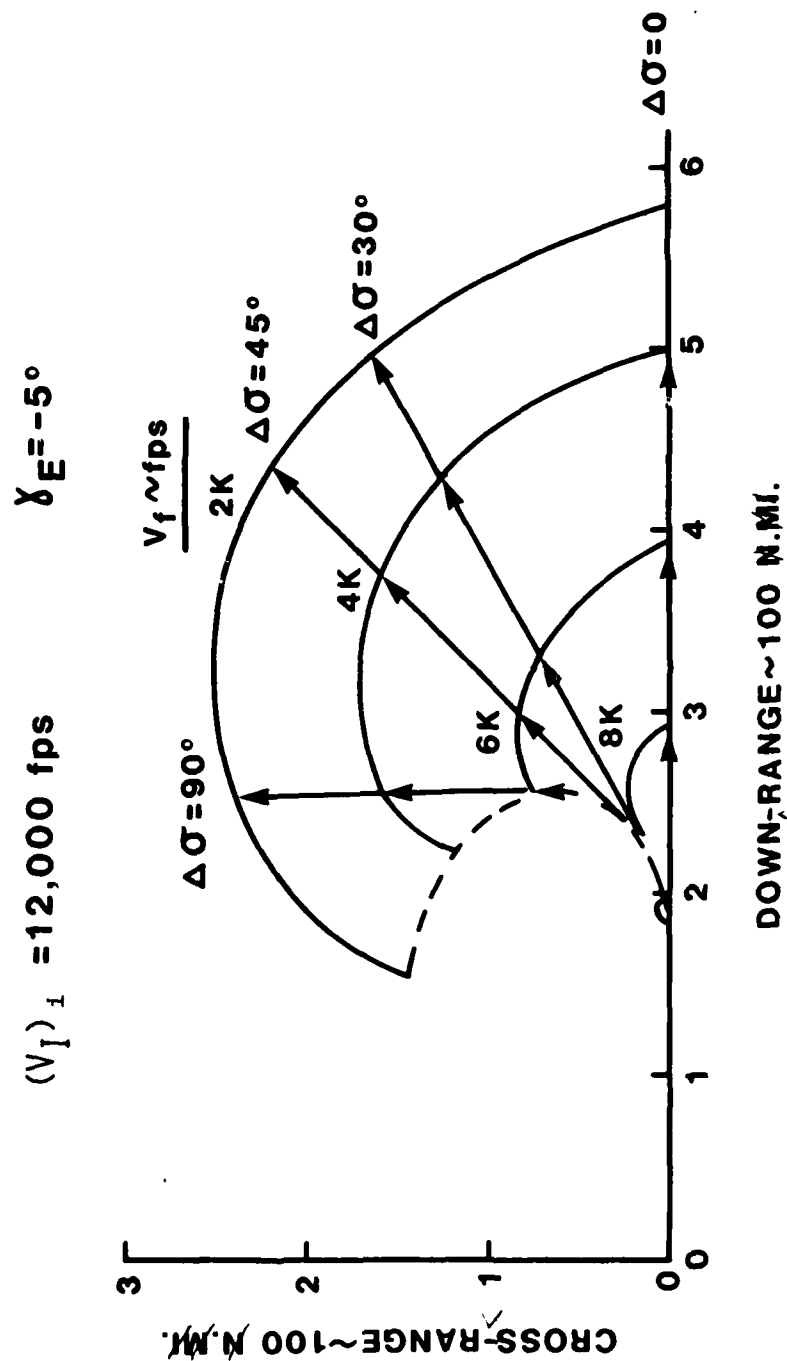
Figure C-36. Medium (L/D) Iso-Velocity Contours, $(V_I)_i = 12,000$ fps, $\gamma_e = -5°$
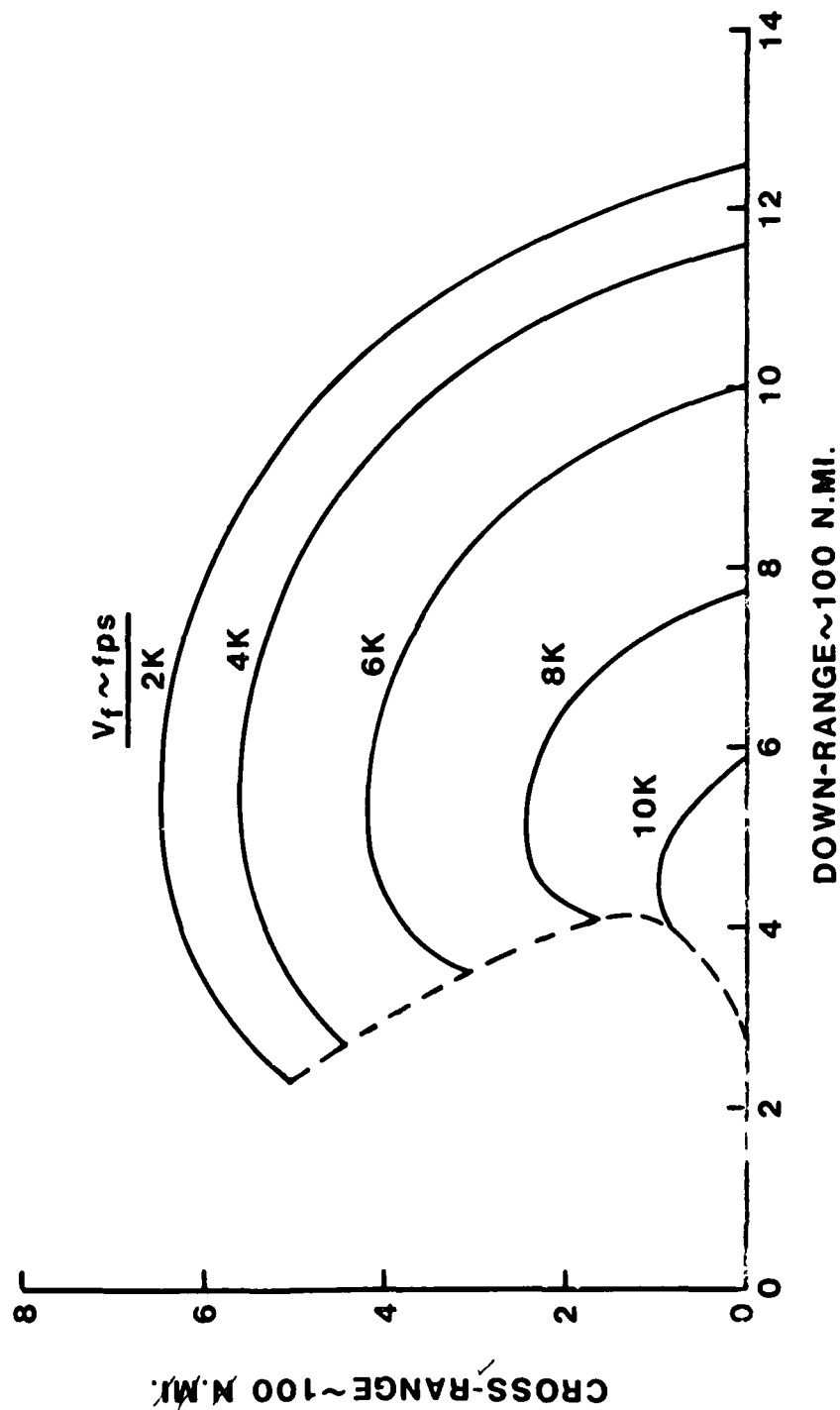
Figure C-37. Medium (L/D) Iso-Velocity Contours, $(V_I)_i$ =16,000 fps, γ_e = -5°

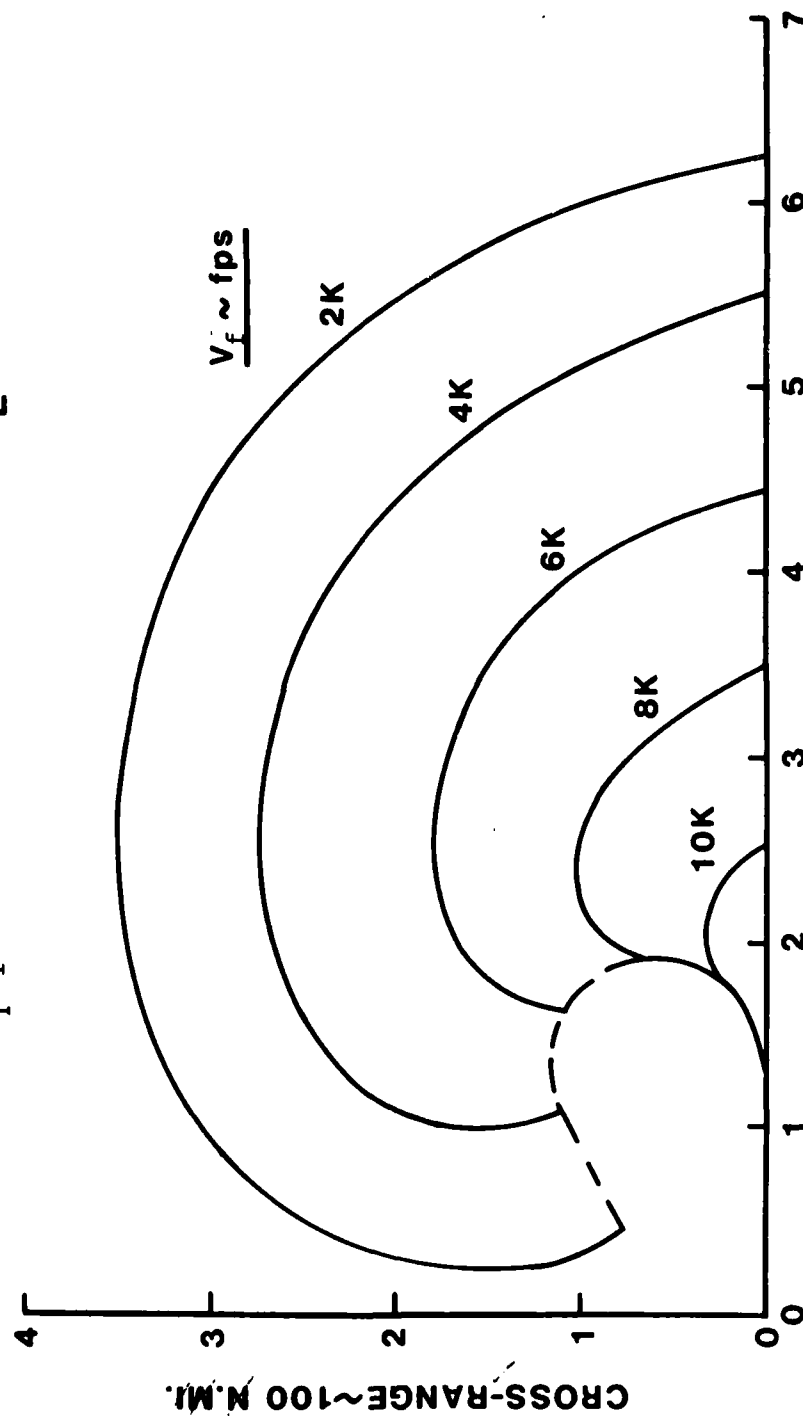Figure C-38. Medium (L/D) Iso-Velocity Contours, $(V_I)_i$=20,000 fps,
γ_e = -5°

MEDIUM L/D

ISO-VELOCITY CONTOURS

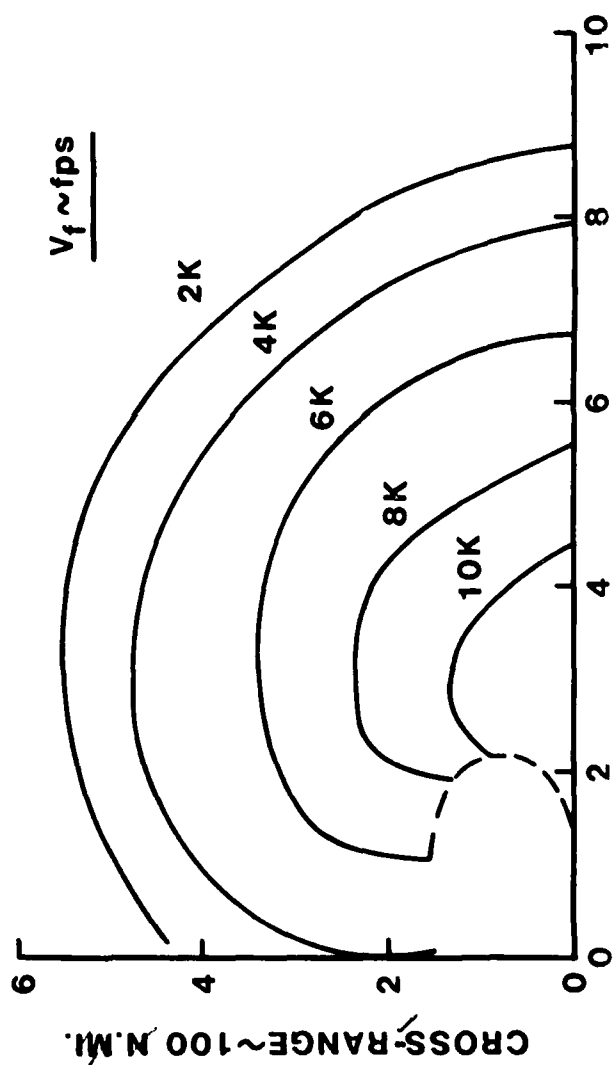$(V_I)_i = 12,000$ fps $\qquad \delta_E = -10°$

$\dfrac{V_f \sim \text{fps}}{}$

2K

4K

6K

DOWN-RANGE~100 N.MI.

CROSS-RANGE~100 N.MI.
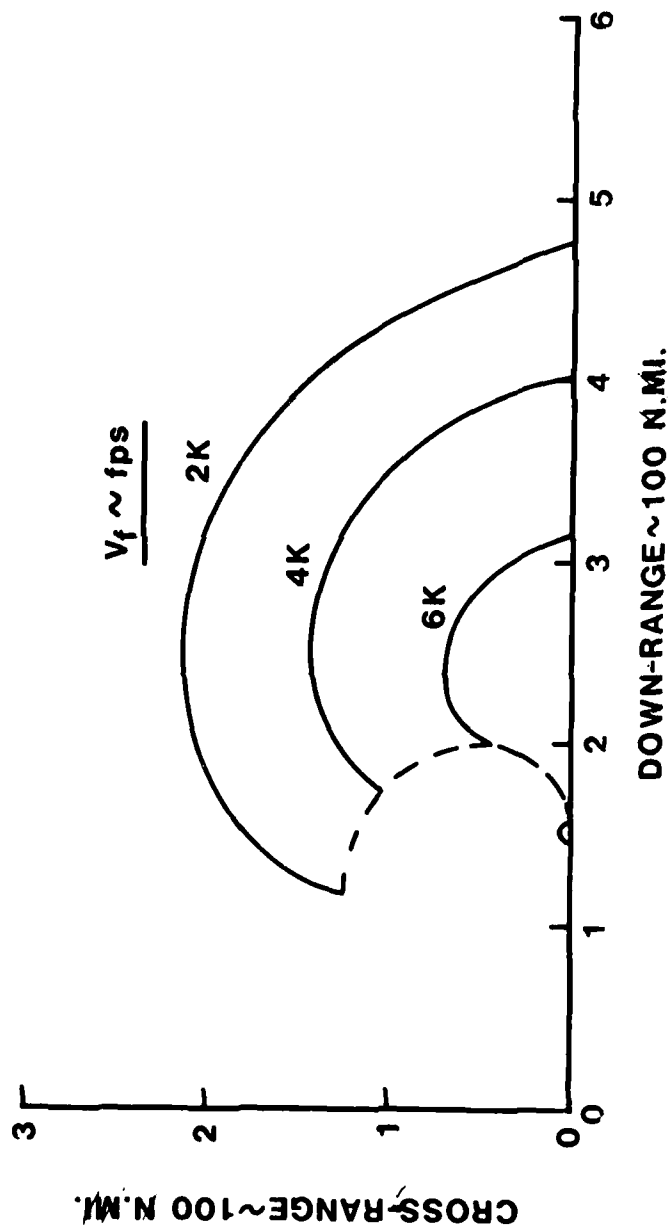
Figure C-39. Medium (L/D) Iso-Velocity Contours, $(V_I)_i = 12,000$ fps, $\gamma_e = -10°$

115

MEDIUM L/D

ISO-VELOCITY CONTOURS
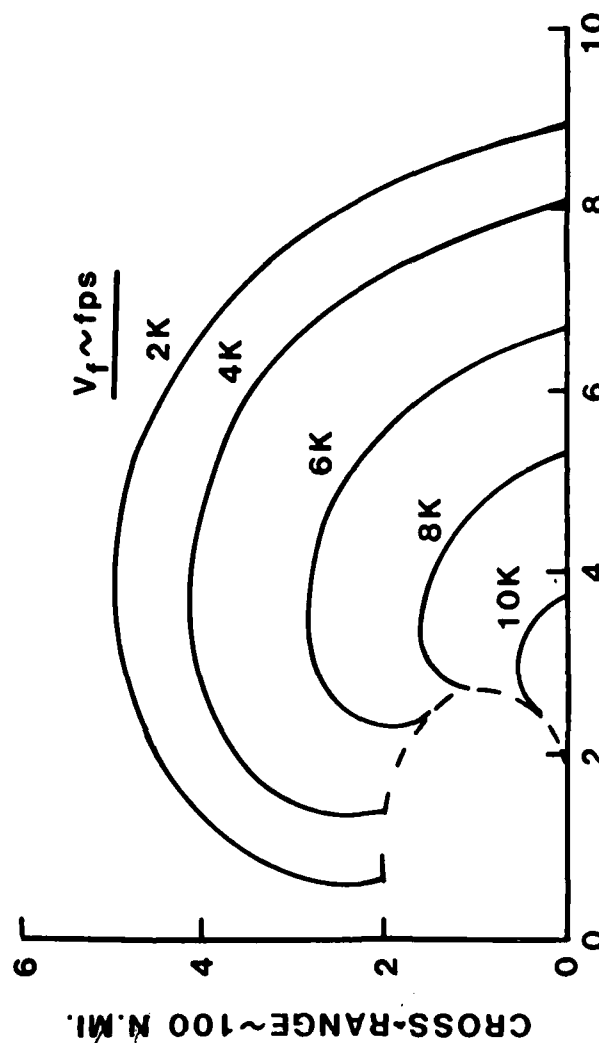
$(V_I)_i = 16,000$ fps $\gamma_E = -10°$

Figure C-40.   Medium (L/D) Iso-Velocity Contours, $(V_I)_i = 16,000$ fps, $\gamma_e = -10°$
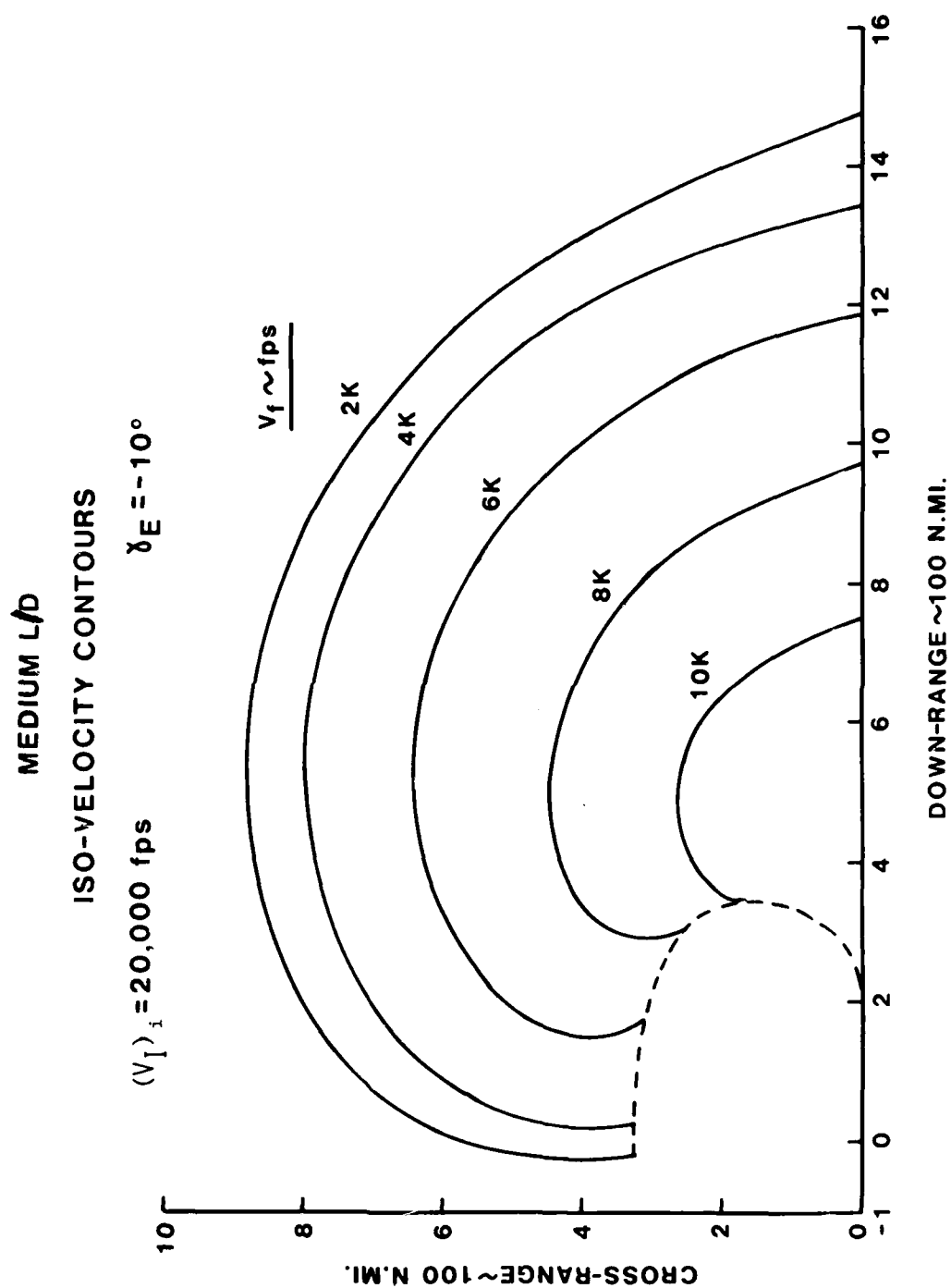
Figure C-41. Medium (L/D) Iso-Velocity Contours, $(V_I)_i$ =20,000 fps, γ_e = -10°
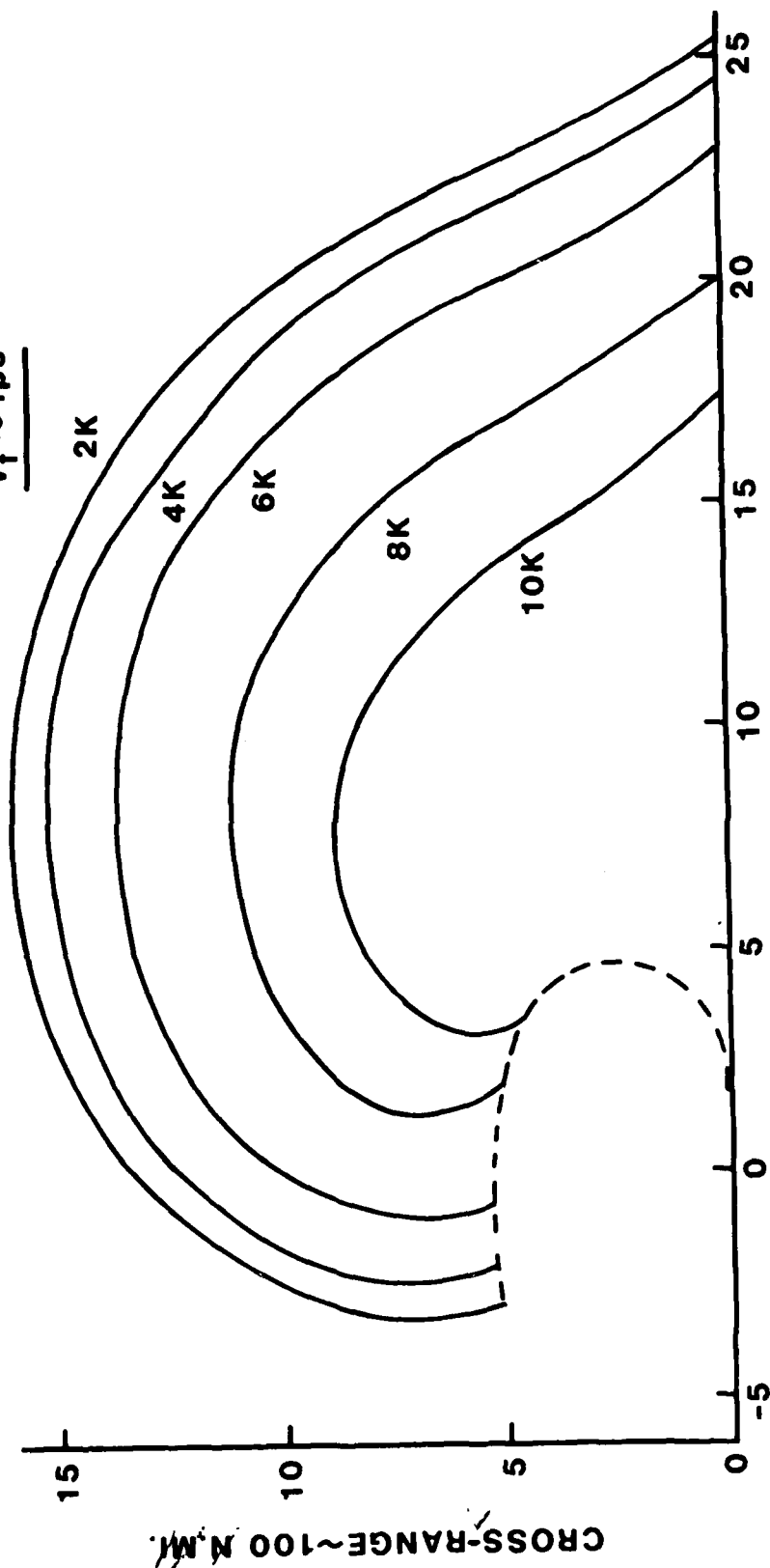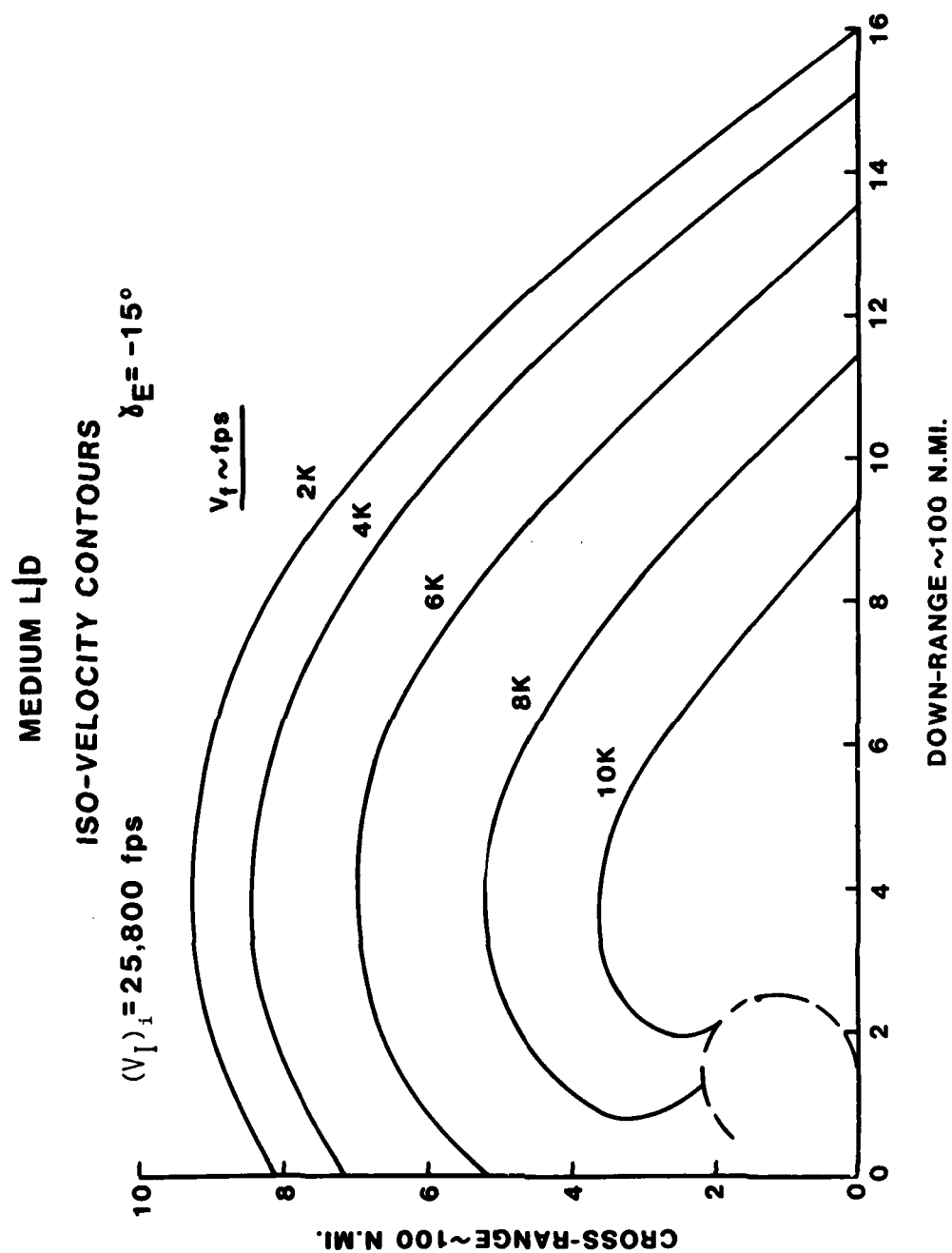
Figure C-42. Medium (L/D) Iso-Velocity Contours, $(V_I)_i$ =25,800 fps, γ_e = -10°

MEDIUM L|D

ISO-VELOCITY CONTOURS

$\delta_E = -15°$

$(V_I)_i = 12,000$ fps

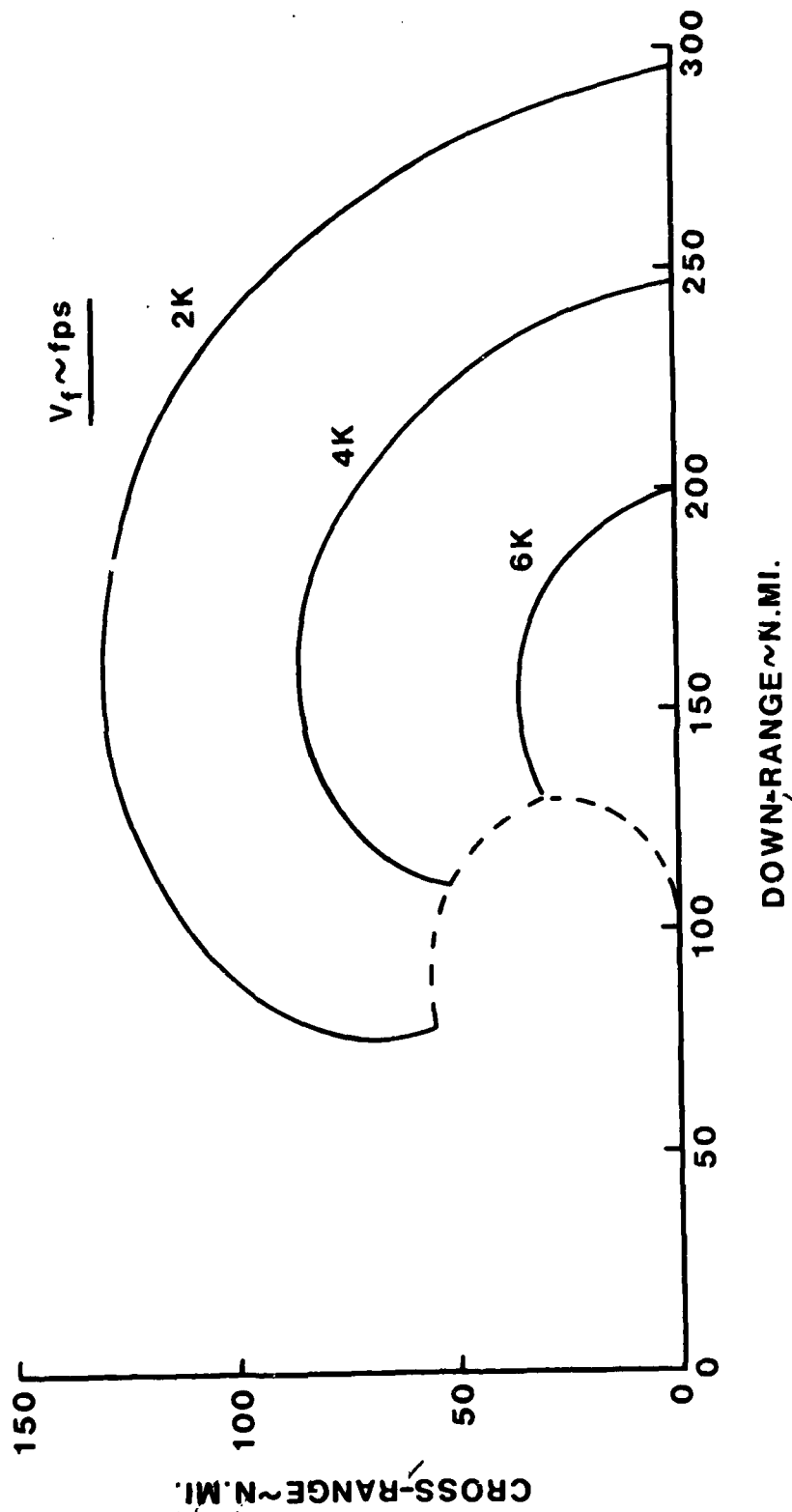Figure C-43. Medium (L/D) Iso-Velocity Contours, $(V_I)_i = 12,000$ fps, $\gamma_e = -15°$

119

MEDIUM L|D

ISO-VELOCITY CONTOURS

$\delta_E = -15°$

$(V_I)_i = 16,000$ fps

Figure C-44. Medium (L/D) Iso-Velocity Contours, $(V_I)_i$=16,000 fps, $\gamma_e = -15°$

Figure C-45. Medium (L/D) Iso-Velocity Contours, $(V_I)_i$=20,000 fps, γ_e = -15°

121

MEDIUM L|D

ISO-VELOCITY CONTOURS

$\delta_E = -15°$

$(V_I)_i = 25,800$ fps

$V_f \sim fps$

Figure C-46. Medium (L/D) Iso-Velocity Contours, $(V_I)_i = 25,800$ fps, $Y_e = -15°$

CROSS-RANGE ~100 N.MI.

DOWN-RANGE ~100 N.MI.

Figure C-47. Medium (L/D) Iso-Velocity Contours, $(V_I)_i$=12,000 fps, γ_e = -20°

Figure C-48. Medium (L/D) Iso-Velocity Contours, $(V_I)_i$ -16,000 fps, $\gamma_e = -20°$
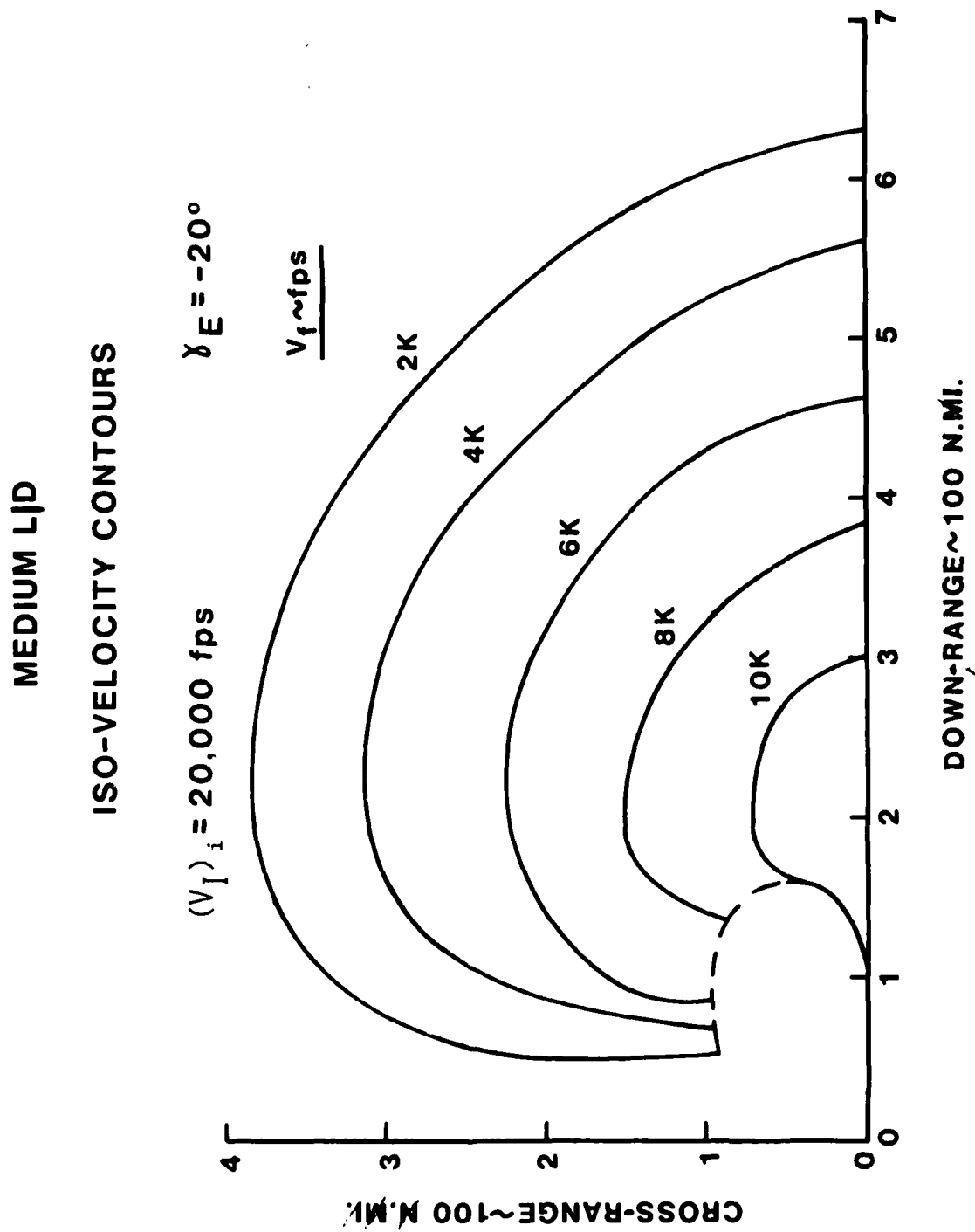
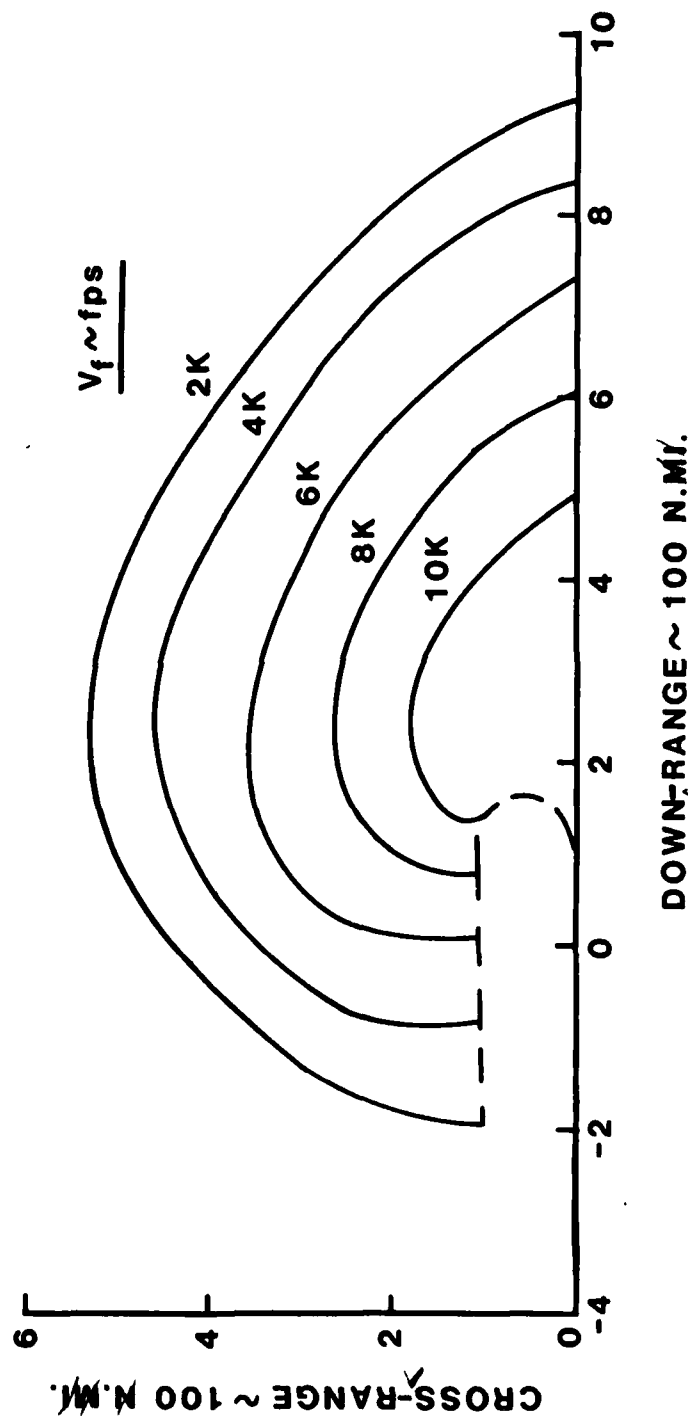Figure C-49. Medium (L/D) Iso-Velocity Contours, $(V_I)_i$ =20,000 fps, γ_e = -20°

Figure C-50. Medium (L/D) Iso-Velocity Contours, $(V_I)_i$ =25,800 fps, γ_e = -20°

MEDIUM L/D

ISO-VELOCITY CONTOURS

$\delta_E = -25°$

$(V_I)_i = 12,000$ fps

$\frac{V_f \sim fps}{}$

2K

4K

6K

CROSS-RANGE ~ N.MI.

DOWN-RANGE~N.MI.

100

50

0
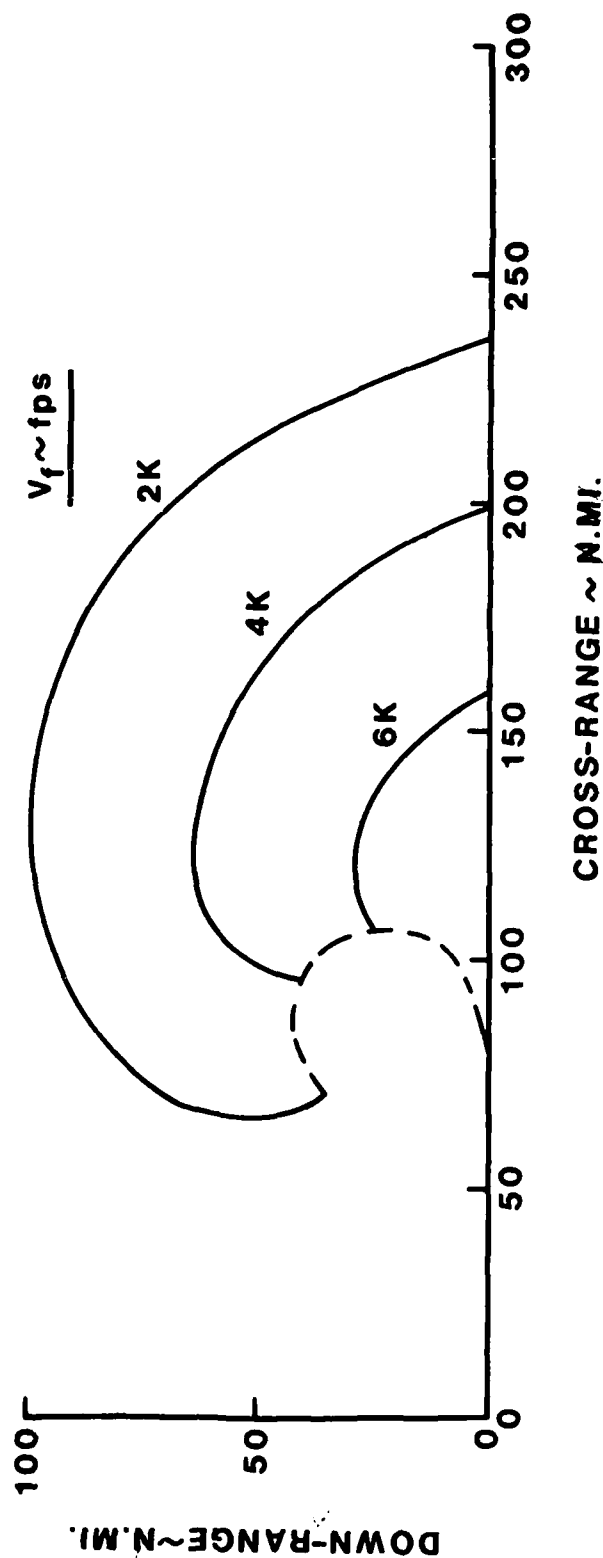
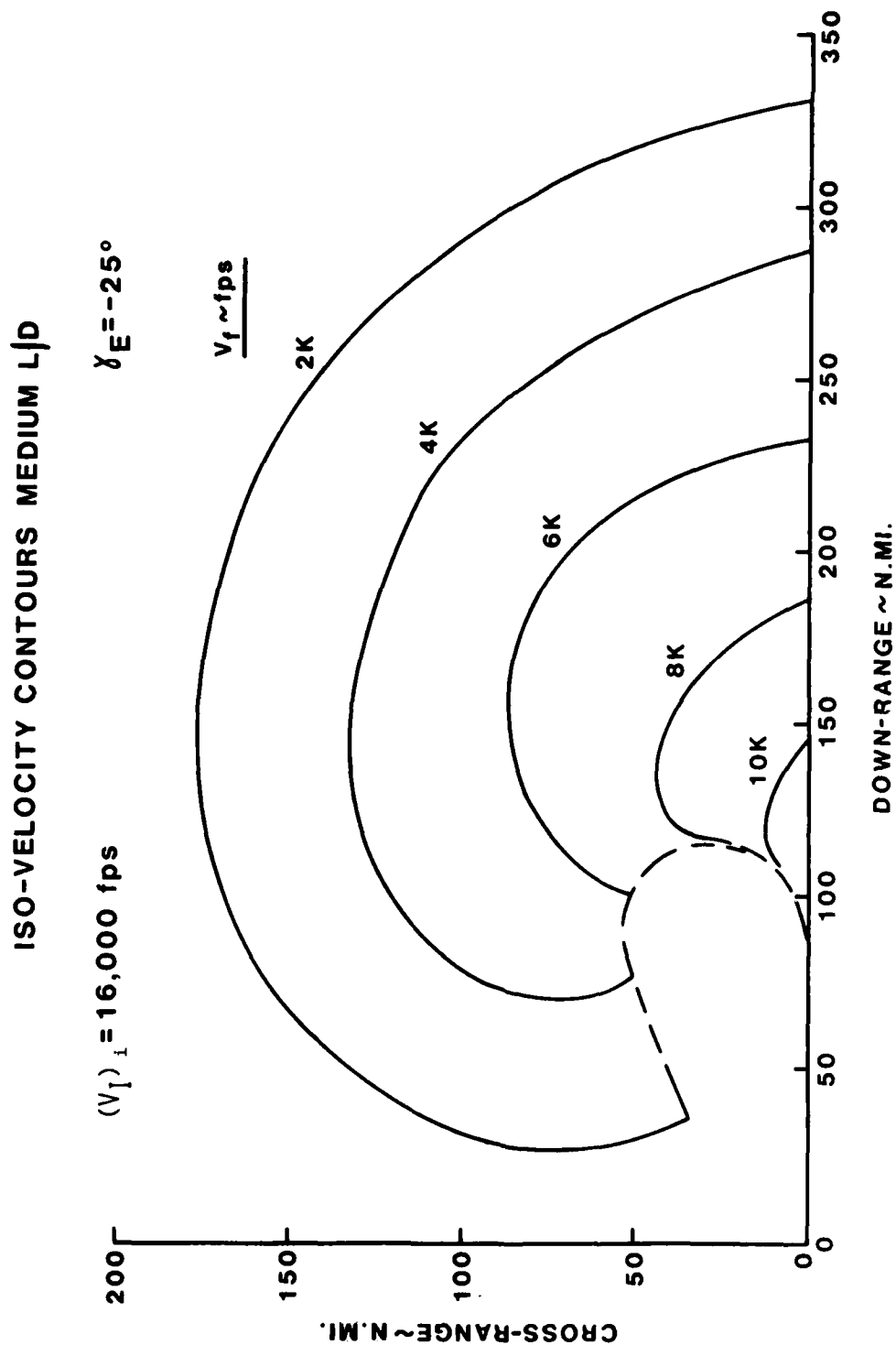Figure C-51. Medium (L/D) Iso-Velocity Contours, $(V_I)_i = 12,000$ fps, $\gamma_e = -25°$

127
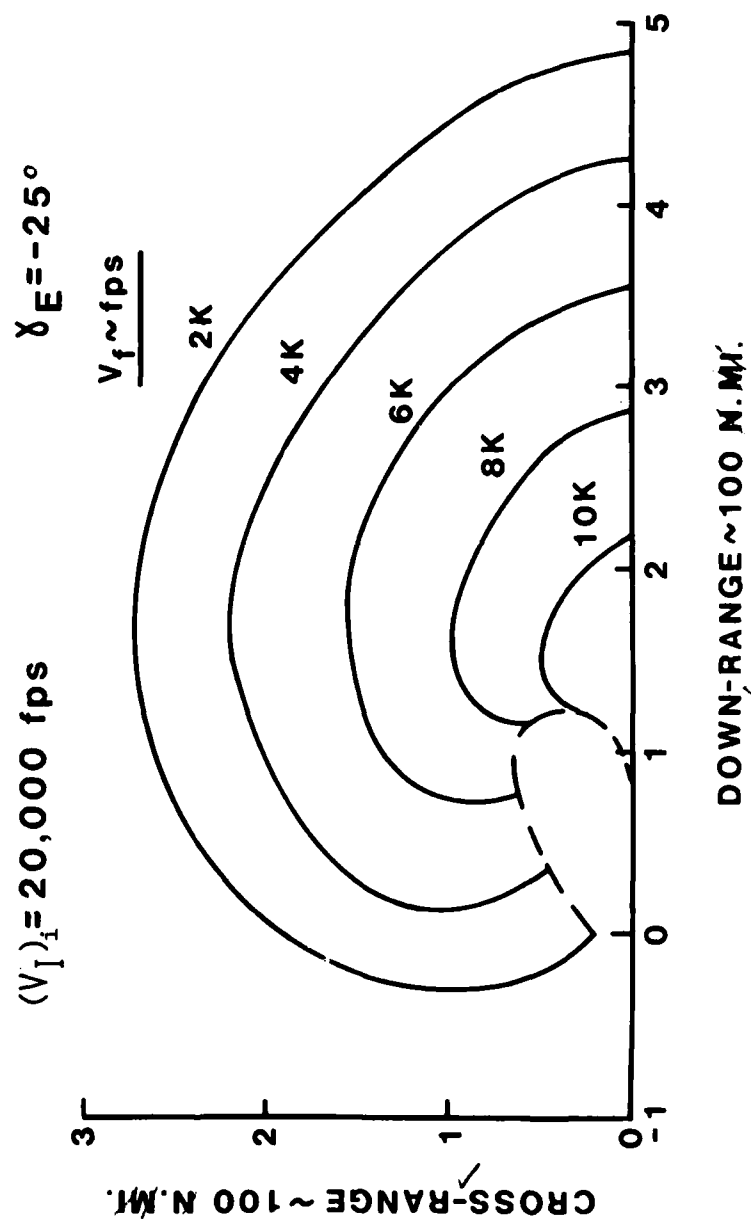
Figure C-52. Medium (I/D) Iso-Velocity Contours, $(V_t)_i=16,000$ fps, $\gamma_e = -25°$

MEDIUM L|D

ISO-VELOCITY CONTOURS

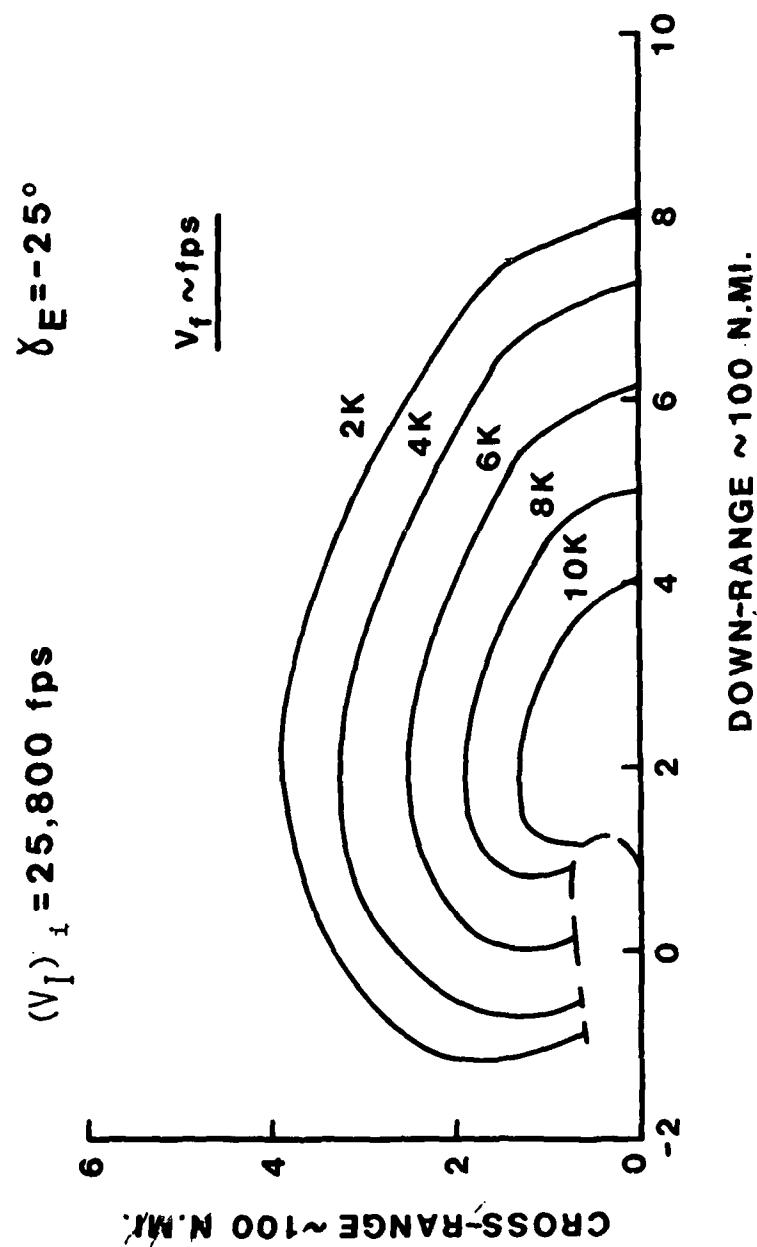Figure C-53. Medium (L/D) Iso-Velocity Contours, $(V_I)_i$=20,000 fps, γ_e = -25°

Figure C-54. Medium (L/D) Iso-Velocity Contours, $(V_I)_i$ =25,800 fps, γ_e = -25°

REFERENCES

1. L. D. Peterson, Trajectory Optimization by Method of Steepest Descent: Formulation, AFFDL-TR-67-108 Vol I, Flight Dynamics Laboratory, Wright-Patterson AFB, Ohio, December 1967.

2. D. T. Johnson, Performance Estimation of Unpowered High Lifting Reentry Vehicles, FDMG TM 65-16, Flight Dynamics Laboratory, Wright-Patterson AFB, Ohio, February 1965.

3. C. Bursey, D. Johnson, R. Nash, "Lifting Entry Vehicles Performance Analysis Methods,: AIAA Paper No. 1665, Astrodynamics Conference, Danvers, Massachusetts, August 1980.

4. D. S. Hague, "An Introduction to Multivariable Search Technique for Parameter Optimization," N68-19041, The Boeing Co., Seattle, Washington, 1968.

5. D. Hague, R. Jones, C. Glatt, Combat Optimization and Analysis Program-COAP-Parameter Optimization Subprogram Manual, AFFDL-TR-71-52 Vol. IV, Flight Dynamics Laboratory, Wright-Patterson AFB, Ohio, August 1971.

6. F. O. Young, Six-Degree-of-Freedom Flight Path Study Generalized Computer Program (SDFCP), AFFDL-TR-75-1, Flight Dynamics Laboratory, Wright-Patterson AFB, Ohio, July 1975.

7. A. Thomas, A. Perlbachs, A. Nagel, Advanced Re-entry Systems Heat Transfer Manual for Hypersonic Flight, AFFDL-TR-65-195, Air Force Flight Dynamics Laboratory, Wright-Patterson AFB, Ohio, October 1966.

8. Rockwell International, Space Division, Aerodynamic Design Data Book, Vol. I, October 1978.

9. J. H. Porter, Jr, Static Force Tests of the MRRV Hypersonic Configuration at Mach Numbers 2-5, AEDC-TSR-79-V43.

10. Valentine Dahlem, Summary of Aerodynamic Characteristics of the FDL-6 High L/D Configuration, AFFDL-TR-72-48, July, 1972

11. Private communication with G. L. Burke of AFWAL/FIMG.

12. DISSPLA User Information Manual, Integrated Software Systems Corporation and Control Data Corporation, 1974.

13. E. B. Graves, Aerodynamic Characteristics of a Monoplanar Missile Concept with Bodies of Circular and Elliptical Cross Section, NASA TM-74079, 1977.

14. AFWAL-TR-80-3071. Vol IV, Aero-Configured Missile Development, Phase I, Experimental Program, 1980.

BIBLIOGRAPHY

1. Brown, R., Bruelle, R., Griffin, G., <u>Six-Degree-or-Freedom Flight Path Study Generalized Computer Program</u>, WADD-TR-60-781, Flight Dynamics Laboratory, Wright-Patterson AFB, Ohio, May 1961.

2. Fay, J. A., Riddell, F. R., "Theory of Stagnation Point Heat Transfer in Disassociated Air," Journal of the Aeronautical Sciences, Vol. 25, No. 2, Feb 1958.